

A model integrating satellite-derived shoreline observations for predicting fine-scale shoreline response to waves and sea-level rise across large coastal regions

Sean Vitousek^{1,2}, Kilian Vos³, Kristen D Splinter³, Li Erikson¹, and Patrick L Barnard¹

¹USGS Pacific Coastal & Marine Science Center

²University of Illinois at Chicago

³University of New South Wales - Sydney

March 9, 2023

Abstract

Satellite-derived shoreline observations combined with dynamic shoreline models enable fine-scale predictions of coastal change across large spatiotemporal scales. Here, we present a satellite-data-assimilated, “littoral-cell”-based, ensemble Kalman-filter shoreline model to predict coastal change and uncertainty due to waves, sea-level rise, and other natural and anthropogenic processes. We apply the developed ensemble model to the entire California coastline (approximately 1,350 km), much of which is sparsely monitored with traditional survey methods (e.g., Lidar/GPS). Water-level-corrected, satellite-derived shoreline observations (obtained from the CoastSat toolbox) offer a nearly unbiased representation of in-situ surveyed shorelines (e.g., Mean Sea Level elevation contours) at Ocean Beach, San Francisco. We demonstrate that model calibration with satellite observations during a 20-year hindcast period (1995 to 2015) provides a nearly equivalent model forecast accuracy during a validation period (2015 to 2020) compared to model calibration with monthly in-situ observations at Ocean Beach. When comparing model-predicted shoreline positions to satellite-derived observations, the model achieves an accuracy of <10 m RMSE for nearly half of the entire California coastline for the validation period. The calibrated/validated model is then applied for multi-decadal simulations of shoreline change due projected wave and sea-level conditions while holding the model parameters fixed. By 2100, the model estimates that 25 to 70% of California’s beaches may become completely eroded due to sea-level rise scenarios of 0.5 to 3.0 m, respectively. The satellite-data-assimilated modeling system presented here is generally applicable to a variety of coastal settings around the world owing to the global coverage of satellite imagery.

1 **A model integrating satellite-derived shoreline observations for predicting fine-scale**
2 **shoreline response to waves and sea-level rise across large coastal regions**

3 *Sean Vitousek^{1,2}, Kilian Vos³, Kristen D. Splinter³, Li Erikson¹, and Patrick L. Barnard¹*

4 **Author Affiliations**

- 5 1. U.S. Geological Survey
- 6 2. University of Illinois at Chicago
- 7 3. UNSW Sydney

8
9 **Abstract**

10 Satellite-derived shoreline observations combined with dynamic shoreline models enable fine-
11 scale predictions of coastal change across large spatiotemporal scales. Here, we present a
12 satellite-data-assimilated, “littoral-cell”-based, ensemble Kalman-filter shoreline model to
13 predict coastal change and uncertainty due to waves, sea-level rise, and other natural and
14 anthropogenic processes. We apply the developed ensemble model to the entire California
15 coastline (approximately 1,350 km), much of which is sparsely monitored with traditional survey
16 methods (e.g., Lidar/GPS). Water-level-corrected, satellite-derived shoreline observations
17 (obtained from the CoastSat toolbox) offer a nearly unbiased representation of in-situ surveyed
18 shorelines (e.g., Mean Sea Level elevation contours) at Ocean Beach, San Francisco. We
19 demonstrate that model calibration with satellite observations during a 20-year hindcast period
20 (1995 to 2015) provides a nearly equivalent model forecast accuracy during a validation period
21 (2015 to 2020) compared to model calibration with monthly in-situ observations at Ocean Beach.
22 When comparing model-predicted shoreline positions to satellite-derived observations, the model

23 achieves an accuracy of <10 m RMSE for nearly half of the entire California coastline for the
24 validation period. The calibrated/validated model is then applied for multi-decadal simulations
25 of shoreline change due projected wave and sea-level conditions while holding the model
26 parameters fixed. By 2100, the model estimates that 25 to 70% of California's beaches may
27 become completely eroded due to sea-level rise scenarios of 0.5 to 3.0 m, respectively. The
28 satellite-data-assimilated modeling system presented here is generally applicable to a variety of
29 coastal settings around the world owing to the global coverage of satellite imagery.

30

31 **Plain Language Summary (PLS)**

32 We present a computer model to predict shoreline change due to waves, sea-level rise, and other
33 local processes. We apply the model to the entire California coastline (approximately 1,350 km),
34 much of which is not well monitored using traditional survey methods. Observations of
35 historical shoreline position obtained from satellite images can be used in lieu of traditional
36 shoreline survey data to estimate erosion/accretion trends as well as to calibrate and validate
37 models. By 2100, the model estimates that 25 to 70% of California's beaches may become
38 completely eroded due to sea-level rise scenarios of 0.5 to 3.0 m, respectively.

39

40 **1. Introduction**

41 Accurate predictions of coastal erosion in response to sea-level rise, changing wave conditions,
42 and reduced natural sediment supplies are increasingly sought by coastal managers to assess the
43 impacts of climate change on beaches (Masselink et al., 2016; Vitousek et al., 2017a; Le

44 Cozannet et al., 2019). Several well-tested and emerging models are capable of simulating
45 coastal erosion (Roelvink, 2011; Montaña et al., 2020; Toimil et al., 2020a, Ranasinghe 2020,
46 Hunt et al., 2023). However, most models inherently capture a limited number of processes
47 occurring at a narrow geographic scope, because of computational or data availability
48 constraints. Although there are many different paradigms of coastal evolution models, two main
49 classifications often emerge: (1) physics-based numerical models and (2) reduced-complexity (or
50 process-based) models. On the one hand, physics-based models numerically solve equations of
51 conservation of mass and momentum of fluid and sediment with the aim to resolve all (or nearly
52 all) of the important oceanographic/hydrodynamic processes resulting in sediment transport and
53 coastal change. However, the high computational effort of physics-based models often hinders
54 simulation of large-scale (e.g., 100's m to 100 km) or long-term (e.g., annual and longer) coastal
55 change. On the other hand, reduced-complexity models (Murray 2007) seek to parameterize a
56 limited number of dominant coastal-change processes or trends, usually without explicitly
57 resolving the underlying hydrodynamic processes responsible for sediment transport. The
58 biggest drawback of reduced-complexity models is that they generally require observational data
59 to parameterize, calibrate, and/or validate the model (Vitousek et al., 2017; Montaña et al.,
60 2020), at least when used in a predictive sense rather than an exploratory sense (Murray et al.,
61 2016). Although they do not explicitly resolve all relevant physical processes, data-driven
62 reduced-complexity models can often implicitly account for the most dominant processes via
63 calibration to local observations (Vitousek et al., 2017). However, time series of coastal-change
64 observations over multiple years are often sparse or narrow in geographic scope.

65 The field of coastal morphodynamics has, until recently, been 'data poor,' with long-term
66 monitoring data existing only at a limited number sites (Vitousek et al., 2022). However,

67 reliable forecasts of coastal erosion on decadal to centennial timescales over large geographic
68 regions (e.g., state and country scale) are increasingly sought, even in ‘data-poor’ environments.
69 Recent progress has been made to improve the temporal frequency of coastal observations over
70 large spatiotemporal scales (e.g., 1 m - 100 km and days - decades) using satellites (Pardo-
71 Pascual et al., 2012; Hagenaars et al., 2017; Luijendijk et al., 2018; Vos et al., 2019a,b; Nelson &
72 Miselis, 2019, Vos et al., 2023). Since the 1980’s, Earth-observing satellites (e.g., the Landsat
73 missions) have collected a massive archive of coastal imagery data that have only recently been
74 leveraged for science and engineering applications (Turner et al., 2021). Recent advances in
75 satellite remote-sensing analysis provide a window into the recent past and current state of the
76 world’s beaches (Luijendijk et al., 2018) and their large-scale vulnerability to climatic forces like
77 El Niño (Vos et al., 2023). By leveraging the large streams of data offered from satellites,
78 reduced-complexity coastal-change models seem poised for success in a challenging field of
79 study owing to the newly found ‘treasure trove’ of data (Hunt et al., 2023, Vitousek et al., 2023,
80 Barnard & Vitousek 2023).

81 For more than two decades, satellite-data have been effectively assimilated into predictive
82 atmosphere and ocean models (e.g., ERA5 – Hersbach et al., 2020 and CFSR – Saha et al.,
83 2010). Yet, integration of satellite-data with large-scale, dynamic coastal-change models have
84 remained underdeveloped, until now. Most applications of satellite-derived shorelines
85 investigate shoreline trends (e.g., Luijendijk et al., 2018, Calkoen et al., 2021, Castelle et al.,
86 2022) or interannual variability (Vos et al., 2023), rather than synoptic shoreline variability with
87 wave and storm events. Recently, Alvarez-Cuesta et al., (2021a,b) integrated satellite-derived
88 across 40 km of the Spanish Mediterranean Coast into a dynamic shoreline model. Similarly, in
89 this paper, we demonstrate how decades of satellite imagery can be leveraged to accurately

90 calibrate and validate coastal evolution models, enabling predictions/projections of coastal
91 change in historically data-poor environments over vast geographic scales.

92 **2. Methods**

93 **2.1 Shoreline model**

94 The shoreline-change model, used here, is an update of CoSMoS-COAST (Vitousek et al., 2017;
95 Vitousek et al., 2021), a transect-based, data-assimilated ‘one-line’ model that integrates
96 longshore and cross-shore transport processes. The CoSMoS-COAST model was initially
97 developed as the long-term shoreline change component of the USGS Coastal Storm Modeling
98 System (CoSMoS; Barnard et al., 2014), and the model’s novel developments as part of the
99 current work are presented in Figure 1. In summary, the notable and novel aspects of the current
100 work include: (1) integration with satellite-derived shorelines [which provides nearly a thousand-
101 fold increase in assimilation data over the previous iteration in Vitousek et al., (2017)], (2) the
102 development of a novel “littoral-cell based” data-assimilation method (detailed in Appendix B),
103 and (3) projections across the entire state of California (approximately 1,350 km) compared to
104 the previous iteration in Vitousek et al., (2017), which spanned only 500 km of southern
105 California.

CoSMoS-COAST: Coastal One-line Assimilated Simulation Tool

Model Inputs:

Model transects:

- Transect locations (100-200 m, shore-normal)
- Transect designations: full model, cross-shore only, rate only, or no prediction
- Non-erodible shoreline
- Beach slope
- No beach profile elevation data needed

Forcing conditions:

Wave hindcast
(1995-2020)

Wave forecast / projection
(2020-2100)

+ future sea-level conditions

Historical shoreline data:

- For model calibration & validation:
 - Sources:
 - Lidar
 - GPS
 - Satellites
- CoastSat** (Vos et al., 2019)

Governing equation:

$$\frac{\partial Y}{\partial t} = \underbrace{\left[\frac{1}{d_c} \frac{\partial Q}{\partial X} - \frac{c}{\tan \beta} \frac{\partial S}{\partial t} \right]}_{\text{long-term processes}} + \underbrace{v_{lt}}_{\text{[3] long-term residual shoreline trend; unresolved processes}} + \underbrace{\left[\frac{1}{\tau} (Y_{eq} - Y) + \varepsilon_{add} \right]}_{\text{short-term processes}} + \text{Localized Ensemble Kalman Filter (EnKF) data assimilation based on 'littoral cells'}$$

Model state variables and parameters:

- Y = shoreline position
 Q = longshore transport
 t = time
 X = alongshore coordinate
 $\alpha_{shoreline}$ = shoreline angle
 α_{wave} = wave angle
 $\tan \beta$ = transgression slope
 d_c = closure depth

$$Y_{eq} = -\Delta T \frac{H_z^2 - (H_z)_b^2}{(H_z)_b^2}$$

$$\tau = \Delta T \left(\frac{H_z}{(H_z)_b} \right)^{-1}$$

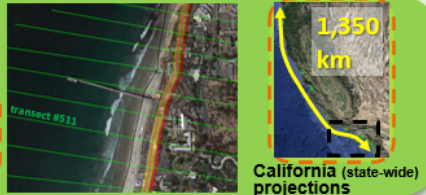
$$\varepsilon_{add} \sim N(0, \sigma^2)$$

Assimilated parameters:

- ΔT = equilibrium time scale
 ΔY = equilibrium erosion length scale
 c = SLR-recession coefficient
 v_{lt} = residual shoreline trend
 σ = additive noise parameter
 $(H_z)_b$ = background wave height
 K = longshore transport coefficient

Outputs:

- Future shoreline positions
- Model parameter estimates
- **Uncertainty estimates via ensemble simulations & comparisons w/ observations**



Developed in:

- Vitousek et al., 2017
- Vitousek et al., 2021
- Current paper

106

107 Figure 1 – An overview of the CoSMoS-COAST model, including the model inputs/outputs,
 108 variables/parameters, and governing equation for the current application in California. The
 109 figure also depicts advancements in the model from its initial development (Vitousek et al. 2017
 110 – black dashed lines) to Vitousek et al., 2021 (blue dashed lines) and to the current paper (orange
 111 dashed lines).

112 2.1.1 Model governing equation

113 The model governing equation, which is based on the one-dimensional conservation of sediment
 114 volume in the alongshore direction and initially developed in Vitousek et al., (2017, 2021), is
 115 given by

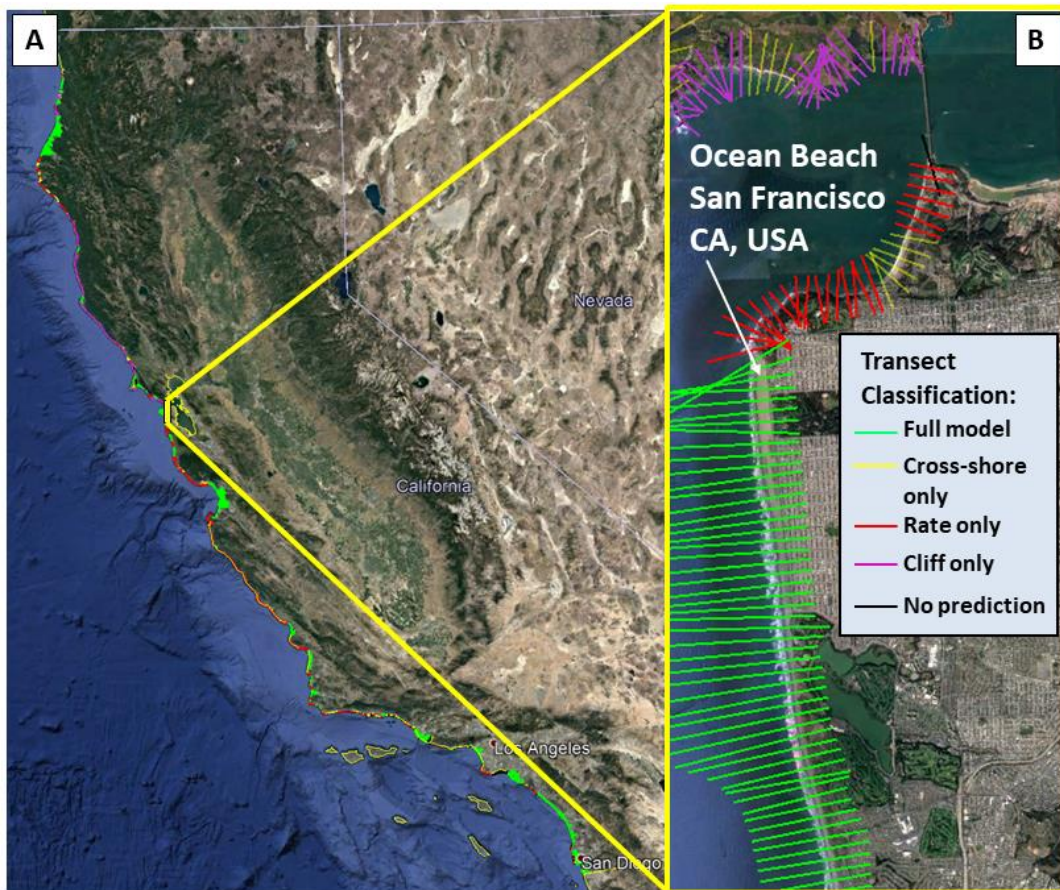
$$\begin{aligned}
116 \quad \frac{\partial Y}{\partial t} = & \overbrace{\left[-\frac{1}{d_c} \frac{\partial Q}{\partial X} - \frac{c}{\tan \beta} \frac{\partial S}{\partial t} \right]}^{\text{long-term processes}} + \underbrace{v_{lt}}_{\text{[3] long-term residual shoreline trend; unresolved processes}} + \overbrace{\left[\frac{1}{\tau} (Y_{eq} - Y) + \varepsilon \right]}^{\text{short-term processes}} \quad (1) \\
\text{shoreline change} & \quad \underbrace{\hspace{10em}}_{\text{[1] longshore transport}} \quad \underbrace{\hspace{10em}}_{\text{[2] shoreline migration due to sea-level rise}} \quad \underbrace{\hspace{10em}}_{\text{[4] cross-shore 'equilibrium' transport}} \quad \underbrace{\hspace{10em}}_{\text{[5] additive noise}}
\end{aligned}$$

117 Each term in Eq. (1) is defined in Figure 1 and detailed in Appendix A, alongside the
118 presentation of numerical methods to solve Eq. (1). In brief, Eq. (1) synthesizes several popular
119 individual-process models including: [1] a ‘one-line’ model for longshore transport (Pelnard-
120 Considere, 1956); [2] a cross-shore beach profile change model due to sea-level rise (Bruun,
121 1962; Davidson-Arnott, 2005; Anderson et al., 2015); [3] a long-term residual shoreline trend v_{lt}
122 that represents long-term processes like sources and sinks of sediment, e.g., fluvial inputs,
123 headland bypassing, beach nourishments, etc., which is estimated via assimilation of local
124 shoreline observations; [4] a wave-driven cross-shore equilibrium shoreline change model that
125 has been modified (without changing the underlying dynamics) from Yates et al., (2009), as
126 discussed in Vitousek et al., (2021); and finally [5] a noise term. Here, the noise term represents
127 (normally distributed) random, short-term, unresolved processes that cause fluctuations in
128 shoreline position with zero mean and user-prescribed standard deviation σ . The model
129 includes an ensemble Kalman filter data-assimilation method based on ‘littoral cells’ (discussed
130 below and detailed in Appendix B) that sequentially adjusts the model parameters (given in
131 Figure 1) to best match local observations at each time step (when data are available).

132 2.1.2 Model transects and littoral-cell-based data assimilation

133 The California model is comprised of 11,539 transects spaced approximately 100-200 m apart
134 (see Figure 2). Each transect is designated as either “full model”, “cross-shore only”, “rate
135 only”, “cliff only” or “no prediction” based on geologic characteristics (which occur for 31.9%,

136 18.2%, 30.6%, 12%, and 7.3% of the California coastline, respectively). Based on the transect
137 designation, the shoreline model retains or neglects certain physical processes and the
138 corresponding terms in the governing equation, Eq. (1), as described in Appendix A.2. For
139 example, “cross-shore only” transects neglect term [1] in Eq. (1), and “rate only” transects
140 neglect terms [1] and [4].



141
142 Figure 2 – The (~100-200 m spaced) model transects for the coast of California shown in panel
143 A. Panel B shows a zoomed-in plot of the transects at Ocean Beach, San Francisco. Transects
144 that are designated as “full model”, “cross-shore only”, “rate only”, “cliff only”, and “no
145 prediction” are shown in green, yellow, red, purple, and black, respectively. (Basemaps from
146 Google Earth).

147

148 The model transects are grouped into so-called ‘littoral cells’, which represent the basis for the
149 novel data-assimilation method, which is fully detailed in Appendix B. The grouping of
150 transects into littoral cells can be either user-specified or done automatically, by grouping all
151 neighboring transects with the same transect designation into a littoral cell (i.e., all adjacent “full
152 model” transects constitute a littoral cell), as is done here. The original data-assimilation method
153 used in CoSMoS-COAST (Vitousek et al. 2017) operated independently for each transect;
154 meaning that any transects without coincident (e.g., intersecting) shoreline observations did not
155 receive any parameter adjustments. The current littoral-cell based data-assimilation method uses
156 all observations within a littoral cell (at a given time step) to assimilate the model parameter
157 values for all transects within that littoral cell (while simultaneously prioritizing the influence of
158 local observations at each transect). This littoral-cell based method provides some significant
159 advantages over individual-transect method, which primarily stem from using more assimilation
160 data and allowing those data to have a greater spatial influence on nearby transects. For
161 example, the new method facilitates assimilation of sparsely spaced beach-profile data (e.g.,
162 from GPS or total-station surveys) onto more densely spaced model transects. Further
163 advantages and the technical details of the littoral-cell based data-assimilation method are
164 discussed in Appendix B.

165 *2.1.3 Model forcing and scenarios*

166 Shoreline evolution is often critically linked to oceanographic forcing from waves and sea level
167 (Wright & Short 1984, Ashton et al., 2001, Splinter et al., 2014, Troy et al., 2021). Hence,
168 reliable shoreline modeling generally demands accurate hindcasts and robust projections of wave
169 and sea-level conditions. As shown in Figure 1, the model is forced by time series of parametric

170 wave conditions (i.e., H_s , T_p , and θ) and sea-level rise, S . In the current application, historic
171 wave conditions (1995-2020) are derived primarily from the CDIP hindcast (O'Reilly et al.,
172 2016), whereas projected wave conditions (2020-2100) are derived from a regional-to-local
173 nested WaveWatch III model (Erikson et al., 2015), which applies wind forcing from the GFDL-
174 ESM2M climate model (Delworth et al., 2006). Sea-level projections are generated from
175 quadratic curves (following Vitousek et al., 2017), which cover a range of physically tenable sea-
176 level outcomes (e.g., 0.5, 0.75, 1.0, 1.25, 1.5, 1.75, 2.0, 2.5, and 3.0 m) in California over the 21st
177 century (e.g., Griggs et al., 2017, Sweet et al., 2022). The specific details on the wave and sea-
178 level forcing conditions are presented in Appendix C.1 and C.2, respectively.

179 Anthropogenic effects on coastal change are difficult to represent using models. Humans make
180 deliberate, real-time interventions (e.g., beach nourishments, dredging/dumping,
181 bulldozing/berm-building, temporary shoreline armoring) in the coastal zone, especially during
182 major storm events – yet, practically all existing shoreline models do not explicitly account them
183 (Lazarus & Goldstein 2019). However, fine-scale observations (e.g., such as those provided
184 from satellites) offer a means to implicitly account for anthropogenic effects in the context of a
185 data-driven model, at least in so much as their impact is reflected in the local shoreline behavior
186 and observations thereof. Thus, the estimation of long-term residual shoreline trends such as v_{lt}
187 in Eq. (1) via data assimilation provides a means of accounting for processes that are difficult, if
188 not impossible, to account for explicitly.

189 As in Vitousek et al., (2017), the model considers two binary (i.e., on or off) management
190 scenarios: called the 'hold the line' and 'continued accretion'. The 'hold the line' versus 'no
191 hold the line' scenarios prohibit or allow the modeled shoreline to erode past a so-called 'non-

192 erodible shoreline’ (detailed in Appendix C.3) that delineates the location of non-sandy
193 substrates such as infrastructure, coastal cliffs, or vegetation. The ‘continued accretion’ versus
194 ‘no continued accretion’ scenarios allow or prevent the persistence of residual accretion trends
195 ($v_{it} > 0$), respectively. Justification and further details on the coastal management scenarios used
196 here are given in Appendix C.3.

197

198 **2.2 Quantifying model performance and uncertainty**

199 Quantifying model performance and uncertainty remains a critical effort in pursuit of reliable
200 coastal-change predictions. In general, methods to assess model performance and uncertainty
201 quantification are somewhat tailored to the model type, e.g., ‘simulation’ versus ‘exploratory’
202 (Murray et al., 2016). ‘Simulation’ models typically seek to reproduce site-specific behavior and
203 thus generally require characterization of model performance (e.g., compared to observations).
204 Idealized, ‘exploratory’ models often seek to address uncertainty related to climate scenarios or
205 to the magnitude and/or parametrization of processes or factors (for which direct observations
206 are often lacking). The current modeling application combines elements from both of the
207 ‘simulation’ and ‘exploratory’ archetypes: we seek the long-term simulation/prediction of site-
208 specific behavior under different climate and management scenarios. Hence, to align with the
209 simulation archetype, we apply a suite of methods to evaluate model performance and
210 uncertainty, as described below.

211 *2.2.1 Model performance*

212 The most common metric to evaluate model performance is the root-mean-square error (RMSE),
 213 which is given by

$$214 \quad \varepsilon_{\text{RMSE}} = \sqrt{\frac{1}{N} \sum_{i=1}^N ((Y_{\text{obs}})_i - (Y_{\text{mod}})_i)^2} \quad (2)$$

215 where Y_{mod} and Y_{obs} are the modeled and observed shoreline positions, respectively, among a
 216 time series of N data points.

217 Another popular model-performance metric is the index of agreement (Willmott 1981), which is
 218 given by

$$219 \quad d = 1 - \frac{\sum_{i=1}^N ((Y_{\text{mod}})_i - (Y_{\text{obs}})_i)^2}{\sum_{i=1}^N \left(\left| (Y_{\text{mod}})_i - \overline{(Y_{\text{obs}})} \right| + \left| (Y_{\text{obs}})_i - \overline{(Y_{\text{obs}})} \right| \right)^2} \quad (3)$$

220 where the overbar indicates the mean of a quantity. The index of agreement ranges from
 221 $0 \leq d \leq 1$, with values close to zero indicating poor and values close to one indicating excellent
 222 performance. The index of agreement was recently used by Montaña et al., (2020) to evaluate
 223 the performance of shoreline models in a blind-test competition (at the test site of Tairua Beach,
 224 New Zealand with 15 years of calibration data and 3 years of data-blind comparisons), and the
 225 best performing shoreline models achieved $d \approx 0.5 - 0.7$. As shown in Results, we assess
 226 model-performance metrics including the RMS error ($\varepsilon_{\text{RMSE}}$) and the index of agreement (d),
 227 across California with the aid of satellite-derived shoreline observations. We also characterize
 228 different types of model uncertainty including structural, epistemic, and intrinsic uncertainty, as
 229 described below.

230 2.2.2 Model uncertainty

231 Several recent studies have investigated the uncertainty associated with individual (Davidson et
232 al. 2013; Kroon et al., 2020, Zarifsanayei et al., 2021) or combined components (Banno et al.,
233 2015, Le Cozannet et al. 2019; D'Anna et al., 2020, 2021a, 2022, Vitousek et al., 2021, Toimil et
234 al., 2017, 2021) of popular shoreline models (such as those described by processes/terms in Eq.
235 (1)). From these studies, consensus emerges that: (1) waves generally dominate uncertainties at
236 short time scales and sea-level-driven recession or persistent shoreline accretion/erosion trends
237 dominate uncertainties at long time scales, (2) intrinsic uncertainty (e.g., due to unknown model
238 forcing conditions, like scenarios of future wave and sea-level conditions) is generally
239 irreducible unlike epistemic uncertainty (e.g., due to unknown/uncertain model parameters),
240 which is reducible via refining model parameters (using data-assimilation, for example), and (3)
241 climate-driven intrinsic uncertainties (e.g., due to cascading uncertainties in greenhouse gas
242 emissions, global temperature projections, future wave and sea-level conditions and different
243 GCM projections thereof, future sediment supplies, and future coastal management pathways)
244 are both broad and deep (Toimil et al., 2020b).

245 In the current approach, we investigate the model's epistemic, intrinsic, and structural
246 uncertainty, as described below. Firstly, we address epistemic/parametric uncertainty via
247 applying a range of model parameters in an ensemble simulation and use data assimilation to
248 calibrate site-specific values of model parameters over a large scale, with the aid of large
249 amounts of satellite-derived shoreline observations (described below). Following Vitousek et al.
250 (2021), we also address epistemic uncertainty of the model solution/parameters by applying a
251 calibrated additive-noise parameter σ (which is part of term [5] in Eq. (1) and is described in

252 Section 2.1). Secondly, we assess intrinsic uncertainty by applying different sea-level and
253 coastal-management scenarios, as described above and in Appendix C. We also assess wave-
254 driven intrinsic/aleatoric uncertainty associated with extreme storm-driven erosion due to annual,
255 20-year, and 100-year return period wave events, by fitting generalized extreme value (GEV)
256 distributions to annual minima in the wave-driven, cross-shore equilibrium shoreline position,
257 following Davidson et al. (2017) as detailed in Appendix C.1. Thirdly, we investigate the
258 model's structural uncertainty, defined as the inadequacy, bias, or discrepancy between the
259 model and the real world (i.e., observations). The structural uncertainty (which we also refer to
260 as the uncertainty due to 'unresolved processes') is, philosophically, a bit different than the
261 intrinsic or epistemic uncertainty. On the one hand, the intrinsic and epistemic uncertainties
262 represent the model's interpretation of how inaccurate *it might be* given different forcing
263 conditions or parameters, respectively. On the other hand, the structural uncertainty is how
264 inaccurate the model *actually is*, compared with real-world observations. We also note that
265 investigating the structural uncertainty is rare among large-scale shoreline modeling applications,
266 due to data-availability constraints. Here, we investigate structural uncertainty by comparing the
267 model to satellite-observed shorelines across California during the validation period of 2015-
268 2020. We report the model structural uncertainty using the common and conservative approach
269 of reporting $\pm 2\varepsilon_{\text{RMSE}}$ (a.k.a., two-sigma) confidence bands surrounding the model's median
270 projections, which seeks to contain ~ 95% of the possible variations, following Taylor & Kuyatt
271 (1994).

272

273

274 **2.3 Satellite-derived shoreline observations**

275 The most intensive local monitoring programs in California have performed ~200 topographic
276 beach surveys over the last two decades (e.g., Barnard et al., 2012, Young et al., 2021), yet
277 satellite imagery can typically provide 500-1000 shoreline observations spanning almost four
278 decades, at any given beach. Here, we apply the [CoastSat](#) toolbox (Vos et al., 2019a) to derive
279 historical shoreline observations from individual, cloud-free satellite images in the Landsat
280 archive. The satellite-derived, historical shoreline position data used as part of this study are
281 available via Vos (2022) [[data set](#)]. Although historical Lidar and GPS data are also assimilated
282 in the model, these CoastSat-derived shoreline observations represent the vast majority (i.e.,
283 99.9%) of assimilated data, which is described further in Appendix B.

284 *2.3.1 CoastSat*

285 The CoastSat image-processing methodology, used in the current application, derives shoreline
286 position using the marching-squares algorithm (Lorenson & Cline 1987) that contours the
287 threshold of the Modified Normalized Difference Water Index (MNDWI) that optimally splits
288 the image-segmentation classes of ‘water’ and ‘sand’ using Otsu’s (1979) method (as detailed in
289 Vos et al., 2019a). CoastSat also provides methodology to estimate beach-face beach slopes
290 (based on Vos et al., 2020), which are subsequently used to correct satellite-derived observations
291 for tidal stage (e.g., using Eq. (4)). CoastSat has been validated against traditional shoreline
292 surveys in a variety of coastal settings worldwide including Truc Vert, France; Moruya,
293 Australia; Narrabeen-Collaroy, Australia; Tairua, New Zealand; Duck, North Carolina, United
294 States, and generally provides accuracy (i.e., root-mean-square error) on the order of 7-14 meters
295 (Vos et al., 2019b) compared with in-situ surveys. For the current application, we compare

296 CoastSat-derived shoreline observations against in-situ GPS surveys at Ocean Beach, San
297 Francisco, California, U.S., a well-monitored site with over 200 monthly surveys since 2004
298 (Hansen and Barnard, 2010; Barnard et al., 2012). Here, we compare the accuracy of satellite-
299 derived shoreline positions to the ‘ground-truthed’ GPS surveys of centimeter-scale accuracy.
300 The primary difference between the GPS versus satellite-derived shoreline data sets is that the
301 latter is based on a visual-detection proxy for the shoreline that is influenced by the local water
302 level, whereas the GPS surveys are elevation-based (or datum-based) and thus are independent of
303 the local water level. Below and in Appendix D, we address differences between GPS- versus
304 satellite-derived shorelines and the so-called ‘proxy-datum bias’ (Moore et al., 2006; Ruggiero &
305 List, 2009), respectively.

306 The shoreline positions in both GPS and satellite data sets at Ocean Beach are measured as the
307 distance Y from a fixed onshore baseline to the location of the mean sea-level (MSL) elevation
308 contour. Although more surveyed shoreline contours (e.g., mean high water - MHW) can be
309 extracted from the GPS-derived elevation point-cloud data available at Ocean Beach, we use the
310 MSL shoreline contour in order to maintain consistency with the satellite-derived water line. In
311 both data sets, observations over ~ 5 km of beach are interpolated onto shore-perpendicular
312 model transects spaced approximately 200 m in the alongshore direction.

313 As discussed in Appendix C, we find that CoastSat-derived MSL shorelines at Ocean Beach are
314 generally biased landward of the GPS-derived MSL shorelines, and that the shoreline error
315 ($Y_{\text{GPS}} - Y_{\text{sat}}$), is highly correlated with wave height (as shown in Figure 21 in Appendix D). This
316 finding suggests that the satellite-derived shoreline positions are affected by wave setup (i.e., the
317 persistent elevation of nearshore water levels inshore of breaking waves), which causes a

318 landward shift of the identified water-line/shoreline, and which might be bias-corrected with
 319 knowledge of synoptic wave conditions, wave setup elevation, and foreshore beach slope.

320 2.3.2 Tide, wave-setup, and residual water-level correction to satellite-derived shorelines

321 To remove bias due to synoptic water-level conditions, we correct the satellite-derived shoreline
 322 position along each transect according to

$$\begin{aligned}
 323 \quad Y_{\text{corrected}}(t) = Y_{\text{raw}}(t) + \frac{1}{\beta_f} & \underbrace{\left(\underbrace{\eta_{\text{tide}}(t)}_{\text{[1] tide correction}} + \underbrace{\bar{\eta}(t)}_{\text{[2] wave setup correction}} + \underbrace{\eta_{\text{MMSLA}}(t)}_{\substack{\text{[3] monthly mean} \\ \text{sea-level} \\ \text{anomaly} \\ \text{correction}}} + \underbrace{\eta_{\text{opt}}}_{\text{[4] residual correction}} \right)}_{\text{the total, nearshore still-water level}} \quad (4)
 \end{aligned}$$

324 where each (time-varying) correction component is due to different processes affecting the total,
 325 nearshore still-water level, including [1] tide, [2] wave setup, [3] monthly mean sea-level
 326 anomalies, as well as [4] any remaining/residual bias. Corrections are made using Eq. (4) for
 327 each of the model's shore-normal transects with known, time-invariant foreshore beach slopes.
 328 At Ocean Beach, the beach slope $\beta_f = 1/28$ for all transects, which is estimated from Lidar
 329 data. Here, CoastSat's built-in tidal corrections (i.e., term [1] in Eq. (4)) come from time series
 330 of astronomic water-levels (η_{tide}) predicted using the Finite-Element Solution (FES14) ocean
 331 model (Lyard et al., 2021). Here, we apply CoastSat's built-in tidal corrections derived from the
 332 FES14 tide model rather than observed water levels (including water-level anomalies) from tide
 333 stations so that the method is applicable to sites/transects lacking nearby water-level
 334 observations. However, there are pros and cons (namely portability and accuracy, respectively)
 335 to utilizing modeled over observed water levels.

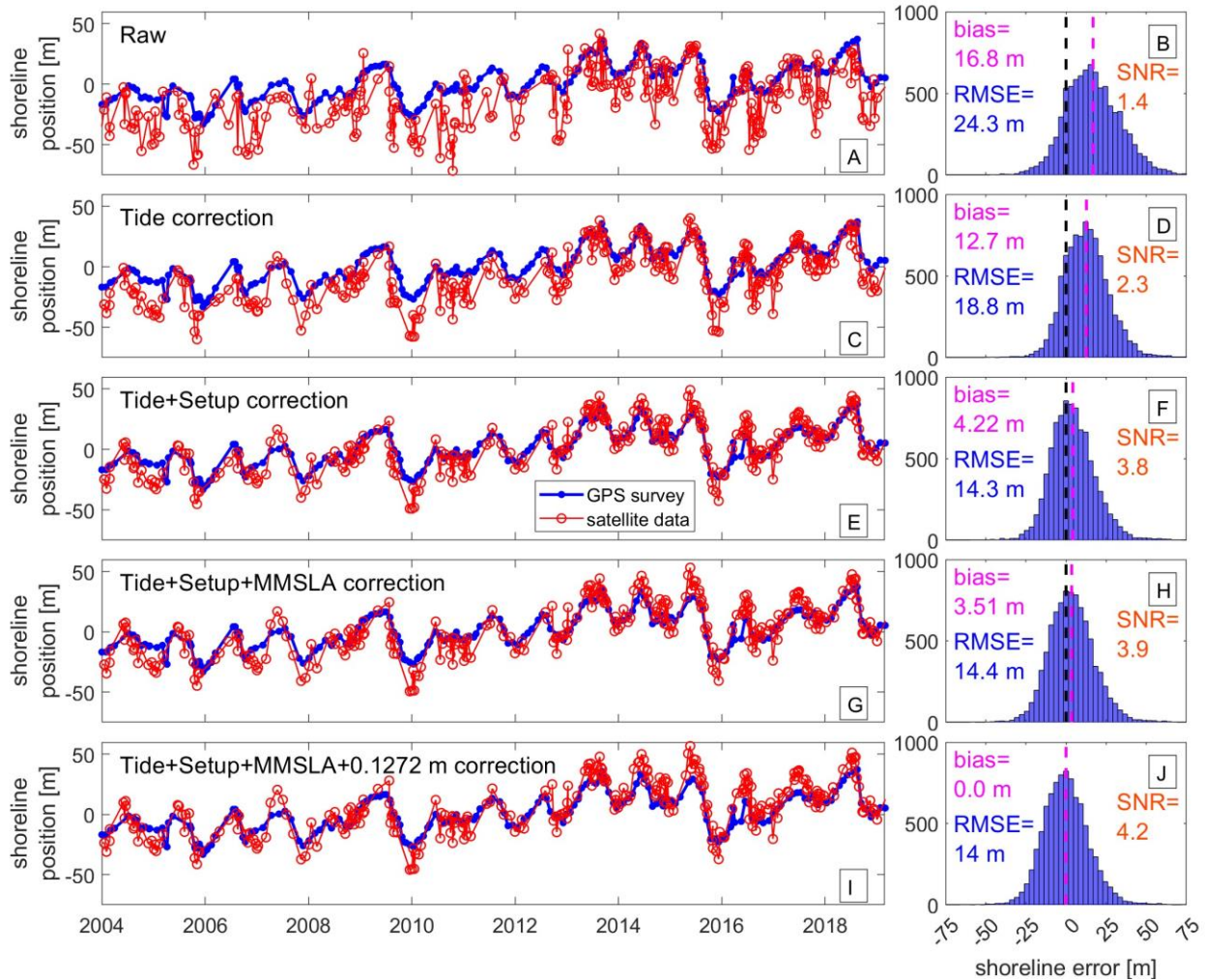
336 We correct for wave setup (term [2] in Eq. (4)) using the Stockdon et al., (2006) empirical
337 parameterization of wave setup for dissipative beaches,

$$338 \quad \bar{\eta} = 0.016\sqrt{H_0 L_0} . \quad (5)$$

339 In Eq. (5), deep-water wave height (H_0) and wave period (T_0), from which wavelength

340 $L_0 = \frac{gT_0^2}{2\pi}$ is calculated using linear wave theory, can come from model hindcasts or buoy

341 records. In the accuracy analysis presented here in Figure 3, we use wave conditions from the
342 San Francisco wave buoy (#46026), located 33 km offshore from Ocean Beach. We also tested
343 slope-dependent wave-setup parameterizations (from Stockdon et al. (2006)), and the results (not
344 shown) provided slightly less skill than the dissipative-beach-specific formulations. The time
345 series of monthly mean sea-level anomalies (MMSLA), η_{MMSLA} term [3] in Eq. (4), comes from
346 estimates from the NOAA Tides & Currents database’s San Francisco tide-gauge station
347 (#9414290) located approximately 6 km away from Ocean Beach. Finally, we estimate an
348 optimal, ‘best-fit’ water-level correction (term [4] in Eq. (4)) of $\eta_{\text{opt}} = 12.72$ cm, which is
349 required for the satellite-derived shorelines to obtain unbiased estimates of shoreline position and
350 is discussed further in Appendix D.



351

352 Figure 3 – The alongshore-averaged shoreline position with the (time-averaged) mean removed
 353 for the GPS surveys compared to the satellite-derived observations at Ocean Beach, San
 354 Francisco, California for different correction methods (i.e., different terms in Eq. (4)). Left
 355 panels show time series of comparisons, and right panels show the histogram of the error (GPS-
 356 derived minus satellite-derived shoreline position) as well as the bias, root-mean-square error
 357 (RMSE), and signal-to-noise ratio (SNR).

358

359 We compare a sequence of corrections (based on Eq. (4)) to the raw satellite-derived shoreline
 360 position compared with the GPS data in Figure 3. Panels A, C, E, G, and I on Figure 3 show the
 361 alongshore-averaged, satellite-derived shoreline position (red) compared to the alongshore-

362 averaged GPS shoreline position (blue) across the surveyed portion of Ocean Beach with
363 different correction methods applied (which are described below). Note that the shoreline
364 positions shown in Figure 3 are given relative to the mean of the time series. Panels B, D, F, H,
365 and J on Figure 3 show histograms of the error in the shoreline position ($Y_{\text{GPS}} - Y_{\text{sat}}$) when using
366 different correction methods. When calculating the shoreline error, the satellite-derived
367 shoreline positions (collected approximately weekly, i.e., every 16 days across two overlapping
368 Landsat missions) are linearly interpolated onto the dates of the (monthly) GPS surveys so that
369 direct comparisons can be made. Figure 3 B demonstrates that the raw satellite-derived shoreline
370 positions have a mean (landward) bias of 16.8 m and a root-mean-square error (RMSE) of 24.3
371 m. Both the bias and the RMSE are sequentially reduced each time a new correction term is
372 applied (via Eq. (4)). After applying CoastSat's built-in tidal corrections, the (landward) bias of
373 the satellite-derived shorelines is reduced to 12.7 m and the RMSE is reduced to 18.8 m (see
374 Figure 3 C and D). Nevertheless, a fairly large bias remains. The ineffectiveness of the tidal
375 correction on reducing the overall bias is perhaps expected. The tide oscillates somewhat evenly
376 around mean sea level, and thus does not contribute significantly to the systematic landward bias
377 of the satellite observations found here. Wave setup, on the other hand, represents a persistent
378 still-water-level change that is likely responsible for much of the landward bias between the
379 satellite's visual proxy interpretation of the shoreline position compared to the GPS's elevation-
380 based (datum-based) interpretation of the shoreline position, which is uninfluenced by the
381 presence of waves or the stage of the local water level. Figure 3 E and F show that correcting for
382 time-varying wave setup (via term [2] in Eq. (4)) significantly reduces the bias of the satellite
383 data from 12.7 to 4.2 m. However, the RMSE still remains sizable before (18.8 m) and after
384 (14.3 m) the setup correction. Subsequent corrections for monthly mean sea-level anomalies

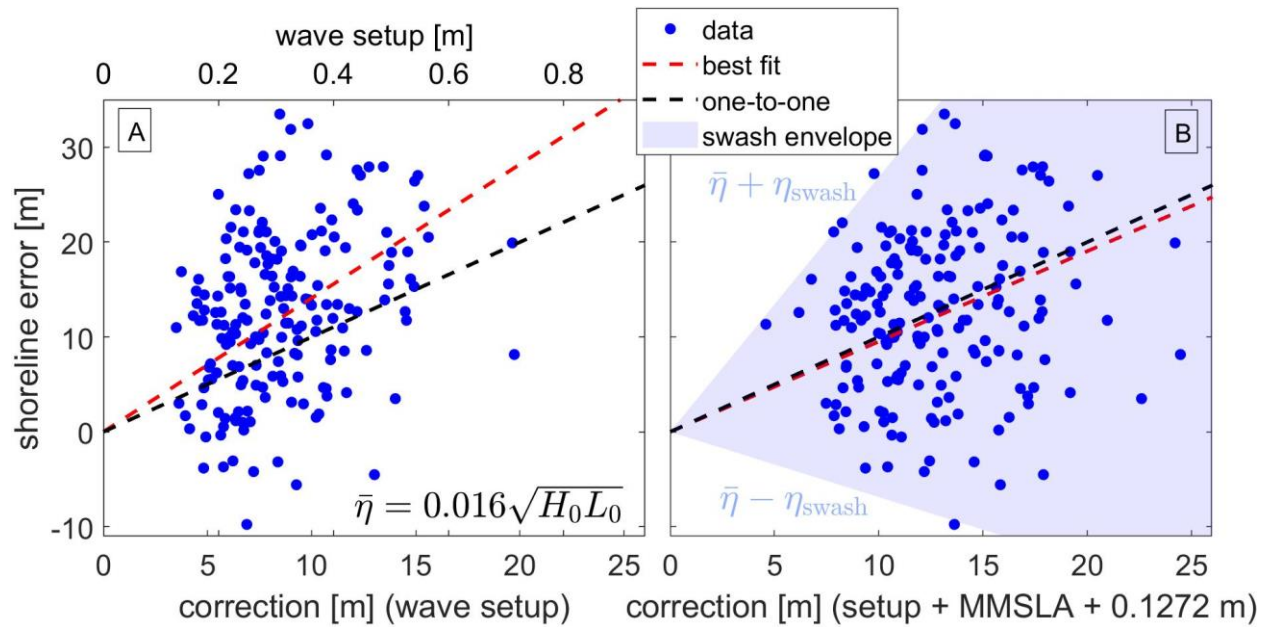
385 (MMSLA), observed at the San Francisco tide-gauge station (#9414290), do relatively little to
386 reduce the remaining bias (compare Figure 3 G and H). The residual landward bias of the
387 satellite-derived shoreline position can be completely eliminated by applying an additional
388 ‘water level’ correction of $\eta_{\text{opt}} = 12.72$ cm, obtained via optimization. We believe that this static
389 correction between the GPS data and the satellite-derived data, corresponding to an effective
390 $\eta_{\text{opt}} = 12.72$ cm water-level difference or to a 3.5 m horizontal landward offset (as shown in
391 Figure 3 H), may represent the ‘proxy-datum bias’ between the visual and elevation-based
392 shoreline data (cf. Moore et al., 2006; Ruggiero & List, 2009) for Ocean Beach. As discussed
393 further in Appendix D and depicted in Figure 22, we believe that more than half of this
394 remaining bias is due to mismatches in modeled and observed water level.

395 After applying the full sequence of corrections in Eq. (4) to obtain an unbiased estimate of the
396 satellite-derived shoreline position, the RMSE of the satellite-derived shorelines is
397 approximately 14 m, which is equivalent to approximately half of the 30 m pixel resolution of
398 the Landsat imagery, which also closely resembles the 15 m pixel resolution of the pan-
399 sharpened Landsat imagery used in CoastSat. The level of accuracy, found here, is consistent
400 with numerous previous findings (e.g., Hagenaars et al., 2017, Luijendijk et al., 2018, Vos et al.,
401 2019a,b, Nelson & Miselis 2019).

402 In Figure 3 B, D, F, H, and J, we also report the signal-to-noise ratio (SNR), which is here
403 defined as the ratio of the variance of the satellite-derived shoreline ‘signal’ to the variance of the
404 ‘noise’ (represented by the RMSE) and is given by

$$\text{SNR} = \frac{\frac{1}{N} \sum_{i=1}^N ((Y_{\text{sat}})_i - \overline{Y_{\text{sat}}})^2}{\frac{1}{N} \sum_{i=1}^N ((Y_{\text{GPS}})_i - (Y_{\text{sat}})_i)^2} = \frac{\sigma_{\text{SAT}}^2}{\varepsilon_{\text{SAT}}^2} \quad (6)$$

406 We find, as shown in Figure 3, that the complete water-level correction method (described
 407 above) triples the signal-to-noise ratio from 1.3 for raw satellite-derived shorelines to 4.2 for the
 408 fully corrected shorelines. Furthermore, this analysis (stemming from Eq. (6)) shows that
 409 beaches that experience larger ‘signals’ of erosion and accretion will generally be more
 410 amenable to observation from satellites according to the SNR metric given here.



411
 412 Figure 4 – The satellite-derived shoreline error (GPS-satellite) vs. the error after different
 413 combinations of corrections. Panel A shows the error after correcting for wave setup only. Panel
 414 B shows the error after correcting for wave setup, mean sea-level anomalies (MMSLA), and an
 415 optimized water-level correction. The swash envelope (shaded blue region) illustrates how the
 416 remaining shoreline excursions appear to be a consequence of wave swash.

417 2.3.3 *The potential influence of wave swash on satellite-derived shorelines*

418 Figure 4 A compares the shoreline error (after tide correction; y-axis) to the wave setup (on the
419 upper x-axis) and to the shoreline correction due to wave setup only (on the lower x-axis).
420 Figure 4 B likewise compares the shoreline error (y-axis) to the complete shoreline correction
421 (due to wave setup and water level) on the x-axis. Notice that the best-fit relationships (red
422 dashed lines) between the shoreline error and the shoreline correction are not exactly one-to-one
423 (black dashed lines) for the wave-setup-only correction (shown on Figure 4 A). However, the
424 shoreline error and the complete shoreline correction (i.e., all terms in Eq. (4)) on Figure 4 B (red
425 dashed lines) are nearly one-to-one (black dashed lines). We also depict the wave-swash
426 envelope (light blue band) on Figure 4 B, which represents the theoretical, horizontal extent of
427 wave swash along a transect where the instantaneous swash line may occur at an arbitrary instant
428 in time (i.e., for an arbitrary phase of the swash). The swash envelope is centered on the wave
429 setup, $\bar{\eta}$, and the upper and lower bounds are calculated as the inverse beach slope (β_f^{-1})
430 multiplied by $\bar{\eta} \pm \eta_{\text{swash}}$, where the maximum swash excursion is calculated as $\eta_{\text{swash}} = 1.69\bar{\eta}$,
431 which is a consequence of the relative magnitude of the empirical swash parameterization (for
432 dissipative beaches) of Stockdon et al. (2006),

433
$$\eta_{\text{swash}} = 0.027\sqrt{H_0 L_0} \quad , \quad (7)$$

434 which is a factor of $0.027 / 0.016 \approx 1.69$ larger than the empirical setup parameterization in Eq.
435 (5). Hence, in Figure 4 B, the swash envelope has a lower bound slope of -0.69 (which
436 represents $\bar{\eta} - \eta_{\text{swash}} = \bar{\eta} - 1.69\bar{\eta} = -0.69\bar{\eta}$) and an upper bound slope of 2.69 (which represents
437 $\bar{\eta} + \eta_{\text{swash}} = \bar{\eta} + 1.69\bar{\eta} = 2.69\bar{\eta}$), and is centered on one-to-one (black dashed lines, which

438 represent the mean setup correction $\bar{\eta}$). As demonstrated in Figure 4 B, most of the
439 observations (blue dots) of the shoreline error (i.e., the difference between the ground-truth,
440 elevation-based GPS shorelines and the image-based satellite shorelines) fall within the swash
441 envelope, shown in light blue, which indicates that the magnitude of the post-correction residual
442 error in shoreline position is similar with the magnitude of potential swash excursions. Further,
443 the analysis presented in Figure 4 B potentially explains why the largest (20 to 30 m) shoreline
444 errors (based on the tide-only correction) are generally positive, since the upper bound of the
445 swash envelope has a much larger slope (i.e., 2.69) than the lower bound (with slope -0.69).

446 The strong role played by the wave setup (shown in Figure 3) and the swash envelope shown on
447 Figure 4 suggests that time-dependent wave swash greatly influences the visual detection of the
448 shoreline in satellite imagery. Unlike wave setup, swash is oscillatory. Hence, its phase cannot
449 easily be corrected. Therefore, the presence of sizable wave swash in satellite imagery may
450 represent an accuracy bottleneck, which may persist despite the increasing resolution of satellite
451 imagery. As is a common practice in shoreline identification with ground-based cameras, a
452 wave-height threshold might be applied to retain only the observations occurring during low
453 wave conditions. However, the relative infrequency of satellite revisits (especially when
454 compared with ground-based camera observations) would perhaps demotivate the decision to
455 favor observational accuracy over observational frequency. In the application presented here, we
456 do not apply a wave-height thresholding approach and instead retain all satellite-derived
457 shoreline observations for data assimilation. For the following large-scale modeling application,
458 we uniformly apply the site-specific error analysis and bias correction method (described above)
459 to the rest of the California coastline, where we have satellite data but lack traditional beach
460 survey data. We offer the proposed satellite-data-assimilated modeling approach as a means to

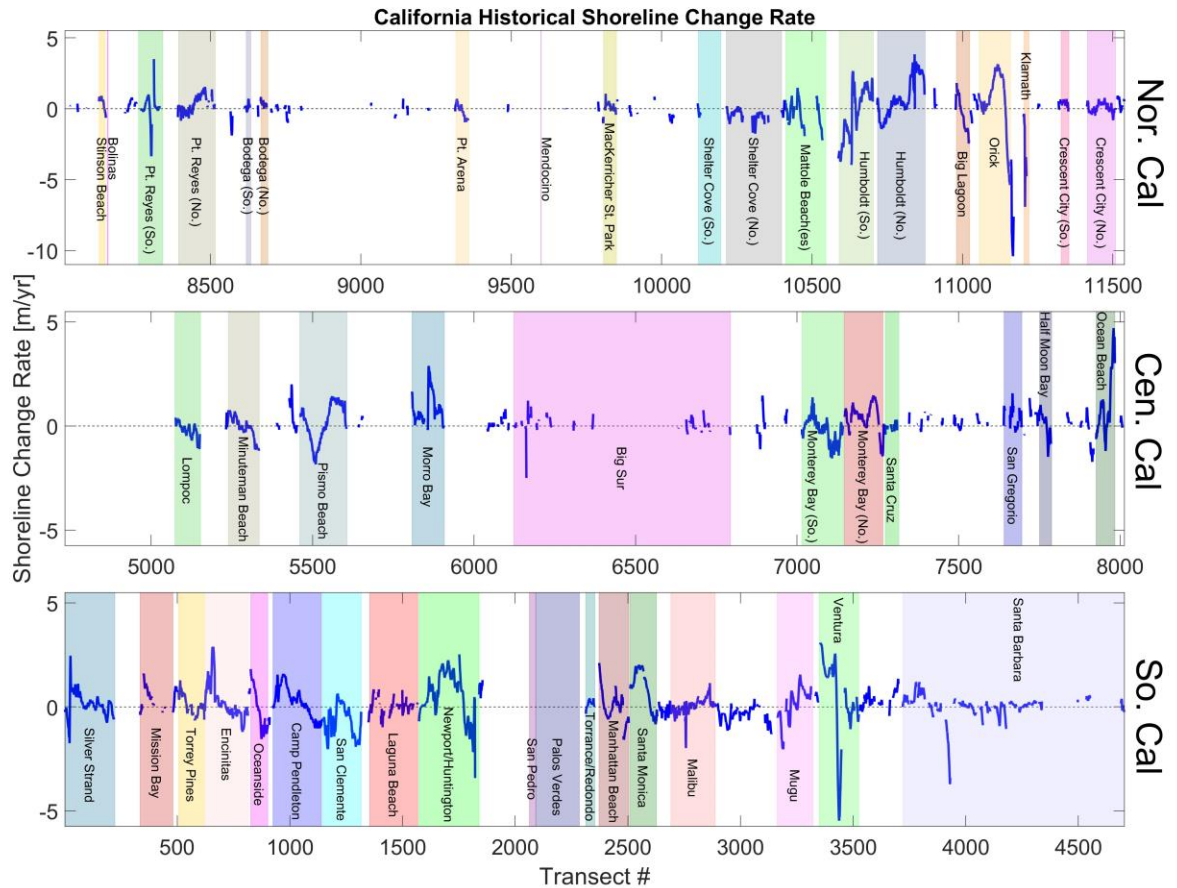
461 achieve reliable forecasts in otherwise ‘data-poor’ environments where in-situ observations are
462 sparse or non-existent.

463 **3. Results**

464 **3.1 Long-term shoreline change rates**

465 As a preliminary analysis, we estimate the historical rate of shoreline change by fitting linear
466 trends to observed shoreline positions from 1995-2020. The shoreline trend analysis presented
467 here provides a modern update, benefitting from decades of satellite-derived shoreline
468 observations, to the historical rates for California presented in Hapke et al., (2006). Although we
469 apply unweighted regressions to all available shoreline observations from different sources (e.g.,
470 Lidar, GPS, satellite) at each transect, 99.9% of the observations come from satellites, hence they
471 dominate the trend analysis, as expected. Trends fit to satellite-derived shoreline observations
472 have been repeatedly shown to reproduce observed trends (derived from traditional sources of
473 shoreline data for overlapping time periods) in many different settings (e.g., Smith et al., 2021,
474 Castelle et al., 2022). In the current application, the shoreline trends are fit to the full set of tide-,
475 wave- and water-level-corrected satellite-derived shoreline observations (see Section 2.3).
476 However, Castelle et al., (2022) showed that using raw, uncorrected satellite-derived shorelines
477 is generally sufficient for long-term trend analyses.

478



479

480 Figure 5 – Long-term, historical shoreline change rates ($(v_{lt})_0$) for southern California (bottom
 481 panel), central California (middle panel), northern California (top panel) from 1995 - 2020
 482 (negative = erosion and positive = accretion). The colored bands identify large littoral regions,
 483 which are enclosed by harbors, headlands, river mouths, etc.

484

485 Figure 5 plots the long-term shoreline change rate (in m/yr with positive and negative values
 486 indicating accretion and erosion, respectively) versus transect number. Figure 5 is split into
 487 three portions, i.e., lower, middle, and upper, which represent southern, central, and northern
 488 California, respectively. The colored bands in Figure 5 identify large littoral regions, which are
 489 enclosed by harbors, headlands, river mouths, etc. Across all of California, we find that 24% of

490 beaches have been eroding (rate < -0.25 m/yr), 52% have been accreting (rate > 0.25 m/yr),
491 and 24% have been stable ($|\text{rate}| \leq 0.25 \text{ m/yr}$). Likewise, for southern California only, which
492 generally exhibits more vulnerability to erosion, we find that 30% of beaches show historical
493 erosion, 42% show accretion, and 28% have been stable. By themselves, the shoreline trends,
494 shown in Figure 5, do not identify the causal mechanisms of shoreline accretion or erosion.
495 However, they do suggest a strong anthropogenic signal on the shoreline trend [as was
496 established in Flick (1993) and Hapke et al., (2006)] in certain locations, based on evidence that
497 the largest rates of change occur near harbors or beaches receiving significant sediment input
498 (e.g., from fluvial inputs or nourishments). A notable saw-toothed pattern of erosion and
499 accretion in northern and southern portions of littoral cells, respectively, is visible throughout
500 much of California, but is particularly evident in southern California for the Silver Strand,
501 Mission Bay, Torrey Pines, Encinitas, Oceanside, Camp Pendleton, and San Clemente regions.
502 This saw-toothed pattern is consistent with a mechanism of longshore transport from north to
503 south driven by obliquely incident swell from the North Pacific, which is interrupted (but has
504 partially bypasses) around harbors or headlands. In central and northern California, where
505 nourishments are rare, anthropogenic influences on the shoreline trend can still be seen at harbor
506 entrances (e.g., in Monterey Bay, Half Moon Bay, and Humboldt). Additionally, large signals of
507 shoreline change (in both accretion and erosion) are visible in regions with strong fluvial
508 sediment input (e.g., Humboldt, Orick, Klamath). We observe the largest shoreline trends at the
509 northern portions of Orick and Ocean Beach, with ~10 m/yr of erosion and ~ 5 m/yr of accretion,
510 respectively.

511 Overall, Figure 5 demonstrates the strong signal of local shoreline trends, which is affected by a
512 multitude of processes such as interrupted longshore transport, headland bypassing, episodic
513 fluvial inputs, beach nourishments, etc. The variability in local shoreline behavior show in
514 Figure 5 also motivates the use of data-assimilation, as locally calibrated residual trends like v_{lt}
515 in Eq. (1) can provides a means of implicitly accounting for processes that are not easy to model
516 or quantify explicitly. As discussed below in Section 3.2.1 and in Appendix B.4, one quarter of
517 the long-term linear trend $(v_{lt})_0$ (shown in Figure 5) is used to provide initial parameter
518 estimates for the residual trend v_{lt} . Using data assimilation, v_{lt} is further refined over the model
519 hindcast period alongside the explicitly resolved shoreline change processes (and their associated
520 parameters), like longshore transport, which are not accounted in the historical trend analysis
521 (Figure 5), but are accounted for in the dynamic model (i.e., Eq. (1)).

522 **3.2 Case study: Ocean Beach**

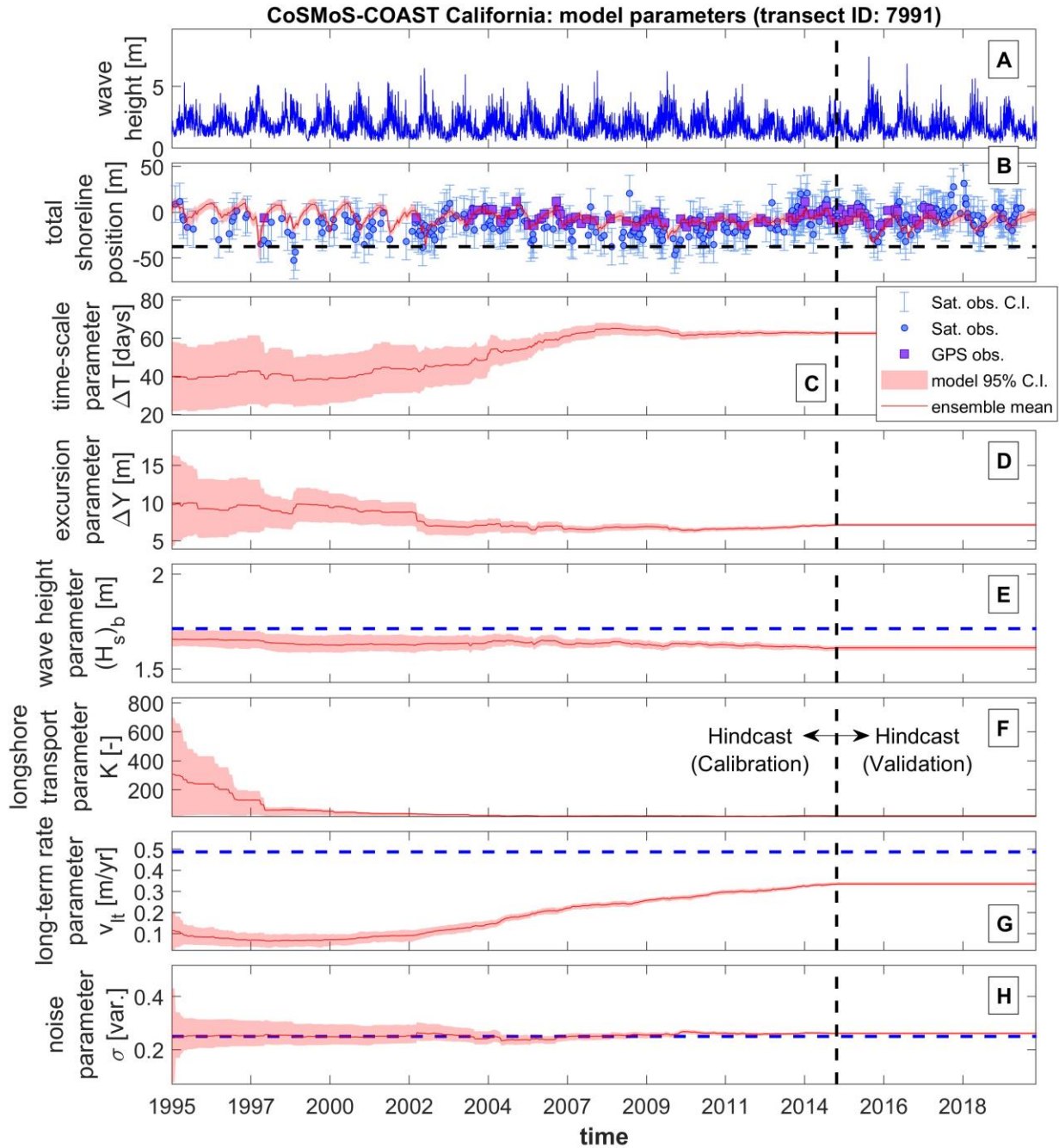
523 In this section, we provide a case study of the data-assimilated model at Ocean Beach, San
524 Francisco, a well-monitored beach, with a large seasonal signal of episodic erosion as well as
525 persistent erosion and accretion trends in the southern and northern portions, respectively. The
526 case study, presented here, is intended to investigate the performance of the model when
527 assimilating satellite-derived shoreline observations versus monthly GPS-derived shoreline
528 observations (which exist here, but generally do not at other beaches).

529 *3.2.1 Model hindcast*

530 Figure 6 shows time series of wave height, observed versus modeled shoreline position, and the
531 assimilated model parameters at transect #7991 at the southern end of Ocean Beach (which is

532 adjacent to the San Francisco Zoo and close to the Oceanside Water Pollution Control Plant; see
533 Figure 7 for a map of the precise location of transect #7991). The ensemble median shoreline
534 position and model parameters are shown with red lines in Figure 6. The pink bands in Figure 6
535 depict the evolving uncertainty at the 95% confidence level, derived empirically from histograms
536 of the assimilated values of the shoreline position and model parameter ensemble. The wave-
537 height time series (Figure 6 A) demonstrates a distinct seasonal pattern of large wave heights in
538 the winter and small wave heights in the summer. The shoreline response (Figure 6 B), which is
539 dominated by wave-driven/equilibrium behavior, is nicely illustrated as nearly the mirror-image
540 of the wave height (in Figure 6 A) with erosion in winter and recovery in summer. Figure 6 B
541 depicts the two different kinds of shoreline observations, which represent the intersection of
542 transect #7991 with satellite-derived shorelines (blue dots + uncertainty) or with GPS-derived
543 mean-sea-level (MSL) shorelines (purple dots). By comparing the assimilated model (red line in
544 Figure 6 B) to the observations (i.e., blue and purple dots Figure 6 B), we see that the model
545 reproduces the observed signal of seasonal shoreline change and the extents of the maximally
546 accreted/eroded beach states in this case study. However, we expect good performance of the
547 model because it is assimilated, i.e., nudged toward the observations. The time series shown in
548 Figure 6 are split into a ‘Hindcast (Calibration)’ period (1995-2015) and a ‘Hindcast
549 (Validation)’ period (2015-2020), where data assimilation is turned on and off, respectively.
550 Note that the ‘Hindcast (Validation)’ is a separate test phase where the agreement between the
551 unassisted model and the observations can provide a fair assessment of the model's skill to
552 faithfully represent shoreline behavior recorded in observations that are previously unseen by the
553 model (as discussed below). Ultimately, its performance during the ‘Hindcast (Validation)’

554 period is perhaps the only thing that affords confidence in the model's predictive capabilities
 555 during projection periods (2020-2100).



556

557 Figure 6 - Time series of model predictions (B) and model parameters (C-H) for transect #7991
 558 at Ocean Beach, San Francisco, California (A) Time series of daily maximum significant wave

559 height [m], (B) satellite observed (blue dots + uncertainty bands), in-situ GPS observed (purple
560 squares), and simulated shoreline position, Y , (ensemble median shown in red line) and 95%
561 confidence bands (shown in pink bands), (C-H) time series of assimilated model parameters
562 (ensemble median in red line) and uncertainty (shown in pink bands), which are sequentially
563 adjusted via an ensemble Kalman filter as more data are ingested into the model. Note the
564 dashed blue lines on panels E, G, and H represent the local mean of significant wave height time
565 series, the local long-term linear shoreline change rate, and the initial value of the noise
566 parameter, respectively. The dashed black line on panel B represents the location of the non-
567 erodible shoreline on this transect. The time series are split into a ‘Hindcast (Calibration)’ period
568 (1995-2015) and a ‘Hindcast (Validation)’ period (2015-2020), when data assimilation is turned
569 on and off, respectively. Note that the model parameters (C-H) remain constant during the
570 Hindcast (Validation) period.

571 Figure 6 C–H show time series of the assimilated model parameters including the equilibrium
572 time-scale parameter (ΔT), the equilibrium erosion length-scale parameter (ΔY), and the
573 equilibrium wave-height parameter ($(H_s)_b$), the longshore-transport coefficient (K), the long-
574 term residual shoreline-change rate (v_{lt}), and the additive-noise parameter (σ), respectively.
575 Note that the entire 200-member parameter ensemble is sequentially adjusted during each data-
576 assimilation step (i.e., at the times when observations are available), which is reflected in Figure
577 6 C–H as adjustments in the values and uncertainty bands of each model parameter. During the
578 ‘Hindcast (Validation)’ period (and for future forecast periods), data assimilation is turned off,
579 and thus the values of all model parameters remain constant (in time, but variable in space).
580 Ideally, when enough data are available during the hindcast period, the assimilated values of the
581 model parameters will be sufficiently converged before the forecast period begins. Figure 6
582 indicates that the parameter values and particularly the uncertainty appear to converge over the
583 course of the simulation. As demonstrated in Vitousek et al. (2021), the evolution of the width
584 of the uncertainty bands is set by a balancing act between the processes of additive noise and
585 data assimilation (or damping), which expand and contract the spread of the ensemble,

586 respectively. In this case, the parameter ensembles appear to converge to roughly constant-in-
587 time value toward the end of the ‘Hindcast (Calibration)’ period because the data-assimilation
588 method (and the amount of available data) suppresses/converges the uncertainty faster than the
589 additive noise expands it. During the ‘Hindcast (Validation)’ and the projection periods, the
590 process of additive noise (i.e., term 5 in Eq. (1)) is completely turned off, and thus the parameter
591 ensemble is completely constant in time. However, retaining additive noise after the ‘Hindcast
592 (Calibration)’ would lead to a linear growth in the variance of the ensemble (or a square-root-
593 time growth in the uncertainty bands with time) as shown in Vitousek et al., (2021). Note that
594 while the parameter ensemble is held static for the projection period, the model will generally
595 still exhibit a growth of its uncertainty bands over time, which are, for example, associated with
596 the continuation of an uncertain/ensemble long-term trend or sea-level-driven recession
597 coefficient (as shown in the Ocean Beach case study below), or from applied ensemble forcing
598 conditions (e.g., ensemble wave or sea-level rise projections).

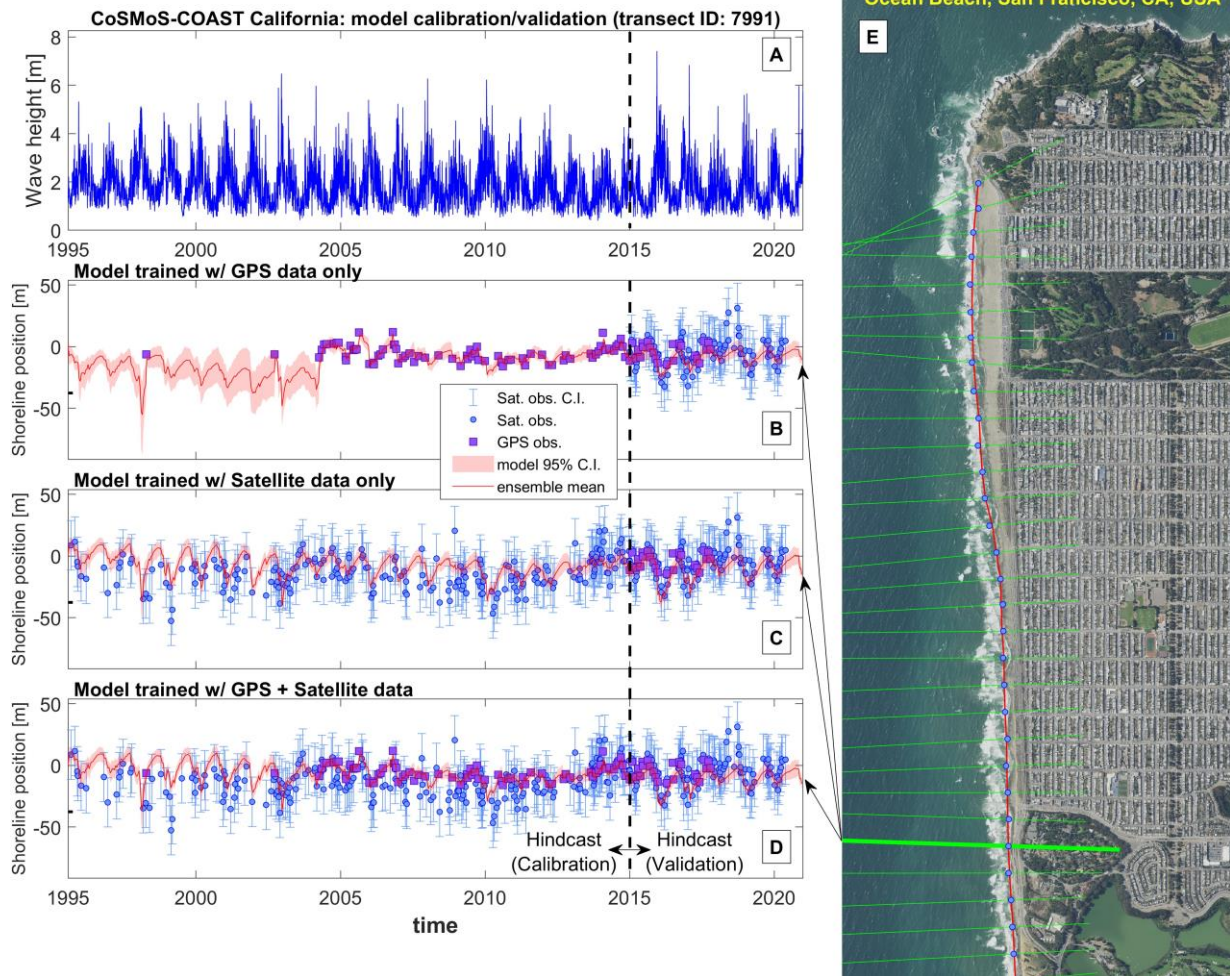
599 Finally, we highlight a few salient features of the convergence of the model parameter ensemble
600 as demonstrated in Figure 6. Figure 6 F indicates that the longshore transport coefficient is
601 rather small in this location (i.e., K is calibrated to almost zero at this location). The relatively
602 small magnitude of longshore transport at this location might be controlled by a few factors: (1)
603 most effects of longshore transport generally appear at the ends of littoral cells (e.g., Anderson et
604 al., 2018) and this particular location is in the middle of Ocean Beach, (2) the shoreline is
605 relatively straight in this location, and hence large gradients in longshore transport are not
606 expected, and (3) the wave angle is predominantly perpendicular to the shoreline at this location
607 on the southern portion of Ocean Beach, although the deep-water to nearshore wave refraction at
608 the northern portion of Ocean Beach plays an important role in driving northward longshore

609 transport, as shown in Vitousek & Barnard (2015). In the context of one-line models, the local
610 wave angle relative to the shoreline, which is extremely important in setting the magnitude of
611 longshore transport, can be controlled by correcting oblique offshore conditions to the local
612 shoreline orientation (Chataigner et al., 2022) or by applying wave conditions that are very close
613 to shore (i.e., in very shallow water). Here, the CDIP wave hindcast (detailed Appendix C.1),
614 which is used to propagate wave conditions to shore (i.e., up to about ~10 m depth) and is co-
615 located with the offshore ends of each transect, is a tremendous resource for the current
616 shoreline-modeling application. Although it has not been tested in the current application,
617 applying linear wave theory (as in Dabees (2000), for example) or the corrections described in
618 Chataigner et al., (2022) might account for the additional wave transformation processes taking
619 place inshore of the wave hindcast locations. However, the strong model performance
620 (discussed below) for this case study suggests that additional wave transformation is generally
621 unnecessary for the current application (given the quality and proximity of the existing CDIP
622 wave hindcast).

623 As mentioned above, the ensemble mean of the long-term residual shoreline change rate v_{lt}
624 shown in Figure 6 G is initialized to approximately one quarter of the local long-term, linear
625 shoreline erosion rate $(v_{lt})_0$ (shown in Figure 5), which is depicted in the blue dashed line on
626 Figure 6 G. We initialized the long-term rate v_{lt} to only one quarter of the long-term rate, $(v_{lt})_0$,
627 because we expect that much of the ‘signal’ contained within the long-term trend, $(v_{lt})_0$, will be
628 parsed into the model’s explicitly resolved components of shoreline change (e.g., longshore
629 transport). In this case, as shown in Figure 6 G, the residual is calibrated to be approximately
630 66% of the historical shoreline trend (up from the initial guess of 25%). However, Figure 6 G

631 demonstrates how the data-assimilation method satisfactorily calibrates v_{lt} over the course of the
632 simulation toward a value that is consistent with the recent shoreline trend at this location. Note
633 that the historical trend represents a time-averaged trend $(v_{lt})_0$ (over the entire span of
634 observations 1995-2020), whereas the residual term v_{lt} represents more of a modern trend, as a
635 consequence of the (sequential) data-assimilation method.

636 Figure 7 depicts observed versus modeled shoreline positions for different model configurations
637 that assimilate the different types of data, e.g., GPS (in panel B) versus satellite-derived
638 shorelines (in panel C) versus both types (Panel D). Figure 7 A shows the wave-forcing time
639 series at transect #7991, whose precise location is shown in the thick green line in Figure 7 E.
640 As in Figure 6, the time series in Figure 7 A, B, C, and D are split into ‘Hindcast (Calibration)’
641 (1995-2015) and a ‘Hindcast (Validation)’ (2015-2020) periods, where data assimilation is
642 turned on and off, respectively. The goal of this test is to better understand the accuracy of the
643 calibrated model when using several years of high precision, but lower temporal frequency data
644 (e.g., monthly GPS observations) versus using several years of lower precision, but higher
645 temporal frequency data (e.g., satellite-derived data). With this comparison, we seek to
646 determine if (for the purposes of model calibration) satellite-derived shorelines can be used in
647 lieu of in-situ observations, which exist only at a handful of well-monitored beaches and are
648 generally unavailable for perhaps over 99% of other beaches worldwide.



649

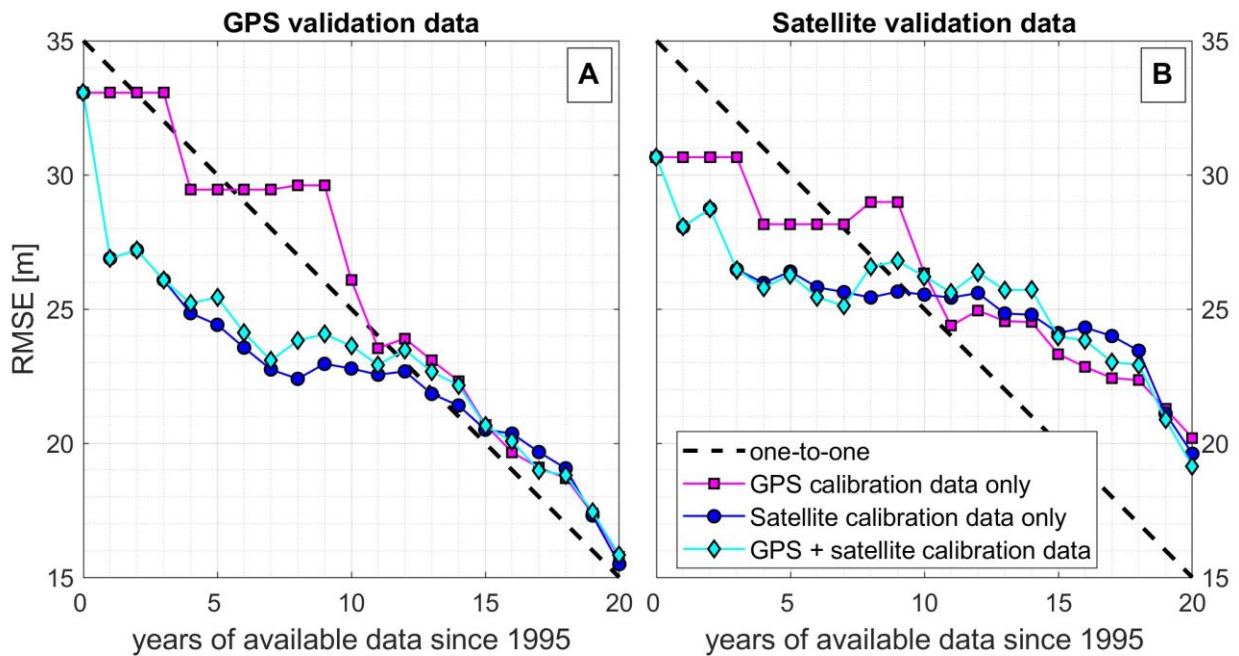
650 Figure 7 – Time series of (A) daily maximum significant wave height [m] for transect #7991 at
 651 Ocean Beach, San Francisco, California, which is indicated in the thick green line in the high-
 652 resolution aerial photo shown in panel E. The figure (panels B, C, and D) also depicts time
 653 series of satellite observed (blue dots + uncertainty bands), in-situ GPS observed (purple
 654 squares), and simulated shoreline position, Y , (ensemble median shown in red line) and 95%
 655 confidence intervals (C.I.) shown in pink bands using different types of assimilated data. Panels
 656 B, C, and D show the model calibrated with only GPS data, only satellite-derived data, and both
 657 types of data, respectively. The time series are split into a ‘Hindcast (Calibration)’ period (1995-
 658 2015) and a ‘Hindcast (Validation)’ period (2015-2020), when data assimilation is turned on and
 659 off, respectively. In panels B, C, and D, each model achieves an RMS error of approximately 16
 660 m compared with the GPS observations during the validation period. (Basemap is from a
 661 current, high-resolution aerial photograph of Ocean Beach available through NOAA Digital
 662 Coast).

663

664 Figure 7 B and C show marked differences in the simulated shoreline position and uncertainty
665 (red line and pink bands, respectively) during the calibration period between assimilating GPS
666 data (panel B) versus satellite-derived data (panel C). In particular, in 2005 (at the onset of the
667 regular field monitoring campaign), the GPS-data-assimilated model (panel B) becomes heavily
668 constrained to fit the (highly accurate) observations. The satellite-data-assimilated model (panel
669 C), on the other hand, is adjusted more slowly/cautiously to the satellite-derived shoreline
670 positions (blue dots) owing to their large (blue ‘whiskers’) uncertainty. However, during the
671 validation period, each of the calibrated models (GPS vs. satellite vs. both, shown in Figure 7 B,
672 C, and D, respectively) demonstrate remarkable similarity, suggesting that calibrations using
673 only satellite observations are on par with calibrations using only GPS data.

674 Figure 8 shows the root-mean-square error (RMSE), $\varepsilon_{\text{RMSE}}$, defined in Eq. (2), which compares
675 the modeled and observed shoreline positions, as a function of calibration-data type and the
676 number of years of data. The RMSE values reported in Figure 8 is the average across all
677 transects within the Ocean Beach survey bounds (transect #7958 to transect #8016), during the
678 ‘Hindcast (Validation)’ period (2015-2020). As more years of observations are assimilated, the
679 RMSE will ideally decrease as the model becomes fully calibrated. Note that in Eq. (2), we
680 apply different RMSE metrics if the observations (Y_{obs}) during the validation period come from
681 GPS-derived shorelines (Figure 8 A) or satellite-derived shorelines (Figure 8 B). Figure 8
682 indicates that assessing model accuracy during the validation period using satellite-derived
683 shorelines (Figure 8 B) has a similar behavior (i.e., RMSE reduces as the amount of calibration
684 data increases) to assessing model accuracy using GPS-derived shorelines (Figure 8 A).
685 However, the assessed model accuracy is generally better when comparing the model to GPS

686 observations (i.e., the curves in Figure 8 A show lower error than those in Figure 8 B), likely
 687 owing to the precision of the GPS observations compared to the satellite-derived shorelines.
 688 Figure 8 establishes some consistency in model performance when either calibrating or
 689 validating it using satellite-derived shorelines versus GPS-derived shoreline observations at a
 690 highly monitored site, as described below.



691
 692 Figure 8 – The spatially averaged root-mean-square error (RMSE) of the model compared to
 693 observations spanning Ocean Beach during the ‘Hindcast (Validation)’ period (2015-2020) vs.
 694 the number of years of available data used during model calibration. Panels A and B correspond
 695 to applying GPS-derived or satellite-derived shoreline for validation, respectively, during
 696 variably sized calibration periods (1995 to 1995+ x , where x is the ‘years of available data’,
 697 plotted on the x -axis). The figure shows different RMSE metrics when calibrating the model
 698 with GPS data only (i.e., purple squares), with satellite-derived shorelines (i.e., dark blue dots) or
 699 both (i.e., light blue diamonds). The blacked dashed line represents a one-to-one line, in which
 700 the RMSE reduces by 1 m with each additional year of data.

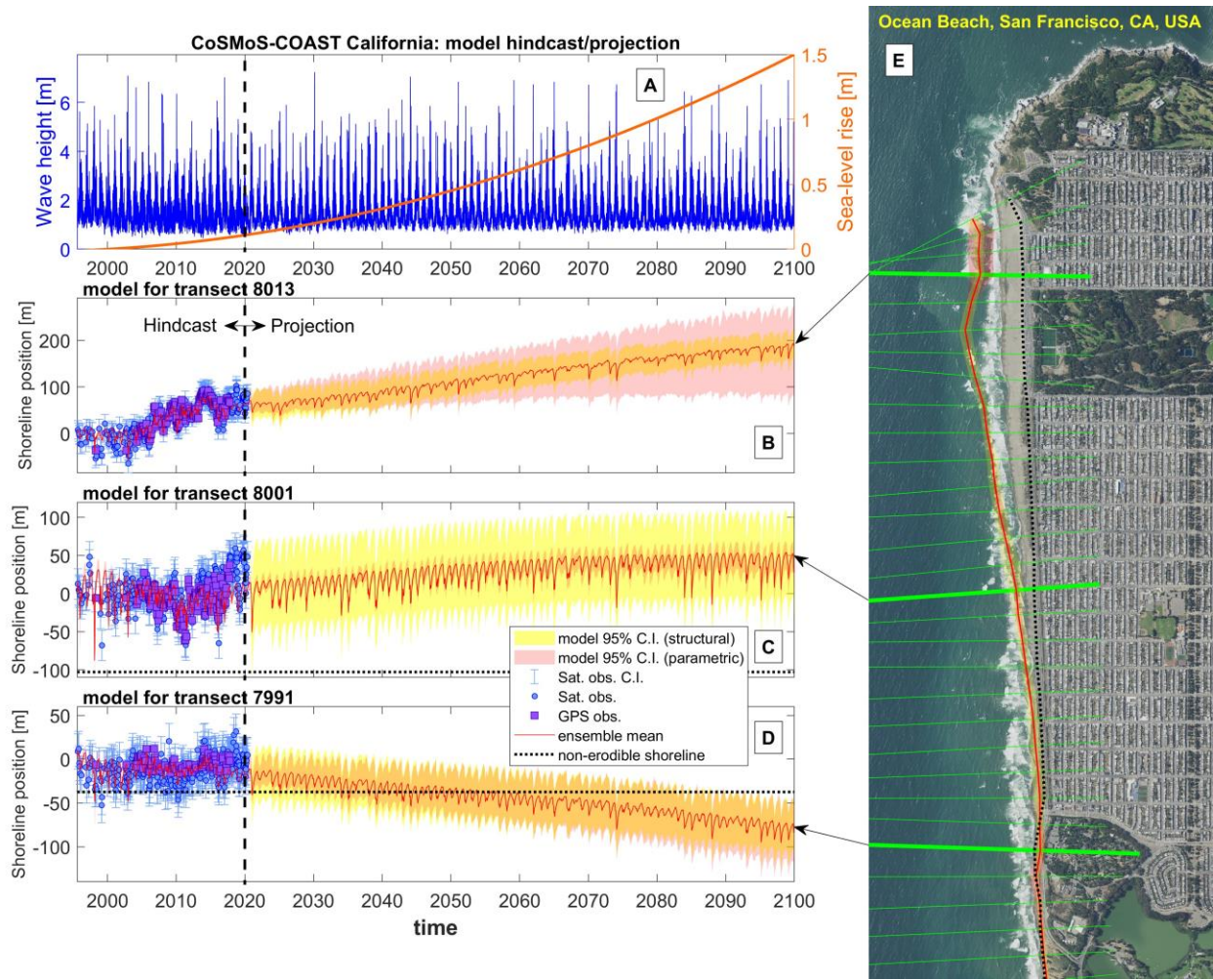
701

702 Figure 8 also illustrates the differences in model RMSE when calibrating the model using
703 different types of calibration data (GPS data only vs. Satellite data only vs. both data sets, shown
704 in purple, dark blue, and light blue, respectively). We also investigate the effects on RMSE as a
705 function of the length of the calibration period, where we artificially turn off the data-
706 assimilation step prior to the ‘Hindcast (Validation)’ (2015-2020) period. For example, 10
707 ‘years of available data since 1995’, shown on the x -axis of Figure 8, indicates a calibrated
708 simulation from the period 1995-2005 (compared the full 20-year calibration period of 1995-
709 2015). In all cases, we apply an unchanging ‘Hindcast (Validation)’ period of 2015-2020. In
710 general, as more data become available, the RMSE (shown in Figure 8) decreases, but not always
711 consistently (often owing to the temporal inconsistency of the observations). For example, the
712 convergence of the GPS-calibration-data-only (i.e., purple) curves in Figure 8 demonstrates two
713 plateaus as more years of data are added, associated with the availability of only two data points
714 prior to the commencement of the extensive field campaign in 2005, which corresponds to
715 isolated (Lidar) surveys in Spring 1998 and Fall 2002 (as shown in Figure 7 B). Conversely,
716 satellite data (blue dots) are more regularly available over the course of the entire simulation, and
717 thus the RMSE shown in Figure 8 B drops rapidly initially, and then at a slightly slower rate
718 thereafter. In each case, the model RMSE decreases slightly more rapidly as modern data
719 become available (i.e., observations collected just prior to the start of the ‘Hindcast (Validation)’
720 in 2012-2014, which correspond to 18-20 ‘years of available data’, respectively). This steeper
721 decrease in RMSE here makes sense (even though the model parameters are mostly converged at
722 this point as shown in Figure 6) since re-initializing the model’s state (particularly the starting
723 shoreline position) to a modern observation is important for improving model accuracy. Using
724 all available data, the model achieves an RMSE of approximately 16 m versus 20 m when

725 validating the model against GPS observations (Figure 8 A) versus when validating the model
 726 against satellite-derived observations (Figure 8 B), respectively, at this location. Note that the
 727 reported model RMSE is only slightly higher than the RMSE of the satellite-derived shorelines
 728 themselves (i.e., 14 m) as demonstrated in Figure 3.

729

730 *3.2.2 Model projection*



731

732 Figure 9 - Time series of (A) daily maximum significant wave height [m] (left axis) and
 733 projected sea-level rise [m] (right axis) for transect #7991 at Ocean Beach, San Francisco,
 734 California, which is indicated in the bottom-most thick green line in the high-resolution aerial

735 photo shown in panel E. Panels B, C, and D depict time series (at different Ocean Beach
736 transects) of the long-term projected ensemble median shoreline position (red line), the 95%
737 confidence intervals (C.I.) of the parametric/epistemic uncertainty (red bands) and the structural
738 uncertainty (yellow bands), the satellite-derived shorelines (blue dots) and uncertainty bands
739 (blue ‘whiskers’), and the in-situ GPS-observed shorelines (purple squares). Panels C, D, and E
740 also show the location of the non-erodible shoreline (black dotted line). The time series are split
741 (visually, by the black vertical dashed line) into ‘Hindcast’ (1995-2020) and ‘Projection’ (2020-
742 2100) periods, where the model is calibrated/validated and run forward, respectively. Note that
743 the dominance of the structural vs. parametric/epistemic uncertainty is transect dependent.
744 (Basemap is from a current, high-resolution aerial photograph of Ocean Beach available through
745 NOAA Digital Coast).

746

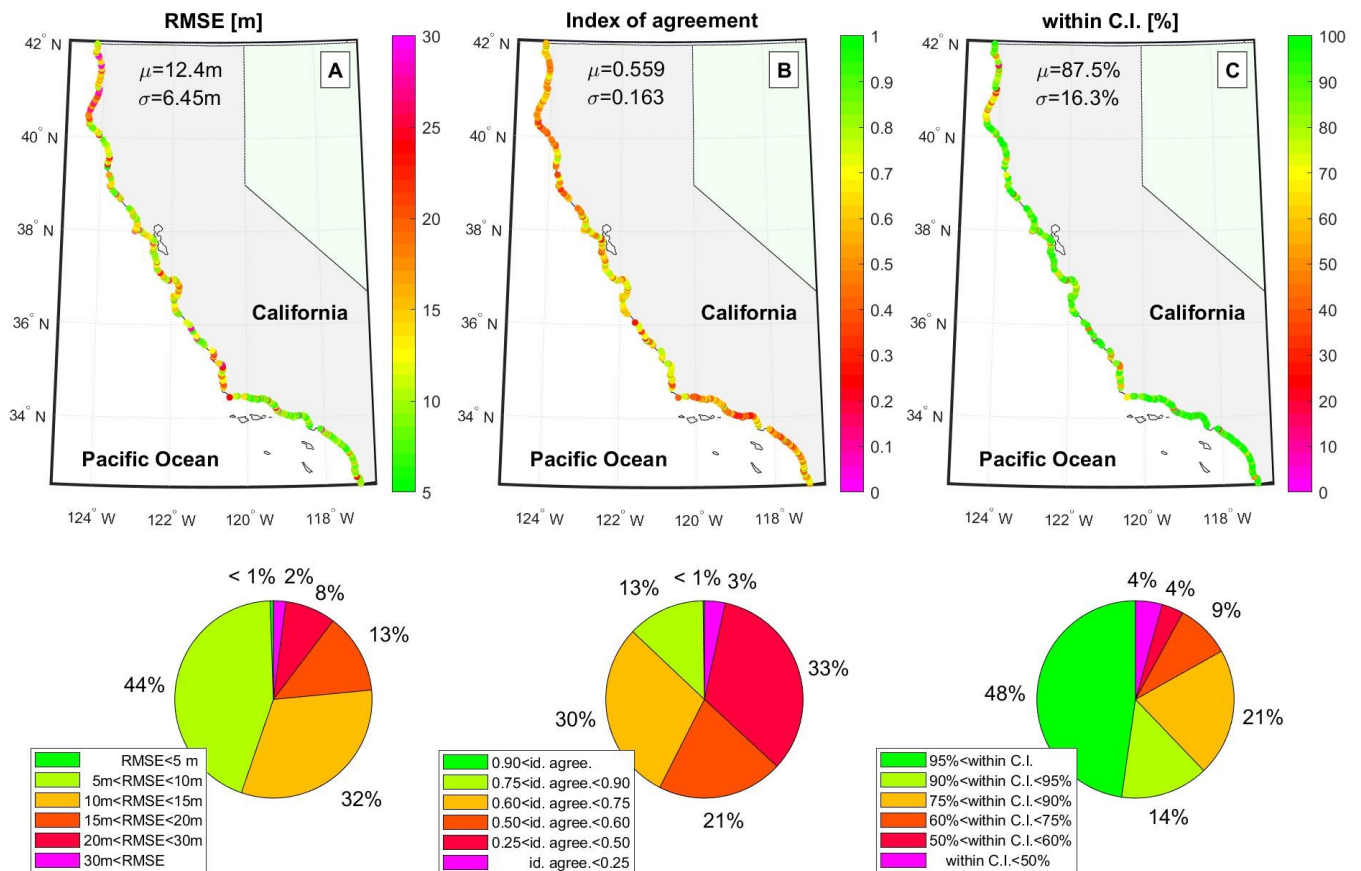
747 Figure 9 depicts long-term projections (up to 2100) of shoreline position and uncertainty
748 (calibrated with all available data) for the Ocean Beach case study under future wave conditions
749 and 1.5 m of sea-level rise. Panels A, B, C, and D depict time series of the long-term projected
750 wave and sea-level conditions, ensemble median shoreline position (red line), and the 95%
751 confidence intervals of the epistemic/parametric uncertainty (shown in red bands and described
752 in Section 2.2.2) and the structural uncertainty (yellow bands, also described in Section 2.2.2).
753 The panels also show the satellite-derived shorelines (blue dots) and 95% confidence bands (blue
754 ‘whiskers’), and the in-situ GPS-observed shorelines (purple squares) used for model calibration
755 during the hindcast period. Figure 9 E shows a high-resolution aerial photograph of Ocean
756 Beach with a map of the modeled shoreline position and uncertainty bands as well as the non-
757 erodible shoreline. Panels C, D, and E also show the location of the non-erodible shoreline
758 (black dotted line). Note that, in panel D, the projected shoreline moves landward of the non-
759 erodible shoreline, indicating loss of sandy beach at this location. Under the ‘hold the line’
760 scenario (described in Appendix C.3, which is not shown here), the modeled shoreline is
761 prevented from eroding past the non-erodible shoreline and acts as if no beach sediment is
762 available for longshore transport when the modeled shoreline is coincident with the non-erodible

763 shoreline. In Figure 9, the time series are split (visually, by the black dashed line) into
764 ‘Hindcast’ (1995-2020) and ‘Projection’ (2020-2100) periods, where the model is calibrated and
765 validated (as in Figure 7) and run forward until 2100, respectively. Note that the model projects
766 long-term accretion, relative stability, and erosion in the northern, central, and southern portions
767 of Ocean Beach, respectively, that are somewhat consistent with modern shoreline trends
768 combined with accelerated sea-level-rise-driven recession, which tends to flatten or reverse
769 historical accretion trends. Much like the variability in projected shoreline trends, the
770 uncertainty bands also demonstrate marked variability across Ocean Beach. At transect #7991
771 (shown in Figure 9 D), the structural and parametric uncertainties are roughly the same size,
772 which represents an ideal case: the model’s internal assessment of its uncertainty (i.e., the
773 parametric uncertainty) is roughly equivalent to an external evaluation of its uncertainty (i.e., the
774 structural uncertainty). However, this is not always the case. Instead, it is often the case that the
775 model is either overconfident (e.g., where parametric uncertainty \ll structural uncertainty, as
776 shown in Figure 9 C) or underconfident (e.g., where parametric uncertainty \gg structural
777 uncertainty, as shown in Figure 9 B). At transect #8013 (shown in Figure 9 B), for example, the
778 model’s large parametric uncertainty is driven by spread of the long-term, residual shoreline
779 trend, v_{lt} , which is not easily constrained via data assimilation, in this case.

780 In summary, the case study of Ocean Beach (presented here) indicates that the calibrated
781 accuracy of the satellite-data-assimilated model is comparable to that of the GPS-data-
782 assimilated model. This comparable accuracy (of the satellite-data-calibrated model and the
783 GPS-data-calibrated model) increases confidence in our ability to calibrate and validate shoreline
784 models over spatiotemporal scales using satellite data. In the following section, we show
785 projections of future shoreline position and uncertainty across California.

786 **3.3 California state-wide projections**

787 Although Lidar and GPS observations of shoreline position are sparse in space and time,
 788 satellite-derived shoreline observations can span the entire California coastline and beyond.
 789 Previous studies, relying on only Lidar and GPS data (e.g., Vitousek et al., 2017), have arguably
 790 had nearly sufficient data for large-scale model calibration over large spatial scales. However,
 791 because model calibration periods must often be long and shoreline-change time series are often
 792 sparse, very limited amounts of Lidar/GPS data (if any) remain for model validation. Prolific
 793 satellite-derived data enable model calibration *and* validation over large spatiotemporal scales.



794

795 Figure 10 – Spatial variability (across the state of California) in model performance metrics
 796 during the ‘Hindcast (Validation)’ period (2015-2020). Panel A depicts the model’s root-mean-

797 square error (RMSE) (Eq. (2)) against satellite-derived shoreline observations; panel B depicts
798 the index of agreement (Eq. (3)) between model and satellite-derived shoreline observations; and
799 finally, panel C illustrates the percentage of the time that the model predictions during the
800 validation period (2015-2020) fall within the 95% confidence bounds of the satellite-derived
801 shoreline observations. The bottom panels show pie charts (for each of the metrics shown
802 above), which indicate various categories of model performance and their associated percentages
803 across the entire California model domain.

804

805 Figure 10 shows the spatial variability across California of three different model performance
806 metrics during the ‘Hindcast (Validation)’ period (2015-2020), including the (1) RMSE (Eq. (2)
807), (2) the index of agreement (Eq. (3)), and (3) the percentage of time that the model falls within
808 the confidence bounds of the satellite shorelines (described below) in panels A, B, and C,
809 respectively. The bottom panels of Figure 10 show pie charts that indicate various categories of
810 model performance and their associated percentages across the entire California model domain.

811 The RMSE (calculated via Eq. (2) and shown in Figure 10 A) applies observations (Y_{obs}) that
812 come from satellite-derived shorelines, which are the only source of consistent observational
813 data at the scale of the current analysis. Figure 10 A indicates that, in this application, the model
814 achieves an RMSE of <15 m for 77% of California and a mean RMSE of 12.4 m, which seems to
815 be roughly consistent with the accuracy of the satellite-derived shoreline observations
816 themselves. The mean RMSE metrics across the different model transect types of “full model”,
817 “cross-shore only”, and “rate only” are 13.3 m, 10.8 m, and 10.3 m, respectively. However, the
818 lower RMSE values for “cross-shore only” and “rate only” are likely due to the more limited
819 shoreline variability of these coastal settings compared to that of the “full model” transects.

820 The index of agreement (Willmott, 1981), given by Eq. (3), is shown in Figure 10 B. We find
821 that $d > 0.5$ across 57% of California with a mean of $\bar{d} = 0.559$. In a recent blind-test

822 shoreline modeling competition (Montaño et al., 2020; comprised of 15 years of calibration data
823 and 3 years of data-blind comparisons), the best performing shoreline models achieved
824 $d \approx 0.5 - 0.7$, and the performance metrics achieved here, over a vastly larger scale, seem
825 comparably good.

826 Lastly, the third and final metric we evaluate here is called ‘within C.I.’ in Figure 10 C, which
827 represents the percentage of the time, during the ‘Hindcast (Validation)’ period (2015-2020), that
828 the model predicted shoreline position falls within the 95% confidence levels of the satellite-
829 derived shoreline observations, which are assumed to be identical to $\pm 2\varepsilon_{\text{sat}}$, where ε_{sat} is the 14
830 m RMSE derived at Ocean Beach (where dense GPS observations are available) and applied
831 uniformly across the California coast. Although the uniform prescription of satellite-error
832 statistics is not ideal, we note that the general 10-15 RMS accuracy of satellite-derived shorelines
833 has been well established through extensive testing at many well monitored sites (e.g., Hagenaars
834 et al., 2017, Luijendijk et al., 2018, Pardo-Pascual et al., 2018, Vos et al., 2019b, Castelle et al.,
835 2021, and Vos et al., 2023). Figure 10 C indicates that the model predictions are within the
836 confidence intervals of the satellite observations approximately 88% of the time (on average)
837 across California.

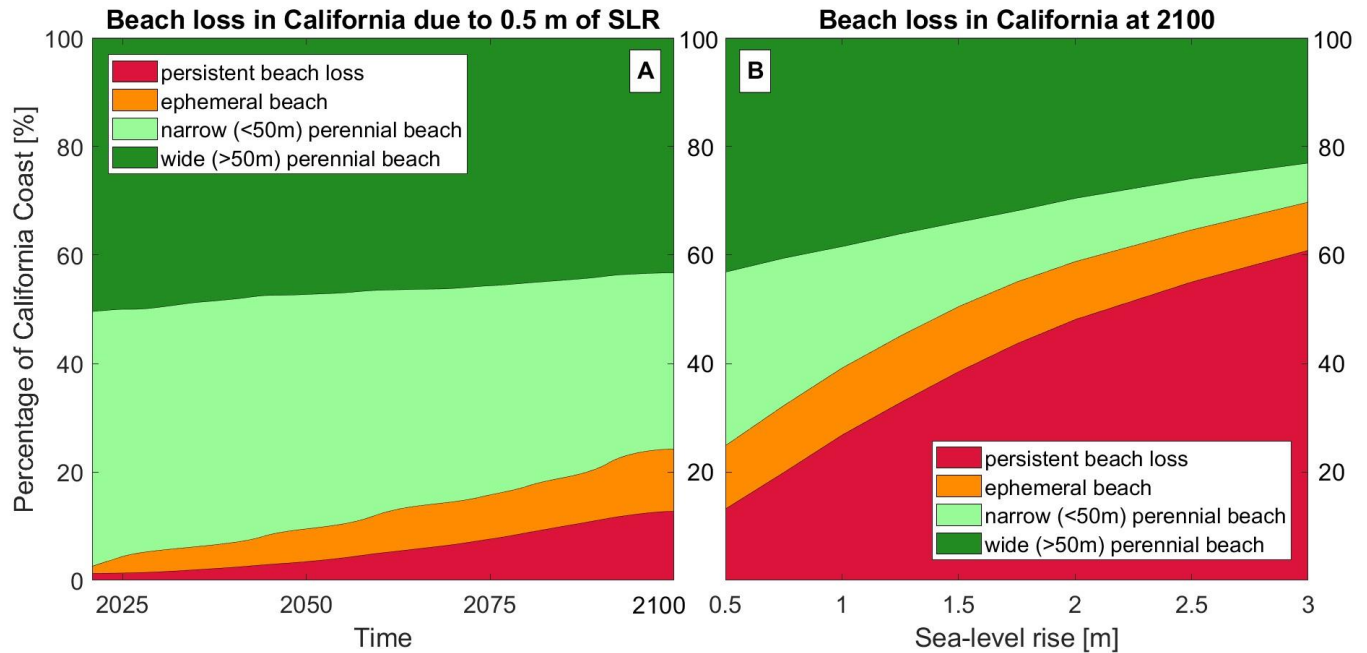
838 Across all skill metrics shown in Figure 10, the model seems to achieve the best performance
839 (i.e., the lowest RMSE and the largest index of agreement) in southern California. However, this
840 is perhaps expected since the equilibrium shoreline-change model, i.e., Yates et al. (2009), which
841 dominates the short-term signal of change, was conceived from local shoreline behavior and
842 observations thereof at Torrey Pines Beach in southern California. However, since its initial
843 development in southern California, the Yates et al. (2009) model has been proven to be skillful

844 across diverse coastal settings (Castelle et al., 2014, Montañó et al., 2020, Hunt et al., 2023).
845 Poorer model performance is generally encountered in northern California, particularly across
846 Humboldt County, which we hypothesize is due to large signals of fluvial sediment input and the
847 presence of large-scale sand waves (~200-1,000 m wavelength) in the region, whose dynamics
848 are not well resolved in the context of the model governing equation. The limited model
849 performance, particularly in regions of high fluvial sediment input, highlights an area for
850 improvement. Future modeling efforts could seek to explicitly account for fluvial sediment
851 inputs by coupling with models of terrestrial processes such as wildfire and pluvial flood events,
852 which can significantly affect coastal sediment budgets (e.g., Warrick et al., 2022), as further
853 discussed below.

854 After validating the model's performance against observed behavior, we apply the model to
855 project future changes in shoreline position until 2100. In particular, we explore scenarios of
856 future beach loss (like the example shown in Figure 9 D) due to accelerated sea-level rise over
857 the 21st century following several previous works (e.g., Vitousek et al., 2017, Le Cozannet et al.,
858 2018, Vousdoukas et al., 2020, and D'Anna et al., 2022). Here (in Figure 11) we analyze the
859 percentage of model transects across California that experience seasonal or persistent beach loss
860 as a function of time and under the 9 sea-level scenarios (0.5, 0.75, 1.0, 1.25, 1.5, 1.75, 2.0, 2.5,
861 3.0 m - given in Figure 20 in Appendix C). In Figure 11, we apply the "no hold the line" and
862 "continued accretion" management scenario (as described in Appendix C), which represents the
863 most conservative scenario. However, as shown in Vitousek et al. (2017), the different
864 management scenarios (replicated here) only result in differences of a few percentage points in
865 the future prevalence of beach loss. Figure 11 categorizes future shorelines into four categories
866 and depicts how those categories change over time (panel A) or with different sea-level rise

867 scenarios (panel B). The four categories, namely “wide perennial beach”, “narrow perennial
868 beach”, “ephemeral beach”, and “persistent beach loss”, indicate increasing levels of
869 concern/vulnerability. The latter two categories, “ephemeral beach”, and “persistent beach loss”,
870 are beach transects whose projected shoreline positions erode past the non-erodible shoreline
871 (i.e., the division between sand and cliffs, dunes, or urban backshores as described in Appendix
872 C.3) either temporarily (e.g., seasonally) or persistently, respectively, by 2100. The first two
873 categories, on the other hand, are mostly self-explanatory and represent either a “wide perennial
874 beach” and “narrow perennial beach” at model transects with greater than or less than 50 m in
875 width¹, respectively, that are not projected to erode close to the non-erodible shoreline by 2100.

¹ 50 m is a somewhat commonly chosen as the threshold that separates wide from narrow beaches, e.g., Vousdoukas et al., 2020.



876

877 Figure 11 – The percentage of beach loss across California as a function of time, and sea-level-
 878 rise scenario of 0.5 m by 2100 (panel A) and as a function of different sea-level rise scenarios by
 879 2100 (panel B; see Figure 20).

880

881 The results in Figure 11 A indicate that the number of transects experiencing “ephemeral” or
 882 “persistent” beach loss accelerates with time (due to accelerated sea-level rise). As shown in
 883 Figure 11 B, the model projects that 13 to 61% of transects across California will experience
 884 permanent beach loss (under sea level scenarios of 0.5 to 3.0 m, respectively). Including
 885 ephemeral/seasonal erosion increases the percentage of beaches lost to between 25 and 70% of
 886 transects across California. Vitousek et al. (2017) projected total beach loss at 31 to 67% of
 887 southern California beaches under sea-level scenarios of 0.93 to 2 m of sea-level rise,
 888 respectively, and the (updated) projections given here across the entire state are largely
 889 consistent with these previous findings. As in Vitousek et al. (2017), the model does not account
 890 for erosion through different substrates (e.g., rocky cliffs and concrete structures) but instead

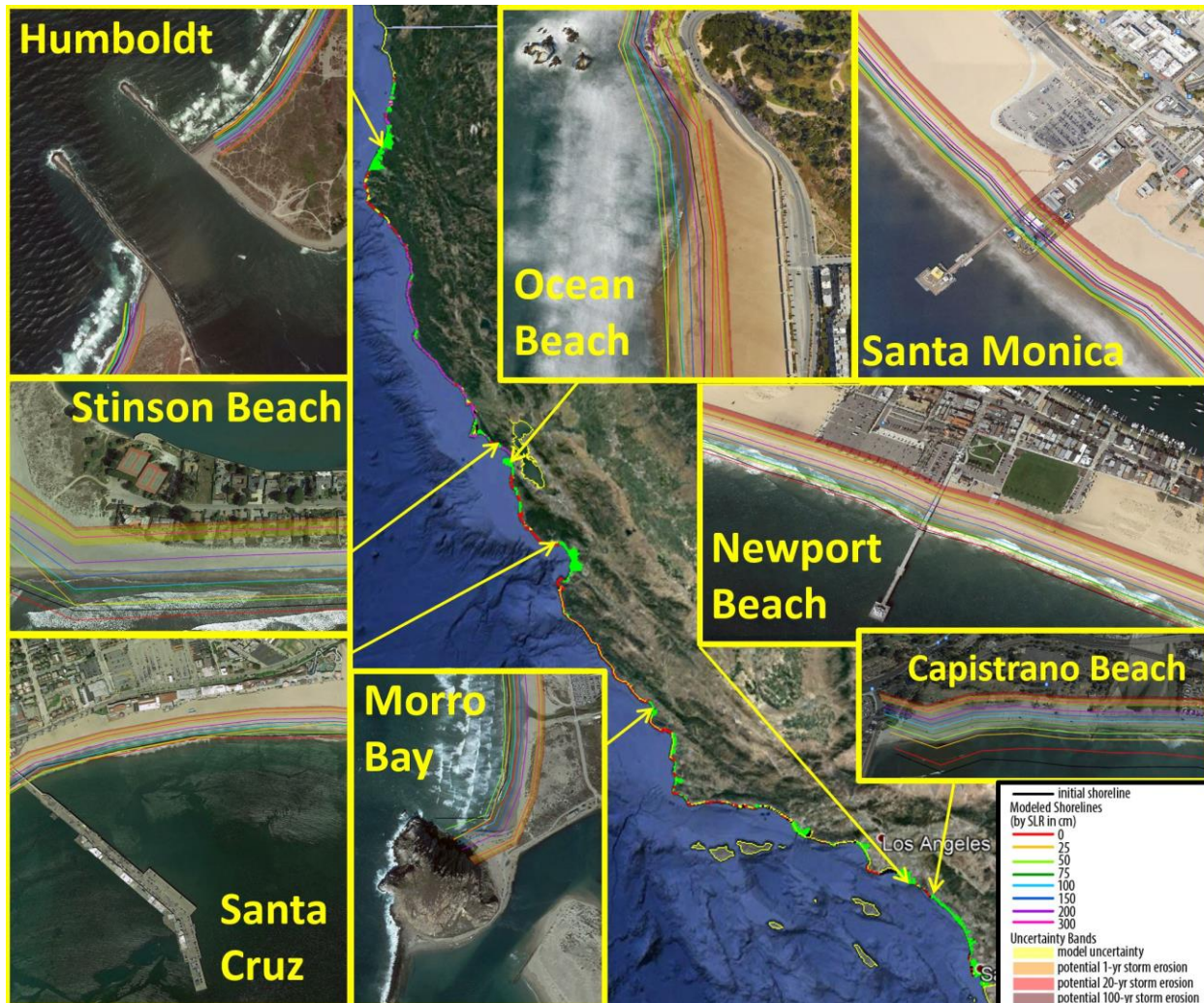
891 treats the entire transect as a sandy substrate during the “no hold the line” scenario. Clearly, this
892 unmodified approach will generally overestimate the landward extent of erosion into cliffs and
893 infrastructure under the “no hold the line” scenario. However, the model predictions of sandy
894 beach erosion extent should generally remain valid up until the beach fully erodes.

895 The model does not explicitly account for sediment supplied to the beach from eroding cliffs,
896 dunes, or rivers, and hence, but instead lumps all of the estimated sediment supply into the long-
897 term residual shoreline trend (e.g., v_{lt}), obtained via data assimilation. Hence, the modeling
898 approach (and the results in Figure 11) may misrepresent the episodic nature of sediment supply
899 in some locations. The current shoreline model could, in theory, be coupled with parameterized
900 models of cliff erosion and/or fluvial input (e.g., Limber et al., 2018, Alessio & Keller 2020,
901 Regard et al., 2022) to mitigate reliance on the long-term residual shoreline trend parameter (e.g.,
902 v_{lt}). However, this endeavor, which has not yet been attempted in the literature, is beyond the
903 scope of the current work and is left as future work.

904

905

906



907

908 Figure 12 - Shoreline modeling predictions for ~1,350 km of coastline in California produced by
 909 the current CoSMoS-COAST model. The predictions represent the shoreline position in 2100
 910 with 1.0 m of sea level rise. The yellow bands represent the projected shoreline position and
 911 (parametric) uncertainty. Note that the transect color across the basemap of California (from
 912 Google Earth) is shown/described in Figure 2.

913

914 The shoreline projections, given here, foretell potentially serious impacts for many of
 915 California's iconic beaches as well as the economic, recreational, and protective benefits they
 916 provide. For example, Figure 12 shows that popular beaches such as Newport Beach, Capistrano
 917 Beach, and the southern portion of Ocean Beach may experience significant erosion by 2100,

918 while others like Santa Monica and the northern portion of Ocean Beach are projected to accrete
919 in spite of the impacts posed by sea-level rise. The California statewide shoreline-change
920 projections produced as part of this study are available via a USGS data release that accompanies
921 this paper (Vitousek et al., 2023 [data set]). Although many of California’s beaches are
922 vulnerable to future erosion (primarily due to sea-level rise and sediment restrictions), scenarios
923 of future beach loss are not unique to California but may become prevalent for many coastal
924 communities throughout the world. However, as shown here, satellite-based shoreline
925 monitoring and data-assimilated modeling are becoming powerful tools for prediction of coastal
926 climate-change impacts and potentially for monitoring the effectiveness of engineering and
927 nature-based solutions.

928 **4. Discussion**

929 Satellite-derived shoreline observations enable predictions across unprecedented spatiotemporal
930 scales. The proliferation of satellite-derived shoreline observations further motivates modeling
931 approaches that can explicitly resolve variability at increasingly shorter time scales (e.g., wave-
932 driven coastal change) yet can be applied over vast, historically data-poor regions. Additionally,
933 increased availability of spatiotemporally dense observations will also greatly benefit long-term
934 historical trend analyses. Castelle et al. (2022) showed that even raw satellite-derived shorelines
935 (which are not corrected for tide or wave setup) can reproduce long-term shoreline trends
936 obtained from traditional methods (e.g., manually digitized shorelines from orthorectified and
937 georeferenced aerial photographs in their study). Avoiding the need to apply tide and wave
938 corrections is a particularly attractive benefit to simplified shoreline-trend analysis efforts.
939 However, tidal-prediction models, which are widely available and accurate, are already

940 incorporated in satellite toolboxes like CoastSat (Vos et al., 2019a), which motivates their use.
941 Nearshore wave hindcasts, needed for wave-setup-corrections to satellite derived shorelines, are
942 generally only available for highly developed and monitored coastlines (e.g., the CDIP hindcast
943 – O’Reilly et al., 2016) or in deeper, offshore waters (e.g., ERA-5 reanalysis – Hersbach et al.,
944 2020). Hence, they might represent a limiting resource for correcting satellite-derived shoreline
945 observations. However, as nearshore wave information is also a critical component of data-
946 assimilated shoreline model predictions, the generation of hindcasted nearshore wave data is
947 complementary to both shoreline modeling and satellite monitoring efforts. As both hindcasted
948 and forecasted nearshore wave information becomes increasingly available, the prospect of
949 operational monitoring and prediction of coastal change becomes possible. Further, satellite-
950 derived workflows are becoming increasingly automated, in contrast to workflows relying on
951 GPS or Lidar data. Thus satellite-derived shoreline observations are becoming an increasingly
952 attractive component of operational shoreline prediction systems (Vitousek et al., 2023). The
953 methods and models described herein might serve as an initial concept for components of a
954 future, operational coastal-change monitoring and prediction system.

955
956 For the very first time, satellite-derived shoreline observations enable validation of model
957 predictions over large spatial scales. Although the model, developed here, is *applied* over a
958 large-scale, we believe the primary innovation of the study is that it is also *validated* over a
959 large-scale (e.g., >1,000 km), which is unlike any other study to date (to our knowledge). We
960 believe that the satellite-based coastal monitoring renaissance may stimulate a renaissance in
961 model prediction. In the past few decades, innovation in coupled coastal hydrodynamic and
962 morphodynamic models has primarily come in the form of resolving more physical processes,
963 notably wave-driven water levels (in incident and infragravity bands; e.g., Sherwood et al.,

964 2021). Innovations to improve the fidelity of coastal physics-based models have had a
965 noticeable impact on the skill of coastal-change simulations during individual storm events, but
966 so far have arguably not had the same effect on long-term simulation of beach processes. On the
967 other hand, simplified, parametrized, and increasingly probabilistic coastal change models,
968 which are most often based on the concept of ‘equilibrium’ (e.g., Wright & Short, 1985, Miller
969 & Dean, 2004, Yates et al., 2009, Davidson et al., 2013, Hunt et al., 2023), have provided the
970 biggest recent innovation in prediction of long-term (e.g., multi-annual to decadal+) coastal
971 change. Although both physics-based and parameterized (reduced-complexity) coastal-change
972 models will benefit from increased availability of observations, we believe the simplified models
973 will receive the greatest returns from data-integration efforts for a number of different reasons:
974 (1) simplified models can be readily calibrated to real-world, site-specific shoreline observations
975 in contrast to more expensive, monolithic models, which also require full bathymetric and
976 topographic surveys for validation, (2) simplified models, mainly due to their significantly
977 shorter runtimes, can be readily applied in a probabilistic sense (e.g., using Monte Carlo
978 methods), and thus will excel in propagating, quantifying, and balancing uncertainty (in both
979 modeling and observational components) in contrast to more expensive and consequently more
980 deterministic models, (3) simplified models can be readily adapted to produce multi-model
981 ensemble predictions, and (4) simplified models are amenable to data-assimilated operational
982 modeling (e.g., based on ensemble Kalman filter methods) as well as scenario-based modeling of
983 future coastal change.

984 The hybridization of models and observations for coastal-change prediction is becoming
985 increasingly viable because of earth-observing satellites. For the first time, satellites can provide
986 coastal *data at the scales of models* and *models at the scales of data* (Vitousek et al., 2023). And

987 eventually, with perhaps another decade of research and development, the field could develop
988 coupled monitoring and modeling systems at national to global scales.

989 In the current application, the developed CoSMoS-COAST model achieves an average RMSE of
990 ~12 m, obtained by comparing model versus satellite-derived observations during a validation
991 period of 2015-2020, averaged over the entire California coastline. We consider this level of
992 accuracy to be quite remarkable (given the scale of shoreline projections in the current
993 application) since the model's performance metrics seem to be on par with the performance
994 achieved in notable, site-specific modeling applications (e.g., Montaña et al., 2020).

995 Furthermore, the accuracy of the model seems to be on the same order of the accuracy of the
996 satellite observations themselves. It is quite likely that the model's RMSE is even lower than the
997 numbers reported here (in Figure 10) due to the limited accuracy of the satellite-derived
998 shorelines used for validation. However, this is only a speculation, as no other (non-satellite)
999 observations exist over equivalent spatiotemporal scales to verify these potential gains in
1000 accuracy. In support of this notion, we turn to the case study at Ocean Beach, a relatively limited
1001 area covering ~5 km of coast, but where monthly data have been collected over 2 decades. In the
1002 case study, presented here, for the 5-year validation period from 2015 to 2020, the model's error
1003 is ~15-20% higher (~3-4 m higher RMSE) when using satellite-derived shoreline observations
1004 for validation than when using highly accurate GPS observations for validation (see Figure 8
1005 panels A vs. B).

1006 Even though the satellite-data-calibrated model is roughly as accurate as the GPS-data-calibrated
1007 model, the model is still not perfect. It is possible that the post-calibration inaccuracies of the
1008 model may have more to do with the limitations of model itself rather than the quality/quantity of

1009 calibration data or lack thereof (especially when two decades of calibration is applied). For
1010 example, non-stationarity in the shoreline model parameters, i.e., the potential for model
1011 parameters to change over time (e.g., Ibaceta et al., 2020), which is not accounted for here, may
1012 lead to drifts between model projections and the real world. Additionally, although the model is
1013 proven to be capable of resolving important signals of coastal change, it does not explicitly
1014 capture a number of important coastal change processes such as the formation and evolution of
1015 large-scale (~200-1,000 m) sand waves, fluvial-discharge events, cliff/bluff failures, headland
1016 bypassing, or other processes that can cause either pulses/shocks of coastal change or slow-
1017 varying, atypical oscillations. However, these issues are certainly not unique to the current
1018 model but persist for nearly all flavors of coastal-change models due to the dogged complexity of
1019 nearshore and subaerial sediment transport. Despite some of the recent improvements adopted in
1020 the latest CoSMoS-COAST model (including the changes in the governing equations and the
1021 adoption of an ensemble-based approach as described in Vitousek et al., 2021 as well as the data-
1022 assimilation advancements detailed in Appendix B), the physics of the current modeling
1023 application is nearly identical to the initial model development (Vitousek et al., 2017). The three
1024 most significant developments of the modeling efforts presented here are: (1) the scale of the
1025 model (i.e., southern California vs. all of California), (2) the integration of satellite-derived
1026 shoreline observations, and (3) the novel data-assimilation method. Further, these developments
1027 are complementary: the scale of data-assimilated modeling efforts is tightly linked with the scale
1028 of available data. We believe it is these three developments (and not really any improvement in
1029 the model physics) that have enabled *better predictions* (e.g., assimilating far more observations
1030 across much larger scales) over previous works.

1031 Although the physics captured in the governing equations of the present model are mostly
1032 adequate to capture the dominant beach processes in California, numerous improvements might
1033 still be integrated into the current model. We suggest that an important component of coastal
1034 change that is not resolved explicitly in the California model is sediment flux from terrestrial
1035 sources, notably rivers. Warrick et al.'s (2022) "Fire plus flood equals beach" (using the same
1036 CoastSat-derived shoreline observations) analyzed beach accretion events at Big Sur, California
1037 following record-setting precipitation events, which followed a wildfire that burned 66% of the
1038 adjacent watershed. Warrick et al.'s (2022) paper was one of the first attempts to estimate the
1039 fluvial portion of a littoral sediment budget using satellite-derived shoreline observations. A
1040 modeling effort to better quantify fluvial sediment input to the coast as a function of
1041 terrestrial/watershed processes, while accounting for its significant temporal variability (East et
1042 al, 2018), is a particularly compelling endeavor and it could possibly be scaled up over the size
1043 of the U.S. West Coast (or even worldwide). Although the current shoreline model is only
1044 forced by nearshore hydrodynamic processes, it could possibly be extended to explicitly account
1045 for fluvial/terrestrial processes via coupling with terrestrial models. For example, future research
1046 might identify signatures of fluvial-discharge events and/or beach nourishments in satellite-
1047 derived shoreline observations (e.g., via machine learning) and subsequently parameterize or
1048 calibrate their occurrence (in both a hindcast and forecast sense with the aid of terrestrial-process
1049 models and GCM projections). The alternative approach (used here), to model fluvial,
1050 anthropogenic, or unresolved processes implicitly via a residual, linear shoreline-change rate (see
1051 term 3 in Eq. (1)), which can mask chronic erosion of nourished beaches (Armstrong & Lazarus,
1052 2019), was previously taken out of necessity, given the sparsity of coastal observations.
1053 However, with the increasing availability of satellite-derived shoreline observations, the

1054 motivation to explicitly resolve both the nearshore hydrodynamic and terrestrial components of
1055 coastal change substantially increases. In California, in particular, the sources and magnitudes of
1056 sediment input remain critical gaps in littoral sediment budgets and in the long-term survival of
1057 beaches (particularly those in natural settings) in response to sea-level rise (Warrick et al., 2023).
1058 In highly urban settings/environments (which are generally without significant fluvial-sediment
1059 input), we believe that the survival of beaches in urban environments will increasingly rely on
1060 beach nourishment and/or sand retention (Griggs et al., 2020). Yet, better satellite observations
1061 (with increasingly higher image quality and quantity) and better satellite-data-assimilated
1062 modeling predictions (such as those developed in the current paper) will be critical to design and
1063 monitor the effectiveness of engineering interventions and nature-based solutions.

1064

1065 **5. Conclusions**

1066 We have developed and applied a large-scale, long-term shoreline change modeling system
1067 across 1,350 km of coast in California, home to a variety of different coastal geomorphic
1068 settings. For the first time, the model assimilates data from satellite-derived shoreline
1069 observations (derived from the CoastSat toolbox), providing a thousand-fold increase in
1070 assimilation data over traditional Lidar and GPS shoreline observations across the California
1071 coastline. In a case study at Ocean Beach, California, where extensive in-situ field monitoring
1072 efforts have taken place, we demonstrate that the assimilation of satellite-derived shorelines
1073 provides comparable predictive accuracy to a model with decades of monthly in-situ surveys.
1074 This case study provides confidence that satellite-derived shorelines, available anywhere in the
1075 world, can be used to calibrate and validate models of coastal change. Across California, during

1076 a validation period of 2015-2020, the model achieves an average RMSE of ~12 m and an index
1077 of agreement of 0.54 when compared to satellite observations. The assessed accuracy of the
1078 California model is comparable to many state-of-the-art blind tests of multi-model shoreline
1079 prediction capabilities at well-monitored individual sites elsewhere in the world (e.g., Montaña
1080 et al., 2020). The model predictions, although subjected to considerable uncertainty, indicate
1081 that significant impacts to the shoreline may occur due to accelerated sea-level rise, with 25 to
1082 70% beaches across California lost by 2100 under the 0.5 to 3.0 m SLR projections. It is likely
1083 that many beaches in California will require substantial management efforts (e.g., beach
1084 nourishments, sand retention, armoring, dune restorations as well as other engineering and
1085 nature-based solutions) in order to maintain existing beach widths and the many services they
1086 provide.

1087

1088 **Acknowledgements**

1089 We would like to thank Tiffany Anderson and Mohsen Taherkhani for conducting internal
1090 reviews of this manuscript. We thank the three anonymous journal reviewers and the editors for
1091 their comments and suggestions, which lead to a significant improvement of this manuscript.

1092 This work was funded by the USGS Coastal and Marine Hazards and Resources Program. Any
1093 use of trade, firm, or product names is for descriptive purposes only and does not imply
1094 endorsement by the U.S. Government.

1095

1096 **Data availability statement**

1097 The satellite-derived shorelines used in this study are available online at
1098 <http://coastsat.wrl.unsw.edu.au/> . Data and models, produced as part of this study, are available,
1099 for purposes of peer review only, at: [https://drive.google.com/drive/folders/1ipaiW9ap9TMJvF-
1100 qUQBRTh3CBM6gtO1x?usp=share link](https://drive.google.com/drive/folders/1ipaiW9ap9TMJvF-qUQBRTh3CBM6gtO1x?usp=share_link) . Upon provisional acceptance of the manuscript and
1101 subject to USGS data and software review policies, the data and software produced as part of this
1102 study will be made publicly available on USGS ScienceBase and code.usgs.gov, respectively,
1103 with a Digital Object Identifier.

1104 **Appendix A: Numerical model**

1105 This appendix details the numerical solution of the governing equation of the CoSMoS-COAST
1106 model, Eq. (1), which closely follows that of Vitousek et al., 2017.

1107 *A.1.1 Longshore transport*

1108 The first term on the right-hand side of Eq. (1) is the alongshore convergence of the longshore
1109 sediment transport, where Q is the longshore sediment-transport rate, X represents the
1110 alongshore coordinate, and d_c is the depth of closure. A generalized expression for the
1111 longshore-transport rate is

$$1112 \quad Q = Q_0 \sin(2\alpha), \quad (8)$$

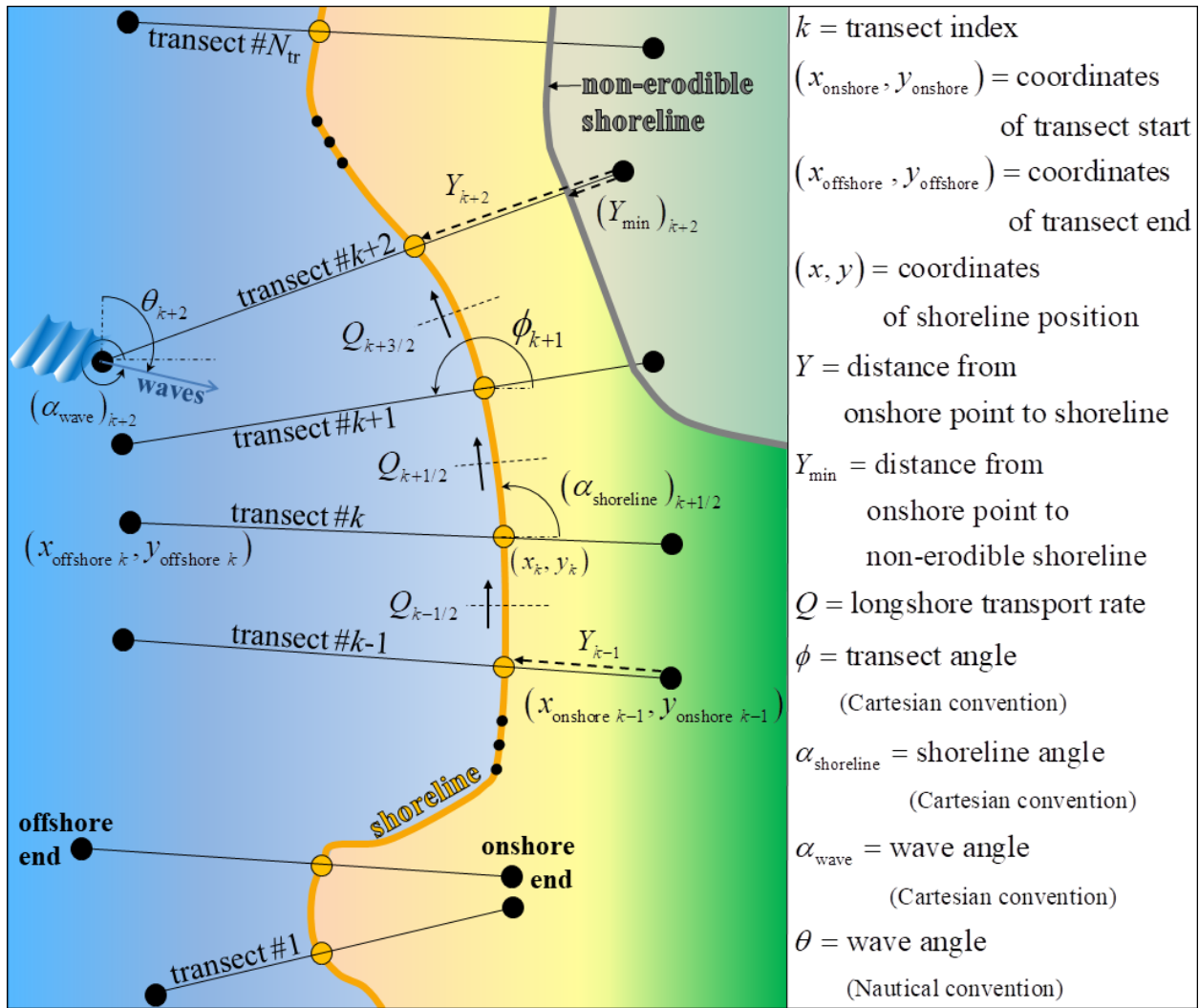
1113 where Q_0 represents the magnitude of the longshore sediment-transport rate derived empirically
1114 and expressed as a function of wave and sediment properties (e.g., CERC (1984); Kamphuis
1115 (1991)). In the current implementation, we approximate the magnitude of the longshore-
1116 transport rate as $Q_0 \approx KH_s^2$, where H_s is the significant wave height at the offshore endpoint of

1117 each model transect (which is calculated via nearshore wave models as described below in
 1118 appendix C.1), and K is an aggregated parameter that is determined via data assimilation. The
 1119 argument of Eq. (8), $\alpha = \alpha_{\text{wave}} - \alpha_{\text{shoreline}}$, represents the relative angle (in Cartesian convention)
 1120 between the incident waves (with incoming direction θ in Nautical convention, which
 1121 corresponds to a Cartesian angle $\alpha_{\text{wave}} = 270 - \theta$ as shown in Figure 13) and the shoreline angle,
 1122 $\alpha_{\text{shoreline}}$ (Larson et al., 1997). The shoreline angle is given by

$$1123 \quad \alpha_{\text{shoreline}} = \text{atan}\left(\frac{\Delta y}{\Delta x}\right), \quad (9)$$

1124 where x and y represent the real world (e.g., Universal Transverse Mercator - UTM) Cartesian
 1125 coordinates of the shoreline, and $\Delta x_{k+1/2} = x_{k+1} - x_k$ and $\Delta y_{k+1/2} = y_{k+1} - y_k$ represent the
 1126 differences (in easting and northing, respectively) between the shoreline-position coordinates on
 1127 adjacent transects (as shown in Figure 13). Note that some variables exist on directly on the
 1128 transects themselves (with integer values of subscripts k) and some variables exist at the
 1129 midpoints between transects (with values $k + 1/2$). When necessary, we apply one-dimensional
 1130 (1-D) linear interpolation to translate variables from transects to midpoints and vice versa.

1131 The model does not consider high-angle wave instability and the growth of shoreline features
 1132 such as spits, sand waves, and capes (e.g., Ashton et al., 2001; Falques, 2003; van den Berg et
 1133 al., 2012; Kaergaard and Fredsoe, 2013; Roelvink et al., 2020), which can lead to multivalued
 1134 solutions to the shoreline position, Y , at a specific time. Further details on the longshore-
 1135 transport component of the model are given in Vitousek et al. (2017).



1136

1137 Figure 13 - Schematic showing the setup and some important variables of the transect-based
 1138 CoSMoS-COAST model.

1139 *A.1.2 Shoreline recession due to sea-level rise*

1140 The second term on the right-hand side of Eq. (1) models shoreline recession due to sea-level
 1141 rise (S). The $\tan \beta$ is the so-called the “transgression slope” (e.g., Wolinsky & Murray 2009),
 1142 which represents the ratio of sea-level rise and the shoreline recession. The transgression slope
 1143 is typically approximated using beach profile geometry. When $\tan \beta$ is chosen as the foreshore
 1144 beach slope or the inland beach slope (e.g., Wolinsky & Murray 2009), this term represents the

1145 shoreline recession in response to passive flooding. When the transgression slope is chosen as
1146 the average slope of the active beach profile extending to the depth of closure (commonly
1147 denoted as $\tan \alpha$), term [2] on the right-hand side of Eq. (1) represents the “classic Bruun rule”
1148 (Bruun 1962). The Bruun rule is widely used (Bruun, 1988) and modified (Davidson-Arnott,
1149 2005; Wolinsky & Murray, 2009; Rosati et al., 2013; Young et al., 2014; Anderson et al., 2015,
1150 Davidson-Arnott & Bauer 2021), yet widely criticized (Cooper & Pilkey, 2004; Ranasinghe et
1151 al., 2012; Cooper et al., 2020) as an oversimplification of shoreline evolution. In the current
1152 implementation, the additional terms on the right-hand side of Eq. (1), e.g., terms [1] and [3]-[5],
1153 are intended to capture the processes missing from stand-alone applications of the Bruun rule.
1154 Despite criticism of the Bruun rule, there model remains widely used because there is "no
1155 simple, viable alternative" to it (Rosati, 2013). However, recent work (D’Anna et al., 2021b)
1156 proposed that the recession mechanism of the Bruun rule can be separated into two components:
1157 (1) shoreline recession due to passive flooding and (2) shoreline recession due to wave
1158 reshaping, which represents the cumulative effect of increased wave-driven erosion efficiency on
1159 a beach profile with an elevated sea-level state, which is captured via “equilibrium” shoreline-
1160 change theory in the fourth term on the RHS of Eq. (1). Recent validation studies of the Bruun
1161 rule have been carried out in both laboratory (Atkinson et al., 2018) and field (Troy et al., 2021,
1162 Davidson-Arnott & Bauer 2021) settings, which motivate the inclusion on the Bruunian
1163 shoreline recession model (along with an accompanying calibration coefficient c obtained from
1164 data assimilation) in the current application. Perhaps the biggest uncertainty in the application of
1165 the Bruun rule, is: what is the most appropriate “transgression slope” to apply? As in Vitousek et
1166 al. 2017, we apply a transgression slope ($\tan \beta$) that represents the foreshore beach slope
1167 between approximately -2.0 and +2.0 m around mean sea level, which translates to roughly a

1168 1/32 slope, when spatially averaged. However, in different coastal environments this
1169 transgression slope may differ significantly from that used here.

1170 *A.1.3 Long-term shoreline trend*

1171 The third term on the right-hand side of Eq. (1) is the long-term, residual shoreline trend that
1172 represents persistent processes such as sources and sinks of sediment from fluvial inputs (Inman
1173 and Jenkins, 1999; Willis and Griggs, 2003; Warrick and Mertes, 2009), nourishments (Flick,
1174 1993), cliff-failure (Young et al., 2011; Limber and Murray, 2011), aeolian transport (Bauer et
1175 al., 2009), sand mining (Thornton et al., 2006), and transport from offshore (Schwab et al.,
1176 2013). Regions dominated by these unresolved, residual effects will have locally high values of
1177 v_{lt} .

1178 In Eq. (1), if the long-term trend, v_{lt} , is a constant, then the shoreline migration is linear in time.
1179 Shoreline-change analyses using historical aerial photos often use linear regressions to fit
1180 observed shoreline data and determine long-term annual erosion rates (e.g., USGS National
1181 Assessment of Shoreline Change - Hapke et al., 2006). The data-assimilation method assumes
1182 that v_{lt} is constant, with initial value that is proportional to the linear regression rate $(v_{lt})_0$.
1183 However, when each data-assimilation step takes place, the magnitude of v_{lt} changes and thus
1184 the unresolved, long-term shoreline change is time-dependent. During the model forecast period
1185 when there are no observations available to assimilate, v_{lt} remains constant (as set by the
1186 sequential data-assimilation method at the end of the calibration period), and therefore the
1187 unresolved, long-term shoreline change associated with this term is linear in time. Consequently,

1188 the long-term component is subject to error when chronic, unresolved processes result in a
1189 nonlinear, future shoreline response (Armstrong & Lazarus 2019).

1190 *A.1.4 Wave-driven cross-shore equilibrium transport*

1191 The fourth term on the right-hand side of Eq. (1) represents the Yates et al. (2009) equilibrium
1192 shoreline model that simulates episodic beach erosion and recovery during periods of high and
1193 low waves, respectively. Vitousek et al. (2021) reformulated the Yates et al. (2009) model to
1194 introduce parameters with intuitive meanings and dimensions (e.g., length or time), while
1195 retaining exactly the same model dynamics. In Eq. (1), the equilibrium shoreline position is
1196 given by

$$1197 \quad Y_{\text{eq}} = -\Delta Y \frac{H_s^2 - (H_s)_b^2}{(H_s)_b^2} \quad (10)$$

1198 and the equilibrium time scale is given by

$$1199 \quad \tau = \Delta T \left(\frac{H_s}{(H_s)_b} \right)^{-1} \quad (11)$$

1200 where $(H_s)_b$, ΔY , and ΔT , are free parameters, detailed in Vitousek et al. (2021) and briefly
1201 summarized below. In Eqs. (10)-(11), $(H_s)_b$ is the background wave-height parameter, which
1202 bears a close resemblance to the average of the wave-height time series. The term ΔY is the
1203 characteristic cross-shore erosion/accretion length-scale parameter, which is typically
1204 $O(1-10 \text{ m})$, and ΔT is the background equilibrium time-scale parameter, whose magnitude is
1205 typically on the order of several weeks. Note that, in Eq. (11), the instantaneous time scale τ

1206 effectively becomes longer or shorter than the background time scale ΔT during small or large
1207 wave conditions, respectively, relative to the background wave height.

1208 *A.2 Spatial discretization (model transects)*

1209 In the proposed model, the coastline is discretized into a series of nodes that exist on shore-
1210 normal transects that are arbitrarily spaced in the alongshore direction. For each transect, the
1211 shoreline position at a given time step is measured by the distance, Y , from the onshore end of
1212 the transect. The model computes the evolution of Y for each transect. Accordingly, the
1213 shoreline evolves as if “on rails” represented by each transect. A schematic of the model domain
1214 is shown in Figure 13. Although there are long-term coastal evolution models that are grid
1215 based (e.g., the Coastal Evolution Model (CEM) – Ashton & Murray, 2006, LX-shore – Robinet
1216 et al., 2018) and vector-based (Hurst et al., 2015) or free-form (Roelvink et al., 2020), the current
1217 model is chosen to be transect based to cover long, irregular coastlines and facilitate the
1218 composition of the 1-D, process-based models (described above) with data assimilation.

1219 For the current application, the domain is discretized into 11,539 transects spaced approximately
1220 100-200 m apart (Figure 2). Each transect is assigned a designation of either “full model”,
1221 “cross-shore only”, “rate only”, “cliff only” or “no prediction” based on geologic characteristics
1222 (which occur for 31.9%, 18.2%, 30.6%, 12%, and 7.3% of the California coastline, respectively).
1223 Based on the transect designation, the shoreline model retains or neglects certain physical
1224 processes and the corresponding terms in the governing equation, Eq. (1). As the name implies,
1225 transects designated as “full model” evolve the shoreline using the full governing equation, Eq.
1226 (1). “Full model” transects are selected for long, sandy beaches, and all model components are
1227 included. Small (< 1 km), sandy barrier islands or pocket beaches are designated as “cross-shore

1228 only” by setting $K = 0$. The model also designates cobble beaches and heterogeneous
1229 sandy/rocky beaches as “rate only” transects by neglecting longshore and cross-shore transport
1230 due to waves, i.e., setting $K = 0$ and $\Delta Y = 0$. These transects evolve the shoreline using a linear
1231 change rate (obtained via data assimilation) plus a recession rate due to excess passive flooding
1232 above the current rate of SLR (Anderson et al., 2015). Finally, “cliff only” and “no prediction”
1233 transects represent sea-cliffs (without fronting beaches) or armored shorelines, respectively,
1234 where no model calculations are performed.

1235

1236 *A.3 Temporal discretization*

1237 The model uses explicit Euler time stepping (e.g., Moin, 2010) for the cross-shore transport
1238 terms due to waves, sea-level, and long-term effects. However, these terms generally do not
1239 exhibit much susceptibility to numerical instability. The longshore-transport term, on the other
1240 hand, is susceptible to numerical instability based on the Courant number condition $\Delta t < \frac{\Delta X^2 d_c}{4Q_0}$
1241 (Ashton & Murray, 2006; Vitousek & Barnard, 2015). Hence, the transect spacing, ΔX , is
1242 generally the most important consideration in selecting the preferred model time step. In
1243 general, explicit Euler time stepping suffices for transects spaced approximately 50 m or greater.
1244 To avoid potential numerical instability the model optionally uses a split-explicit method (e.g.,
1245 Debreu et al., 2012) to subcycle the longshore-transport term with an integral time-refinement
1246 factor.

1247

1248

1249 *A.4 Split model equations*

1250 To facilitate model construction and data assimilation, Eq. (1) is split into individual components
 1251 of shoreline change Y_{lst} , Y_{bru} , Y_{vlt} , and, Y_{st} , which represent shoreline change components on
 1252 each individual transect driven by the individual terms [1]-[4] in Eq. (1). The total shoreline
 1253 position is given as

$$1254 \quad Y = Y_{lst} + Y_{bru} + Y_{vlt} + Y_{st} + Y_0 \quad , \quad (12)$$

1255 where Y_0 is the initial (observed) shoreline position.

1256 This splitting procedure ensures that the equilibrium shoreline position, Y_{eq} , given in Eq. (1), is
 1257 correctly associated with the variability of the short-term shoreline position, Y_{st} , following Long
 1258 & Plant (2012). Further, this splitting procedure allows easy identification of the dominant
 1259 components involved in the overall coastal change.

1260 The split model equations become

$$1261 \quad \frac{(Y_{lst})_k^{n+1} - (Y_{lst})_k^n}{\Delta t} = -\frac{1}{(d_c)_k} \frac{Q_{k+1/2}^{n+\theta} - Q_{k-1/2}^{n+\theta}}{\Delta X_k} \quad (13)$$

$$1262 \quad \frac{(Y_{bru})_k^{n+1} - (Y_{bru})_k^n}{\Delta t} = -\frac{c_k}{\tan \beta_k} \left(\frac{\partial S}{\partial t} \right)_k^n \quad (14)$$

$$1263 \quad \frac{(Y_{vlt})_k^{n+1} - (Y_{vlt})_k^n}{\Delta t} = (v_{lt})_k \quad (15)$$

$$1264 \quad \frac{(Y_{st})_k^{n+1} - (Y_{st})_k^n}{\Delta t} = \frac{1}{\tau_k} \left((Y_{eq})_k^n - (Y_{st})_k^n \right) \quad (16)$$

1265 where superscripts n represent the time-step index, Δt is the time step, k represents the transect
1266 index, and ΔX_k the distance between adjacent transects. In Eq. (13), the superscript variable
1267 $\theta = 0$ or $\theta = 1$ represents the use of explicit versus implicit time stepping, respectively,
1268 following the method of Vitousek & Barnard (2015). All of the model parameters and variables
1269 in Eqs. (13) - (16) are defined at each transect (with index k) except the longshore transport rate,
1270 Q , which is located between adjacent transects (with indices $k \pm 1/2$). Although the splitting
1271 procedure in Eqs. (13) - (16) seems to result in an “uncoupled” model, the model still accounts
1272 for feedbacks between the individual shoreline components since the longshore-transport term
1273 (see Eqs. (8) - (9)) is calculated using the shoreline angle associated with the full shoreline
1274 position Y .

1275 **Appendix B: Data assimilation**

1276 The original data-assimilation method used in CoSMoS-COAST (Vitousek et al. 2017) operated
1277 independently for each transect. Here, we develop novel data-assimilation method (described in
1278 this appendix) that uses all observations within a littoral cell (at a given time step) to assimilate
1279 the model parameter values for all transects within that littoral cell. To accomplish this, the data
1280 assimilation method uses a global state vector (containing all state variables/parameters) rather
1281 than a local (transect specific) state vector as described in B.1, combined with a novel
1282 localization method described in B.3.

1283 *B.1 Model state vector*

1284 Data assimilation automatically adjusts the model state (i.e., the model solution and parameters)
1285 during runtime to best fit any available observed data at the concurrent time step. In the current

1286 application, the state vector representing the model solution and parameters (at a given transect
 1287 k) that is adjusted via data assimilation is given by

$$1288 \quad \vec{x}_k = \left[(Y_{\text{lst}})_k \quad (Y_{\text{st}})_k \quad \Delta T_k \quad \Delta Y_k \quad (\hat{H}_s)_k \quad c_k \quad (v_{\text{lt}})_k \quad K_k \quad \sigma_k \right]^T. \quad (17)$$

1289 Eq. (17) includes the important model parameters and two model solution variables (Y_{lst} and Y_{st})
 1290 for a total of $N_{\text{var}} = 9$ variables, in this case. Note that, in the context of the current model, the
 1291 assimilation of any parameter in the state vector in Eq. (17) can be effectively turned off by
 1292 removing the variance of that parameter across the ensemble (i.e., by applying a constant value
 1293 of the model parameter), which implies perfect confidence in the value of that parameter.

1294 Although the total shoreline position (given in Eq. (12)) is composed of other components, i.e.,
 1295 Y_{bru} , and Y_{vlt} , we do not seek to assimilate (i.e., adjust) the values of these components, since,
 1296 according to Eqs. (14) and (15), they represent quasi-deterministic model components (i.e., they
 1297 are generally monotonic and their governing equations allow them to be uniquely determined
 1298 from independent variables such as the amount of sea-level rise or time, respectively) rather than
 1299 dynamic components (like Y_{lst} and Y_{st}). Note, however, that the model parameters like c and v_{lt}
 1300 that influence the evolution of Eqs. (14) and (15) are assimilated.

1301 Eq. (17) presents a slight simplification of the state vector used in CoSMoS-COAST. As
 1302 discussed in Vitousek et al. (2017), the native data-assimilation method does not guarantee that
 1303 the model parameters retain their requisite sign (for example, $\Delta T, \Delta Y, \hat{H}_s, c, K, \sigma$ are positive
 1304 quantities). Hence, we modify the state vector slightly (following Vitousek et al., 2017) to
 1305 assimilate the natural logarithm of positive-valued model parameters, which are then converted
 1306 (via the exponential function) back to its original form following the data assimilation step.

1307 Following Eqs. (13) - (17), the evolution equation of the state vector is given by

$$\begin{aligned}
 1308 \quad \frac{\partial \vec{x}_k}{\partial t} = \frac{\vec{x}_k^{n+1} - \vec{x}_k^n}{\Delta t} = & \begin{bmatrix} \frac{1}{(d_c)_k} \frac{Q_{k+1/2}^{n+\theta} - Q_{k-1/2}^{n+\theta}}{\Delta X_k} \\ \frac{1}{\Delta T_k} \left((Y_{\text{eq}})_k^n - (Y_{\text{st}})_k^n \right) \\ 0 \\ 0 \\ 0 \\ 0 \\ 0 \\ 0 \end{bmatrix} = \mathbf{f}_k^n \quad (18)
 \end{aligned}$$

1309 Eq. (18) has zero right-hand-side terms, $\frac{\partial \vec{x}}{\partial t} = 0$, for the evolution of the seven model parameters,

1310 $\Delta T, \Delta Y, \hat{H}_s, c, v_{\text{lt}}, K, \sigma$, that represent spatially-variable, yet temporally-constant coefficients,

1311 which are updated at each data-assimilation step. Note that in Eq. (18), terms with superscript n

1312 (i.e., $Q^{n+\theta}$ and $(Y_{\text{eq}})^n$), which are functions of the wave forcing conditions, $(H_s)^n$) are variable in

1313 time. On the other hand, terms without superscript n are assumed to be constant with time in the

1314 absence of data assimilation (e.g., $\Delta T, \Delta Y, \hat{H}_s, c, v_{\text{lt}}, K, \sigma$ as well as the unassimilated parameters

1315 d_c and $\tan \beta$), although in reality the processes that these parameters seek to represent can

1316 exhibit some variability in time, inevitably resulting in model error. For the original CoSMoS-

1317 COAST model (Vitousek et al., 2017), the data-assimilation method in Eq. (18) took place

1318 independently for each transect k , meaning that the model for a given transect only accounted for

1319 shoreline observations falling on that individual transect at that instance in time. The current

1320 method, however, assimilates an augmented state vector \vec{x}_a for all transects that is given by

1321
$$\bar{\mathbf{x}}_a = \left[\bar{\mathbf{x}}_1^T \quad \bar{\mathbf{x}}_2^T \quad \cdots \quad \bar{\mathbf{x}}_k^T \quad \bar{\mathbf{x}}_{k+1}^T \quad \cdots \quad \bar{\mathbf{x}}_{N_{\text{tr}}}^T \right]^T \quad (19)$$

1322 The (global) augmented state vector $\bar{\mathbf{x}}_a$ (which is of size $(N_{\text{tr}} \times N_{\text{var}}) \times 1$) in Eq. (19) contains the
 1323 $N_{\text{var}} \times 1$ state vectors (with $N_{\text{var}} = 9$) given in Eq. (17) for all (N_{tr}) model transects.

1324 It is often desirable to assimilate site-specific behavior from site-specific observations.

1325 However, assimilating each transect independently does not leverage the spatial coherence that
 1326 exists between adjacent observations. As discussed below in Section B.3, we seek a
 1327 compromise between data quantity and data locality by implementing a so-called ‘localization’
 1328 method to prioritize assimilation of coincident and neighboring observations.

1329 *B.2 Ensemble Kalman filter data-assimilation method*

1330 Here, we utilize an ensemble Kalman filter (EnKF) data-assimilation method following Evensen
 1331 (1994). The EnKF data-assimilation method evolves an ensemble of the (augmented) model
 1332 state vector,

1333
$$\mathbf{x} = \left[(\bar{\mathbf{x}}_a)_1 \quad (\bar{\mathbf{x}}_a)_2 \quad \cdots \quad (\bar{\mathbf{x}}_a)_{N_{\text{ens}}} \right], \quad (20)$$

1334 where each (augmented) state vector $\bar{\mathbf{x}}_a$ of the N_{ens} member ensemble contains the combination
 1335 of the model solution and parameters (as in Eqs. (17) and (19)). Note that throughout this
 1336 appendix, boldfaced quantities (e.g., \mathbf{x}) indicate an ensemble quantity or matrix (with
 1337 dimensions provided where possible). The assembly of the model state vector ensemble (i.e.,
 1338 Eqs. (17), (19), and (20)) is illustrated in Figure 14.

1339 The EnKF method sequentially adjusts the model state during the simulation to best fit any
 1340 available shoreline observations at the concurrent time step, via an optimal interpolation that
 1341 accounts for the uncertainty of both model and observations. The procedure of the data-
 1342 assimilation method is given by:

1343 1. Run the forward model with added noise:

$$1344 \quad \mathbf{x}^* = \mathbf{F}(\mathbf{x}^n) + \boldsymbol{\varepsilon}_{\text{mod}} \quad (21)$$

1345 where \mathbf{x}^* is the $((N_{\text{tr}} \times N_{\text{var}}) \times N_{\text{ens}})$ ensemble of the forecasted state vector (e.g., Eq. (17)
 1346), \mathbf{x}^n is the ensemble of the model state vectors at time step n , \mathbf{F} is the operation of the
 1347 (forward) model for a single time step (i.e., $\mathbf{F}(\mathbf{x}^n) = \mathbf{x}^n + \Delta t \mathbf{f}^n$ where \mathbf{f}^n is given in Eq.
 1348 (18)) and $\boldsymbol{\varepsilon}_{\text{mod}} \sim \mathbf{N}(0, \sigma^2)$ is a sample of random, normally-distributed noise with zero
 1349 mean and user-prescribed standard deviation σ , which can vary for each parameter and
 1350 is added to the model forecast. Vitousek et al. (2021) demonstrated that the additive
 1351 noise parameter σ plays an extremely important role in the specification of the epistemic
 1352 uncertainty (i.e., the user-specified accuracy limits of the model).

1353 In the absence of data to assimilate, $\mathbf{x}^{n+1} = \mathbf{x}^*$, and the inverse model (i.e., the data-
 1354 assimilation method computed via steps 2-5 below) is not computed, and the model state
 1355 vector at time step $n+1$ is simply that which is predicted by the (forward) model. In the
 1356 current application, when data are no longer available to assimilate (i.e., during a forecast
 1357 period), then $\boldsymbol{\varepsilon}_{\text{mod}}$ is set to zero, and the ensemble is propagated forward without additive
 1358 noise, $\mathbf{x}^{n+1} = \mathbf{F}(\mathbf{x}^n)$, as is nominally the case for unassimilated models.

1359 2. Calculate the background model (\mathbf{X}^*) and (model-predicted) observation (\mathbf{Y}^*) anomalies
 1360 about the ensemble average, according to

$$1361 \quad \mathbf{X}^* = \mathbf{x}^* - \bar{\mathbf{x}}^* \quad (22)$$

$$1362 \quad \mathbf{Y}^* = \mathbf{y}^* - \bar{\mathbf{y}}^* \quad (23)$$

1363 where $\bar{\mathbf{x}}^*$ and $\bar{\mathbf{y}}^*$ are the ensemble averages of \mathbf{x}^* and \mathbf{y}^* , respectively. In Eqs. (22) and
 1364 (23), \mathbf{X}^* and \mathbf{Y}^* are ensembles of size $(N_{\text{tr}} \times N_{\text{var}}) \times N_{\text{ens}}$ and $N_{\text{obs}} \times N_{\text{ens}}$, respectively,
 1365 where N_{obs} is the number of transects with observations to assimilate at a given time
 1366 step. It is important to note that here the variable \mathbf{y}^* does not represent actual
 1367 observations. Instead, $\mathbf{y}^* = H(\mathbf{x}^*)$ represents the ensemble of model-predicted variables
 1368 that coincide with the observed variables (e.g., at their given spatial locations), where H
 1369 is an interpolation operator that ensures that the model output and observations are co-
 1370 located.

1371 3. Calculate the combined error covariance matrix

$$1372 \quad \mathbf{P} = \underbrace{\rho \left(\frac{1}{N_{\text{ens}} - 1} \mathbf{Y}^* (\mathbf{Y}^*)^T \right)}_{\text{(inflated) model covariance matrix}} + \underbrace{\mathbf{R}}_{\text{observation covariance matrix}} = \rho \text{cov}(\mathbf{y}^*) + \mathbf{R} \quad (24)$$

1373 which is a $N_{\text{obs}} \times N_{\text{obs}}$ matrix that represents the sum of the covariance of the model error
 1374 and the observation error, where ρ is a so-called ‘covariance inflation factor’ (typically
 1375 chosen to be $\rho = 1.1$, as is the case here) and \mathbf{R} is the $N_{\text{obs}} \times N_{\text{obs}}$ covariance matrix of

1376 observation error. Here we apply the approximate error covariance matrix ($\mathbf{R} = \tilde{\mathbf{R}}$)
1377 derived below in Eq. (34) of Section B.5. The weighting between model and
1378 observations (which accounts for the uncertainty of each source of error) is calculated
1379 below in Eq. (25). Compared with the *extended* Kalman filter (EKF) approach (used in
1380 Long & Plant, 2012, and Vitousek et al., 2017), Eq. (24) replaces the analytical derivation
1381 and advancement of the error covariance matrix \mathbf{P} , which is calculated from the Jacobian
1382 matrix (i.e., the matrix of partial derivatives) of the forward model \mathbf{F} . Hence, the EnKF
1383 method requires very little computational overhead and no analytical work to derive the
1384 Jacobian matrix, in contrast to the EKF method. However, the EnKF method does
1385 require running an ensemble of models as opposed to running a single model realization
1386 using the EKF. Running a model ensemble certainly increases the computational
1387 requirements, but it also enables modeling of a range of model parameters and forcing
1388 conditions, and thus a better accounting of uncertainty, which is often a desirable feature.

1389 4. Calculate the so-called ‘Kalman gain’, \mathbf{K} , according to

$$1390 \quad \mathbf{K} = \frac{1}{N_{\text{ens}} - 1} \mathbf{X}^* (\mathbf{Y}^*)^T \mathbf{P}^{-1} \quad (25)$$

1391 Here, \mathbf{K} is a $(N_{\text{tr}} \times N_{\text{var}}) \times N_{\text{obs}}$ matrix (recalling that N_{tr} is the total number of model
1392 transects to assimilate, N_{var} is the number of variables in the assimilated state vector [Eq.
1393 (17)], and N_{obs} is the number of transects with observations to assimilate at the current
1394 time step). Eq. (25) requires the calculation of a matrix inverse (or the solution of a
1395 linear system of equations). However, this matrix inversion is typically quite affordable

1396 since \mathbf{P} is an $N_{\text{obs}} \times N_{\text{obs}}$ matrix, where N_{obs} is typically $O(10-100)$ and is generally
 1397 much smaller than N_{tr} (which is often $O(1,000-10,000)$).

1398 5. Apply a localization routine (described in the following section) to prioritize the
 1399 influence of nearby observations on the data-assimilation procedure. This step adjusts
 1400 the (global) Kalman gain, \mathbf{K} , according to $\mathbf{K}_{\text{loc}} = \mathbf{L}_{\mathbf{K}} \circ \mathbf{K}$, where $\mathbf{L}_{\mathbf{K}}$ is the localization
 1401 matrix given in Eq. (28), which is motivated below in Section B.3.

1402 6. Update the ensemble state vector according to

$$1403 \quad \mathbf{x}^{n+1} = \mathbf{x}^* + \mathbf{K}_{\text{loc}} \left(\underbrace{\left[\mathbf{y}_{\text{obs}}^{n+1} + \boldsymbol{\varepsilon}_{\text{obs}} \right]}_{\text{perturbed observations}} - \underbrace{\mathbf{y}^*}_{\text{model prediction for the observed locations/variables}} \right) \quad (26)$$

1404 where \mathbf{x}^{n+1} is the final (analysis) state vector. Eq. (26) represents an ‘optimal’
 1405 interpolation between model and observations. Eq. (26) demonstrates that the
 1406 $(N_{\text{tr}} \times N_{\text{var}}) \times N_{\text{obs}}$ (localized) Kalman gain matrix \mathbf{K}_{loc} effectively scales/translates the
 1407 mismatch between the observation ensemble (of size $N_{\text{obs}} \times N_{\text{ens}}$) and the model into
 1408 adjustments made to the state vector \mathbf{x} (with size $(N_{\text{tr}} \times N_{\text{var}}) \times N_{\text{ens}}$). Note that the
 1409 bracketed term in Eq. (26) represents perturbation of the observed state vector, $\mathbf{y}_{\text{obs}}^{n+1}$, with
 1410 the representative error/noise sampled from a multivariate normal distribution,

$$1411 \quad \boldsymbol{\varepsilon}_{\text{obs}} = \mathbf{N}(\mathbf{0}, \mathbf{R}).$$

1412 The model and data-assimilation methodology are summarized in Figure 14.

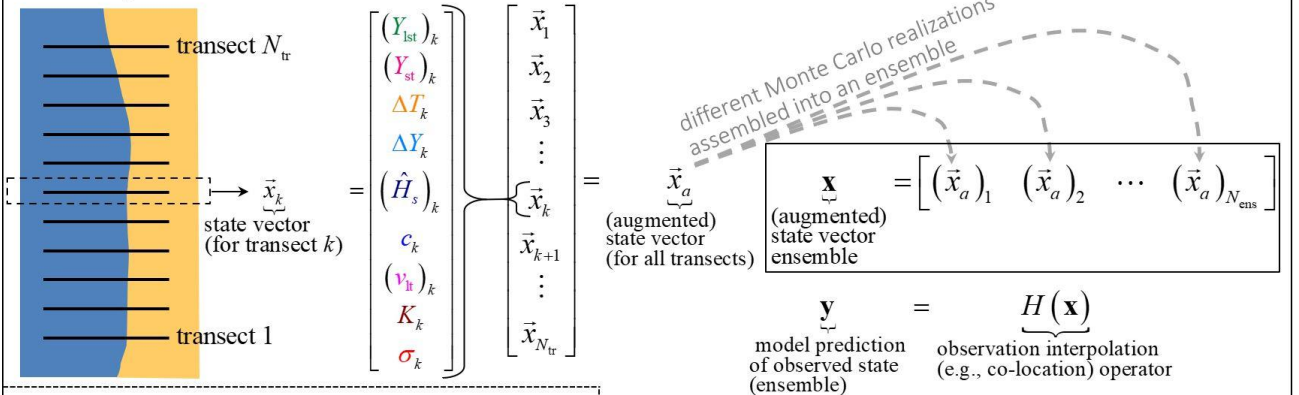
CoSMoS-COAST: Coastal One-line Assimilated Simulation Tool

Governing equations (i.e., forward model):

recession due to sea-level rise: long-term rate: longshore transport: cross-shore (equilibrium) transport:

$$\left((Y_{bru})_k^{n+1} = (Y_{bru})_k^n - \Delta t \frac{c_k}{\tan \beta_k} \left(\frac{\partial S}{\partial t} \right)_k^n \right); \quad \left((Y_{vit})_k^{n+1} = (Y_{vit})_k^n + \Delta t (v_{tr})_k \right); \quad \left((Y_{lst})_k^{n+1} = (Y_{lst})_k^n - \frac{\Delta t}{(d_c)_k} \frac{Q_{k+1/2}^{n+\theta} - Q_{k-1/2}^{n+\theta}}{\Delta X_k} \right); \quad \left((Y_{st})_k^{n+1} = (Y_{st})_k^n + \frac{\Delta t}{\tau_k} \left((Y_{eq})_k^n - (Y_{st})_k^n \right) \right)$$

Assembly of model state vector ensemble:



Data assimilation (ensemble Kalman filter):

1. $\underline{\mathbf{x}}^* = \mathbf{F}(\underline{\mathbf{x}}^n) + \boldsymbol{\varepsilon}_{\text{mod}}$ where \mathbf{F} represents the forward model (above) & $\boldsymbol{\varepsilon}_{\text{mod}} \sim \mathcal{N}(0, \boldsymbol{\sigma}^2)$ is the additive noise
forecasted (prior) state vector ensemble
2. a : $\underline{\mathbf{x}}^* = \mathbf{x}^* - \bar{\mathbf{x}}^*$ where $\bar{\mathbf{x}}^*$ is the ensemble mean
state vector anomaly
- b : $\underline{\mathbf{y}}^* = \mathbf{y}^* - \bar{\mathbf{y}}^*$ where $\bar{\mathbf{y}}^*$ is the ensemble mean
(model-predicted) observed state anomaly
3. $\mathbf{P} = \rho \left(\frac{1}{N_{\text{ens}} - 1} \mathbf{Y}^* (\mathbf{Y}^*)^T \right) + \mathbf{R}$ where $\rho = 1.1$ is the covariance inflation factor
covariance matrix (inflated) model covariance matrix observation covariance matrix
4. $\mathbf{K} = \frac{1}{N_{\text{ens}} - 1} \mathbf{X}^* (\mathbf{Y}^*)^T \mathbf{P}^{-1}$
Kalman Gain
5. $\mathbf{K}_{\text{loc}} = \mathbf{L}_{\mathbf{K}} \circ \mathbf{K}$ where $\mathbf{L}_{\mathbf{K}}$ is the localization matrix
(localized) Kalman Gain
6. $\underline{\mathbf{x}}^{n+1} = \underline{\mathbf{x}}^* + \mathbf{K}_{\text{loc}} \left(\left[\mathbf{y}_{\text{obs}}^{n+1} + \boldsymbol{\varepsilon}_{\text{obs}} \right] - \mathbf{y}^* \right)$ where $\mathbf{y}_{\text{obs}}^{n+1}$ are the observations and ...
assimilated (analysis) state vector ensemble perturbed observations model prediction of observed variables $\boldsymbol{\varepsilon}_{\text{obs}} = \mathcal{N}(0, \mathbf{R})$ is the observation error

1413

1414 Figure 14 – Summary of the model and data-assimilation methodology, including the assembly
 1415 of the state vector ensemble.

1416

1417

1418

1419 *B.3 Localization*

1420 Localization is a commonly used method in data assimilation to prioritize the influence of nearby
1421 observations on the assimilated model state (Hamill et al., 2001). For many beaches located
1422 along the same broad stretch of coastline, we expect that observations of coastal change will be
1423 correlated due to the spatial coherence of the underlying geologic and oceanographic process
1424 (e.g., wave conditions) that force change. Localization methods prioritize data locality during
1425 the data assimilation step by suppressing the potential for spurious correlations in the model state
1426 across large spatial distances. In the context of the current work, localization is attractive because
1427 it effectively calibrates local shoreline behavior from local shoreline observations (while still
1428 utilizing as much data as possible). Further, because (satellite-derived) observations are
1429 generally available (i.e., with comparable temporal resolution) for all transects, we have the
1430 option to be “picky” when it comes to prioritizing site-specific data. For modeling applications
1431 in regions where beach profile data are available with far greater spacing than model transects
1432 (e.g., Ruggiero et al., 2016), the localization method can also provide a means of assimilating
1433 parameters for model transects in neighborhood of profile observations, without the need for the
1434 (model and observational) transects to overlap, for example.

1435 The two most common localization techniques include *domain localization* and *covariance*
1436 *localization*. The former applies the data assimilation separately for individual, independent
1437 subdomains of the model. The latter artificially tapers the model error covariance matrix, i.e.,
1438 the first term of Eq. (24), to suppress the influence of covariates that occur over large distances.
1439 In the present work, we apply a novel ‘hybrid’ localization method, which applies concepts from
1440 both domain and covariance localization methods. The developed localization method replaces

1441 the (global) Kalman-gain matrix, \mathbf{K} , of size $(N_{\text{tr}} \times N_{\text{var}}) \times N_{\text{obs}}$ given in Eq. (26), with a localized
 1442 Kalman-gain matrix \mathbf{K}_{loc} (which is of the same size) and is given by:

$$1443 \quad \mathbf{K}_{\text{loc}} = \mathbf{L}_{\mathbf{K}} \circ \mathbf{K} \quad (27)$$

1444 In Eq. (27), the \circ operator represents the Hadamard (or element-wise) product between the
 1445 original Kalman gain \mathbf{K} (given in Eq. (26)) and $\mathbf{L}_{\mathbf{K}}$, which represents the localization matrix
 1446 that given by

$$1447 \quad \mathbf{L}_{\mathbf{K}} = \mathbf{L}_{\text{obs}} \otimes \mathbf{e} \quad (28)$$

1448 In Eq. (28), $\mathbf{e} = [1 \ 1 \ \dots \ 1]^T$ is a $N_{\text{var}} \times 1$ vector of all ones, and \otimes is an operator representing
 1449 the Kronecker product, which effectively “tiles” (i.e., replicates) the localization matrix \mathbf{L}_{obs} for
 1450 each of the N_{var} elements of the assimilated state vector in Eq. (17). In Eq. (28), \mathbf{L}_{obs} is a
 1451 $N_{\text{tr}} \times N_{\text{obs}}$ localization matrix that is derived by selecting only specific columns (corresponding
 1452 to transects with co-located observations) from a global localization matrix \mathbf{L} of size $N_{\text{tr}} \times N_{\text{tr}}$,
 1453 which is given by

$$1454 \quad \mathbf{L} = 2^{-\frac{\mathbf{D}}{L_d}} \circ \mathbf{I}_{\text{cell}} \quad (29)$$

1455 The first term in the product on the right-hand side of Eq. (29) applies the concept of covariance
 1456 localization via a exponentially decaying function $f(x) = 2^{-x/L_d}$ (with decay distance
 1457 corresponding to the alongshore distance between two transects, i.e., $L_d = 2$, in the present
 1458 application) and \mathbf{D} is the $N_{\text{tr}} \times N_{\text{tr}}$ transect separation distance matrix

1459 $(\mathbf{D})_{i,j} = |i - j|,$ (30)

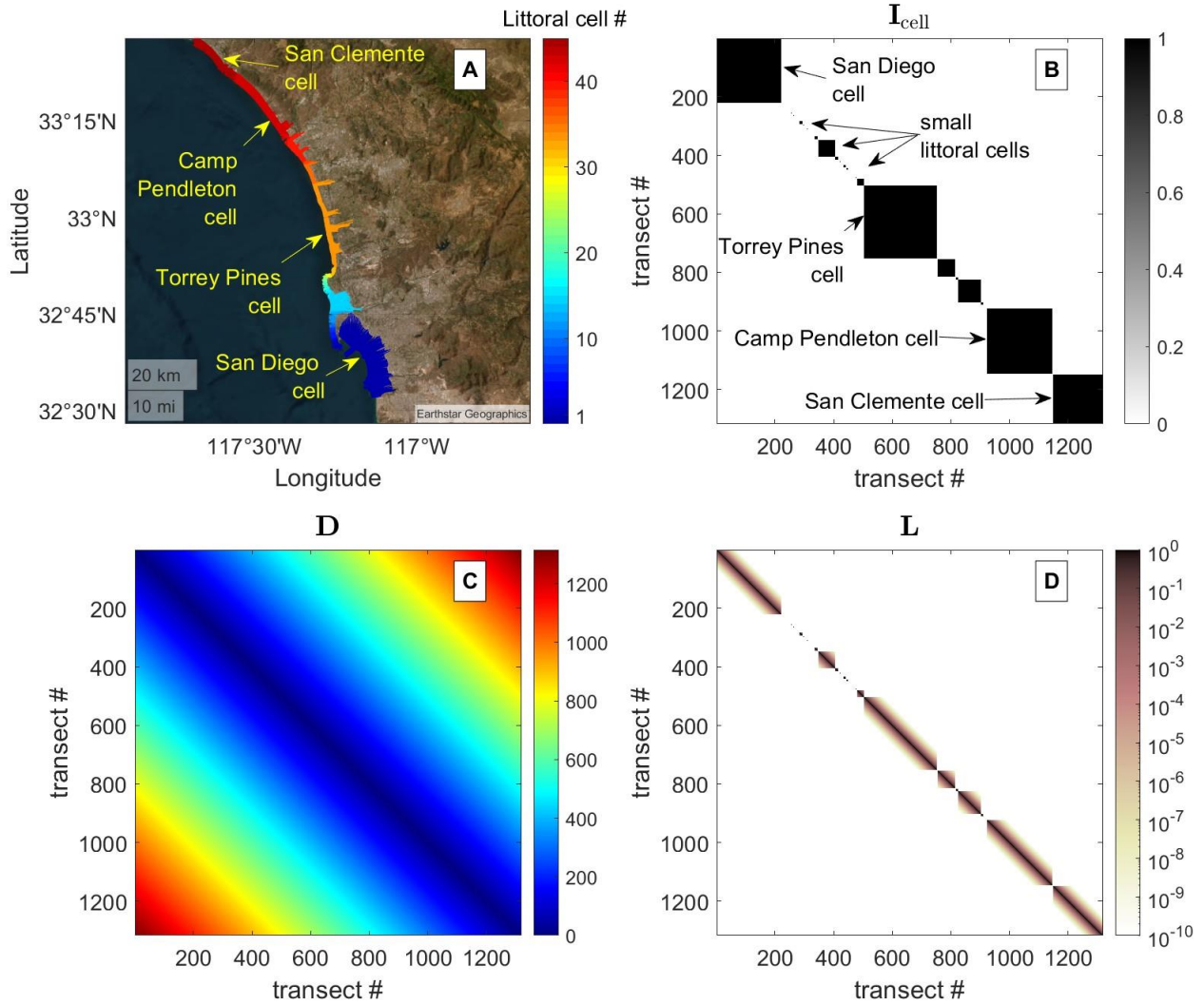
1460 where i and j represent transect indices. Although the same decay function, $f(x)$, and the
 1461 same decay distance $L_d = 2$ are applied uniformly for all model parameters and all transects, the
 1462 hybrid method presented here, permits the possibility that different model parameters or transects
 1463 might be localized with different treatment (e.g., observations might be specified exert a stronger
 1464 or weaker spatial influence on certain model parameters). However, the optimization of this
 1465 approach is beyond the scope of this paper.

1466 Eq. (29) also applies the concept of domain localization by introducing (user-specified or
 1467 automatically defined) “littoral cells”, which represent individual subdomains that isolate (i.e.,
 1468 localize) assimilated changes to the model state to come only from observations falling within
 1469 the same littoral cell. In Eq. (29), the (global) littoral cell adjacency matrix \mathbf{I}_{cell} of size $N_{\text{tr}} \times N_{\text{tr}}$
 1470 is used to implement domain localization, which represents the explicit introduction of (user-
 1471 controlled) spatial structure into the data-assimilation method (which is otherwise controlled
 1472 only by the (global) covariance of the model state, see Eq. (25)). In the current application, \mathbf{I}_{cell}
 1473 represents a Boolean matrix that is given by

1474 $(\mathbf{I}_{\text{cell}})_{i,j} = \begin{cases} 1 & \text{if transect } i \text{ is within the same littoral cell as transect } j \\ 0 & \text{otherwise} \end{cases}$

1475 \mathbf{I}_{cell} effectively sets many of the elements of the localized Kalman gain \mathbf{K}_{loc} equal to zero for all
 1476 model transects located in a different user-defined ‘littoral cell’ than the cell with observations
 1477 currently being assimilated. In the context of the California application model, the ‘littoral cells’
 1478 (for the purposes of data assimilation) are defined as sets of transects that share a continuous

1479 stretch of sandy beach with the same model-type designation (e.g., “full model”, “cross-shore
1480 only”, etc. as described in Appendix A) that are not interrupted by inlets, headlands, harbors, or
1481 large jetties, for example. In short, the method, detailed above, ensures that model parameter
1482 values are assimilated using observations that fall within the same littoral cell. Note that when
1483 the elements of the Kalman gain \mathbf{K}_{loc} are zero, then the assimilation step does not alter the
1484 model state vector in Eq. (26), i.e., $\mathbf{x}^{n+1} = \mathbf{x}^*$, for all transect that are considered “non-local” to a
1485 given shoreline observation. Figure 15 depicts idealized versions of the \mathbf{I}_{cell} matrix, the distance
1486 matrix \mathbf{D} , and the full localization matrix \mathbf{L} for a subset of the model transects used here (i.e.,
1487 transects #1-1200) for illustration purposes.



1488

1489 Figure 15 – The components (i.e., a map of the identified littoral cells in panel A, the littoral cell
 1490 adjacency matrix I_{cell} shown in panel B, and the transect-separation distance matrix D shown in
 1491 panel C) of the localization matrix (L) shown in panel D for the present application, which is
 1492 shown only for a limited subset of the transects used here (i.e., transects #1-1200 in southern
 1493 California). Note that the black blocks in panel B represent the connectivity of major littoral
 1494 cells identified in the model, which are also shown in panel A.

1495

1496 *B.4 Initial conditions for the model ensemble*

1497 The ensemble method presented here applies a user-specified range of randomly generated initial
 1498 conditions of the model state, which are drawn from probability distributions. In general, the

1499 selection process of the range of the initial values for each model parameter is a bit arbitrary and
1500 is subject to some uncertainty. Ideally, the initial range of model parameters should be
1501 motivated by the corresponding values of other modeling studies reported in the literature at
1502 geologically similar sites. Although the initial conditions must be specified directly, we find that
1503 a modest mis-specification (e.g., within an order of magnitude) of the initial parameter ensemble
1504 does not severely degrade the assimilated parameter estimates over time (Evensen, 2003). For
1505 most applications, initial conditions are sampled from normal distributions constructed from a
1506 prescribed mean and standard deviation. In the current application, the $N_{\text{ens}} = 200$ ensemble of
1507 the model state is initialized with normally-distributed random-number generator with zero mean
1508 and standard deviation $\sigma_{Y_{\text{st}}} = 5$ m for the short-term shoreline position, Y_{st} . On the other hand,
1509 the long-term shoreline components (namely Y_{lst} , Y_{brn} , and Y_{vlt}) are considered to be known
1510 initially and hence are set to be identically zero. The initial shoreline position Y_0 for each
1511 transect is also set to a constant value (obtained via nearest neighbor interpolation) that
1512 represents the observed shoreline position that is closest in time to the model start time among
1513 the complete set of observations for a given transect.

1514 The model parameter ensemble is initialized with normal distributions for ΔT and ΔY with
1515 means of $\overline{\Delta T} = 28$ days and $\overline{\Delta Y} = 10$ m, and standard deviations of $\sigma_{\Delta T} = 1$ day and $\sigma_{\Delta Y} = 2$ m,
1516 respectively. The background wave height parameter \hat{H}_s is initialized with a normal distribution
1517 with the mean wave-height time series on each transect (\overline{H}_s) and a standard deviation which is
1518 selected as 7.5% of \overline{H}_s , based on our judgment as a reasonable initial spread of this parameter.
1519 Alongshore smoothing (via a low-pass filter) of the background wave height \hat{H}_s is also applied

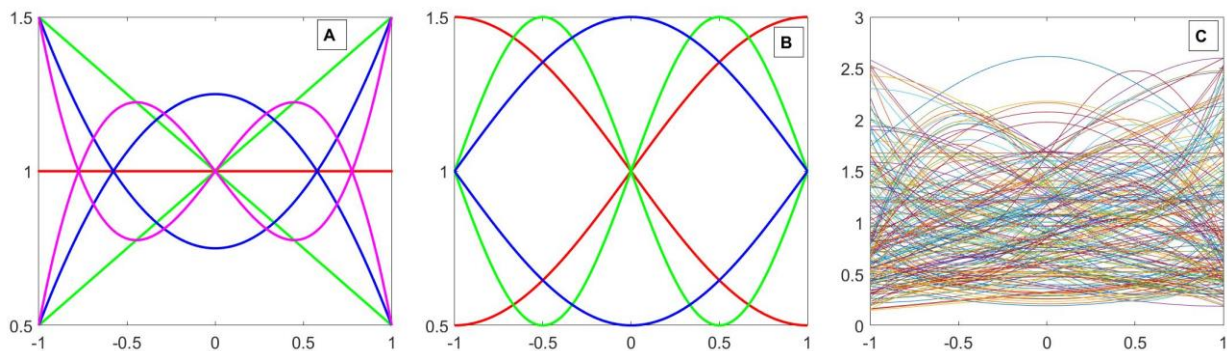
1520 in order to remove high frequency noise/variability in the model parameter (in the alongshore
1521 direction).

1522 The model parameter ensemble is also initialized with normal distributions for c and σ with
1523 means of $\bar{c} = 1$ and $\bar{\sigma} = 0.25$ m, and standard deviations of $\sigma_c = 0.1$ and $\sigma_\sigma = 0.1$ m,
1524 respectively. The long-term shoreline change rate parameter v_{lt} is initialized with a normal
1525 distribution with a standard deviation of $\sigma_{v_{lt}} = 0.05$ m/year and a mean of $\bar{v}_{lt} = 0.25(v_{lt})_0$, where
1526 $(v_{lt})_0$ represents the historical erosion rate obtained via a linear regression fit to all available data
1527 on each transect (see Section 3.1 and Figure 5 for details). In setting the initial rate parameter to
1528 25% of the historical (linear) erosion rate, we implicitly assume that the other resolved long-term
1529 components (e.g., longshore transport and Bruunian response) account for some (i.e., 75%) of
1530 the long-term shoreline change signal, as an initial guess. However, of course, the data-
1531 assimilation method will subsequently calibrate the relative parameters and the contributions of
1532 each shoreline-change component accordingly.

1533 Thus far, we have detailed that all model state and parameter initial conditions are either constant
1534 or have been drawn from normal distributions. However, the longshore transport parameter K
1535 is treated differently: K is initialized with a uniform distribution between values of 0 and 200.
1536 In this case, a uniform distribution is applied to this parameter owing to its underlying
1537 uncertainty and spatial variability in contrast to the equilibrium shoreline parameters (ΔT , ΔY ,
1538 and \hat{H}_s), the long-term parameters (c and v_{lt}), and the noise parameter (σ).

1539 In addition to the procedure in specifying the initial conditions given above, we also impose
1540 longshore variability to the initial parameters ΔT , ΔY , and K . We introduce longshore

1541 structure into the initial parameter ensembles by multiplying the initially longshore-uniform
1542 parameter estimate by a set of simple spatially varying ‘basis functions’ for each littoral cell.
1543 Although the basis functions are rather arbitrary, in the current example, we apply well-known
1544 Legendre polynomials (up to fourth order) and Fourier basis functions (half wave and full wave
1545 sin/cos functions), which are modified to have a unit mean and are shown in Figure 16 panels A
1546 and B, respectively, to construct an overall alongshore structure ensemble (shown in panel C) for
1547 each individual littoral cell. We also randomly scale the basis functions by $\sim \pm 25\%$, in order to
1548 introduce additional magnitude variability into the alongshore structure ensemble. The
1549 alongshore structure ensemble (shown in panel C) is then multiplied by the initial parameter
1550 estimates (for ΔT , ΔY , and K) for each separate littoral cell.



1551

1552 Figure 16 – Simple alongshore basis functions in the form of (modified) Legendre polynomials
1553 (panel A) and Fourier (half and full sin/cos) waves (panel B). An alongshore structure ensemble
1554 (panel C) is constructed from a random sampling and scaling of the simple basis functions shown
1555 in panels A and B. Subsequently, the longshore structure function (shown in panel C) is
1556 multiplied by the initial parameter estimates (for parameters ΔT , ΔY , and K only) for each
1557 separate littoral cell.

1558

1559 The introduction of a longshore structure ensemble into the initial conditions (as opposed to
1560 applying a spatially uniform ensemble) allows the model to encapsulate different possible

1561 realizations of the longshore variability in the model parameters and thus is generally better
1562 conditioned to assimilate (i.e., to nudge the model toward) the correct underlying structure to
1563 emerge from the initially imposed gradients. Although the proposed method has not been fully
1564 tested or optimized (which is beyond the scope of the current paper), we find (from initial tests,
1565 which are not shown) that the longshore-structured, initial ensemble generally outperforms the
1566 alongshore-uniform initial parameter estimates. Further, we also note that even though the *ad*
1567 *hoc* initial longshore structure is imposed in a specific form (analogous to a best-guess initial
1568 condition provided to an optimization routine), the assimilated structure can eventually take on
1569 much more arbitrary complexity than that of the simple functions shown in panel C.

1570 *B.5 Observation error covariance*

1571 A user-defined specification of the spatial correlation (in the alongshore direction) of the error of
1572 satellite-derived shoreline observations is needed for the Kalman filter data-assimilation
1573 operation (described above). Lacking observations of the shoreline error covariance in the
1574 alongshore direction, the observation error covariance matrix \mathbf{R} is often treated as a diagonal
1575 matrix (with $\varepsilon_{\text{RMS}}^2$ sitting on each diagonal entry), where the error in observed shoreline position
1576 (ε_{RMS}) at each transect is assumed to be independent from the error at all other transects, near or
1577 far. However, here, with aid of direct estimates of the shoreline error in space (provided by the
1578 Ocean Beach data described in Section 2.3), we can account for the spatial correlation of the
1579 error using the approach described below.

1580 We compute the (symmetric) observed shoreline error covariance matrix as

$$1581 \quad \mathbf{R}_{i,j} = E(\boldsymbol{\varepsilon}_i \boldsymbol{\varepsilon}_j) \quad (31)$$

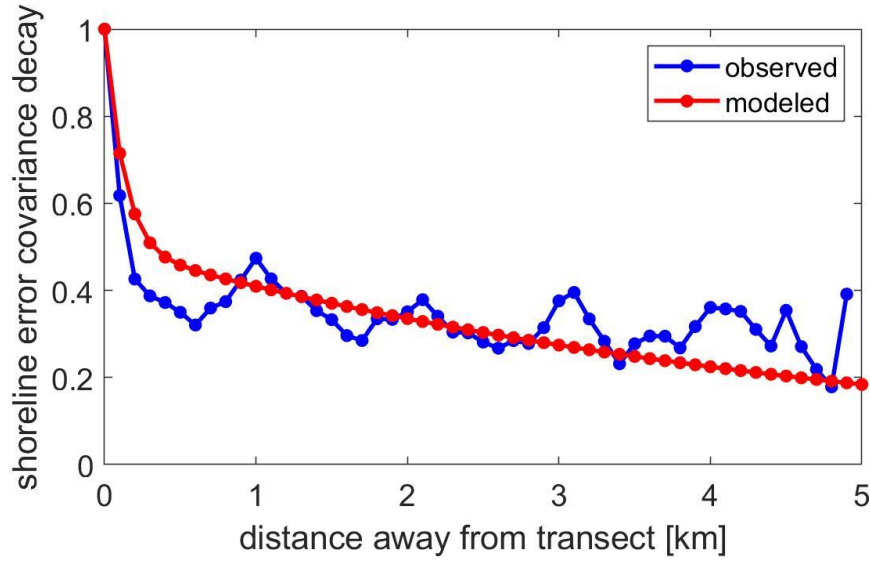
1582 where E is the expected value operator (i.e., the mean, in this case), $\boldsymbol{\varepsilon}_i$ is the time series of the
 1583 shoreline error at transect i (and likewise for transect j). Although \mathbf{R} (Eq. (31)) can, in
 1584 general, only be calculated at sites where ‘ground-truthed’ shoreline observations (e.g., GPS-
 1585 derived shorelines) are available to assess the error in the satellite-derived shorelines (e.g., Ocean
 1586 Beach, in this example), we seek to derive and apply a parameterized version of this \mathbf{R} matrix
 1587 for a broad range of sites lacking in-situ observations. In essence, we seek to understand the
 1588 spatial decay of the shoreline error covariance. To do so, we calculate the covariance decay as a
 1589 function of transect proximity (i.e., distance), k , given by

$$1590 \quad r_k = \frac{\text{median}(\text{diag}(\mathbf{R}, k))}{\text{median}(\text{diag}(\mathbf{R}, 0))} \quad \text{for } k = 0 : N_{\text{transects}} \quad (32)$$

1591 where r_k is the so-called ‘shoreline error covariance decay’, which represents how the shoreline
 1592 error is correlated among nearby transects and becomes increasingly uncorrelated with
 1593 alongshore distance. In Eq. (32), the $\text{diag}(\mathbf{R}, k)$ operation represents the extraction of the k^{th} -
 1594 diagonal of the covariance matrix \mathbf{R} (where $\text{diag}(\mathbf{R}, 0)$ is the main diagonal of \mathbf{R}). In Figure
 1595 17, we fit a smoothed curve (shown in red) of the form

$$1596 \quad \tilde{r}(l) = (\exp(-l/\sigma_1) + 0.5 \tanh(l/\sigma_2)) \exp(-l/\sigma_3) \quad (33)$$

1597 as a function of alongshore distance l to the observed shoreline error covariance decay (shown
 1598 in blue). Eq. (33) represents the sum of a (rapidly) decaying function (\exp) and a plateau
 1599 function (\tanh) that is modulated by another (more slowly) decaying function, parameterized
 1600 with length scales σ_1 , σ_2 , and σ_3 , with values here of 0.2 km, 0.4 km, and 5 km, respectively.



1601

1602 Figure 17 – The variance decay of the shoreline error vs distance away from the transect for the
 1603 Ocean Beach data (blue) and the parameterized version (red).

1604

1605 As described above, in the current modeling application, in absence of direct, site-specific
 1606 observations of the error covariance matrix over the entire model domain, we apply the
 1607 smoothed function \tilde{r} given in Eq. (33) to construct a smoothed error covariance matrix
 1608 according to

$$1609 \quad \tilde{\mathbf{R}}_{i,j} = \tilde{r}(|l_i - l_j|) \varepsilon_{\text{sat}}^2 \quad (34)$$

1610 where $|l_i - l_j|$ is the absolute value of the distance from transect i to transect j and $\varepsilon_{\text{sat}} = 14$ m is
 1611 the RMSE of satellite-derived shorelines as reported above.

1612

1613

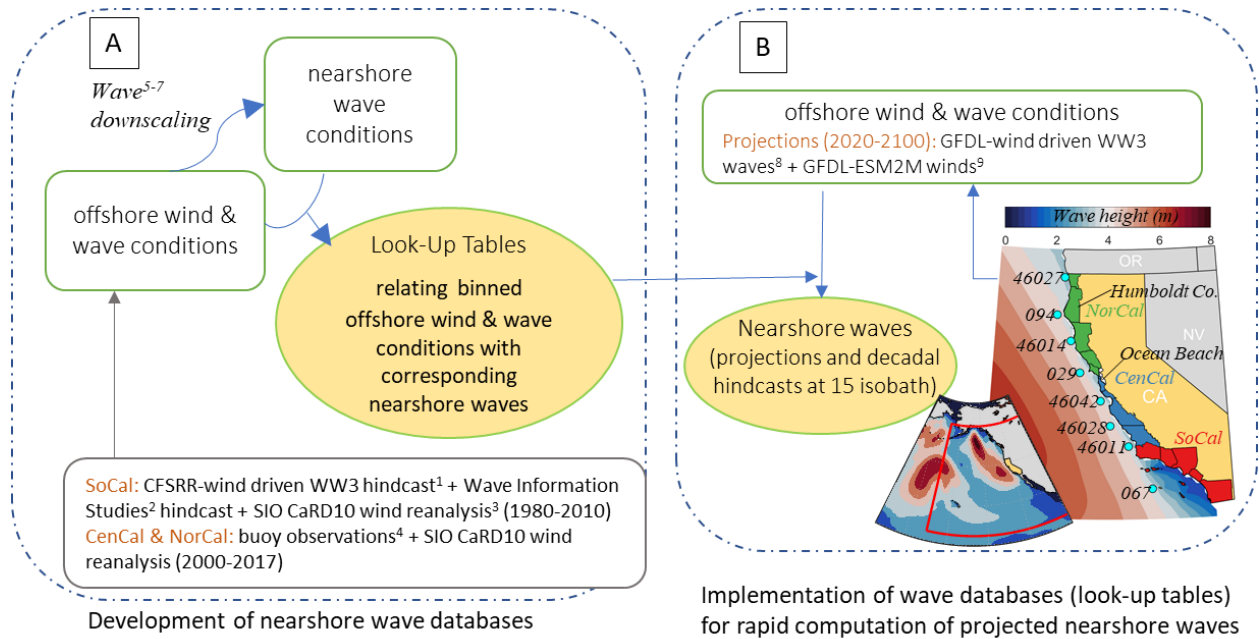
1614

1615 **Appendix C: Model inputs – future climate and management scenarios**

1616 *C.1 Wave modeling*

1617 Climate change is expected to drive changes to mean and extreme wave climates in many areas
1618 (Morim et al., 2019, 2021), which should ideally be accounted for when predicting long-term
1619 coastal evolution. The current shoreline model is forced with a variety of wave hindcast and
1620 wave projection products (as depicted in Figure 18 A and B, respectively), according to their
1621 spatiotemporal availability. Across the vast majority of the hindcasted period (1995-2020),
1622 hindcasted wave conditions (e.g., time series of significant wave height period and direction)
1623 come from the California Coastal Data Information Program – CDIP hindcast (O’Reilly et al.,
1624 2016), which is coincident with model transects and is available from 2000 to 2020. From 1995-
1625 2000, hindcasted wave conditions (Figure 18 A) come from different offshore sources (shown in
1626 the superscripts in Figure 18) including (1) the CFSRR-wind driven WW3 hindcast
1627 (<http://polar.ncep.noaa.gov/waves/hindcasts/nopp-phase2.php>), (2) the US Army Corps of
1628 Engineers Wave Information Studies (WIS; <http://wis.usace.army.mil/>), (3) the CaRD10
1629 reanalysis and projection of winds and sea level pressures. (Scripps Institute of Oceanography,
1630 University of California at San Diego, 2015), (4) Buoy observations from the National Data
1631 Buoy Center (NDBC) site (<https://www.ndbc.noaa.gov/>), which are downscaled to the coast
1632 using look-up tables (5-6: Hegermiller et al., 2016-2017) when the CDIP hindcast (7: O’Reilly et
1633 al., 2016) was unavailable. Beyond 2020, the model is driven by projected time series (2020 to
1634 2100) of daily mean wave heights and corresponding wave periods and directions generated
1635 from a global-to-regional wave model (WaveWatch III; Erikson et al., 2015, depicted using
1636 superscript 8 in Figure 18), which uses wind forcing from the GFDL-ESM2M climate model

1637 (Delworth et al., 2006, depicted with superscript 9 in Figure 18) under the “moderate”
 1638 representative concentration pathway (RCP) 4.5 emissions scenario (Stocker, 2014). Offshore
 1639 wave conditions (Figure 18 B) are, once again, downscaled to each shoreline model transect
 1640 using the look-up-table approach of Hegermiller et al. (2016, 2017).

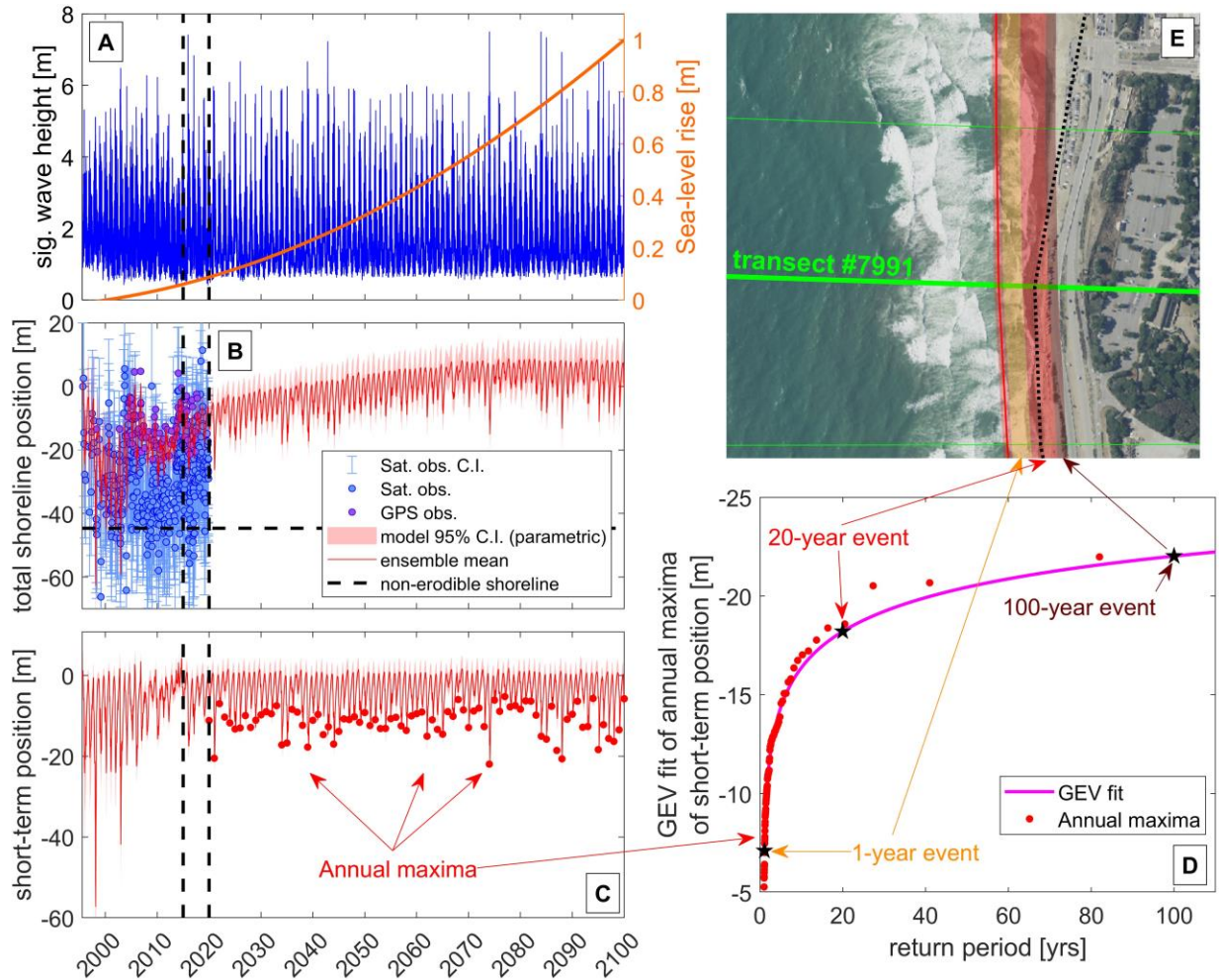


1641

1642 Figure 18 – Overview of the method used to compute nearshore (15 m isobath) wave time-series
 1643 for the years 2020 to 2100. A) Look-up tables that relate binned offshore wind (magnitude and
 1644 direction) and wave (height, period, and direction) conditions to nearshore waves were
 1645 developed by finding corresponding nearshore wave conditions generated from high resolution
 1646 nearshore wave downscaling models. Downscaling of nearshore wave conditions was achieved
 1647 with high spatiotemporal resolution SWAN models for southern California and ray tracing
 1648 techniques for central and northern California (i.e., the CDIP hindcast). B) Implementation of
 1649 the look-up tables for rapid downscaling of projected offshore wind and wave conditions to the
 1650 nearshore. Projected offshore wave conditions were derived with the numerical wave model
 1651 WaveWatch III (NOAA) forced with winds from the GFDL-ESM2M RCP 4.5 climate model.
 1652 The WaveWatch III model consists of a global and nested regional Eastern North Pacific grid
 1653 (0.25° resolution; red line shown in inset). Wave buoys used to translate offshore conditions to
 1654 the nearshore are shown with cyan circles (5- and 3-digit numbers refer to NDBC- and CDIP-
 1655 owned buoys, respectively). Wave height maps represent a sample time-point from January 10th,
 1656 2044.

1658 Accurate hindcasts and projections of nearshore wave conditions are needed in the current
1659 application because the model formulations in Eq. (1) are highly sensitive to wave conditions. In
1660 particular, anomalies/variations in wave angle and wave energy can significantly affect the
1661 calculation of longshore transport (via Eq. (8); e.g., Chataigner et al., 2022) and equilibrium
1662 shoreline response (via Eqs. (10) - (11); e.g., Vitousek et al., 2021), respectively. In the current
1663 application, the shoreline model is forced with a single projected time series of wave conditions
1664 (from Hegermiller et al., 2016). However, this wave forcing time series represents only a single
1665 realization of the stochastic wave climate system. Use of an ensemble wave forcing approach
1666 (e.g., Davidson, et al. 2017, Cagigal et al., 2020) would likely improve the range of potential
1667 short-term shoreline positions and estimates of uncertainty as shown in Vitousek et al. (2021).
1668 However, the uncertainty of long-term wave-driven shoreline change (e.g., due to longshore
1669 transport) and sea-level rise will still generally be well captured by the ‘single realization’
1670 approach used here since the long-term processes are driven more by the mean wave climatology
1671 rather than the instantaneous weather/wave conditions. Nevertheless, to compensate for not
1672 applying ensemble wave conditions, we provide (at each transect location) estimates of
1673 intrinsic/aleatoric uncertainty in shoreline position associated with annual, 20-year, and 100-year
1674 return period wave events, following Davidson et al. (2017), as demonstrated in Figure 19. The
1675 method used here fits a Generalized Extreme Value (GEV) distribution (see Coles et al., 2001) to
1676 the annual maxima in the short-term shoreline position, Y_{st} , as shown in the red dots in Figure
1677 19 C and D. 1-year, 20-year, and 100-year erosion events are the estimated from the fitted GEV
1678 distribution (purple line in Figure 19 D). Finally, storm-driven erosion uncertainty bands
1679 corresponding to 1-year, 20-year, and 100-year erosion event levels are then superimposed onto

1680 the model projections at each transect (as shown in the yellow, red, and brown bands of panel
 1681 Figure 19 E, respectively).

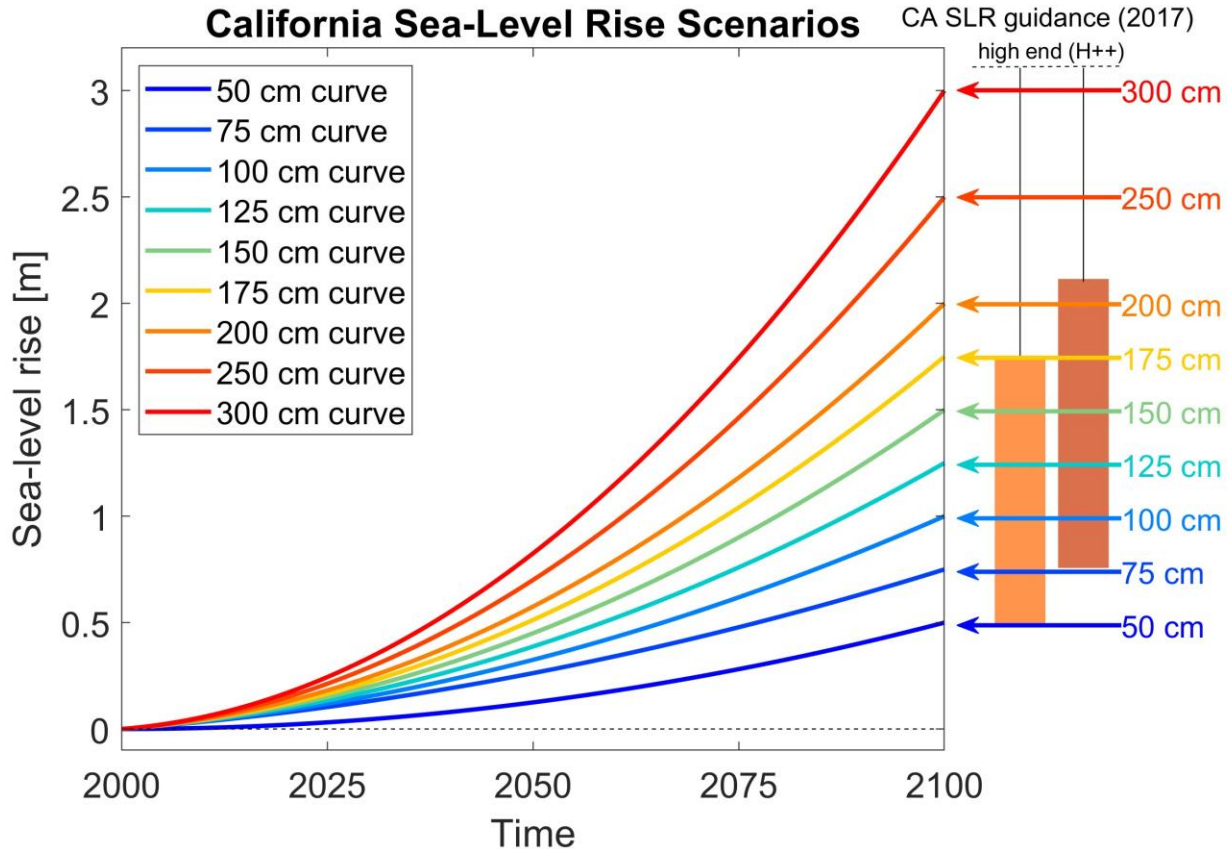


1682
 1683 Figure 19 – An example of CoSMoS-COAST simulations of total shoreline position (panel B)
 1684 and short-term shoreline position (panel C) in response to projected wave and sea-level
 1685 conditions (panel C) at transect 7991 at Ocean Beach, California. A Generalized Extreme Value
 1686 (GEV) distribution (purple line in panel D) is fit to the annual maxima in the short-term shoreline
 1687 position (red dots in panels C and D). 1-year, 20-year, and 100-year erosion events are estimated
 1688 from the fitted GEV distribution (panel D), and storm-driven erosion uncertainty bands
 1689 corresponding to these event levels are then mapped onto each transect (as shown in the yellow,
 1690 red, and brown bands of panel E, respectively). (Basemap is from a current, high-resolution
 1691 aerial photograph of Ocean Beach available through NOAA Digital Coast).

1692

1693 *C.2 Sea-level rise scenarios*

1694 The uncertainty of future coastal erosion is intimately linked to sea-level rise (Anderson et al.,
1695 2015; Vitousek et al., 2017; Le Cozannet et al., 2019; Vousdoukas et al., 2020; D’Anna et al.,
1696 2021a, 2022). In the current application, we consider nine sea-level rise scenarios: 0.5, 0.75, 1.0,
1697 1.25, 1.5, 1.75, 2.0, 2.5, and 3.0 m (shown in Figure 20), which cover the range of physically
1698 tenable sea-level outcomes in California over the 21st century (e.g., Griggs et al., 2017, Sweet et
1699 al., 2022). The high-end sea-level scenarios, used here, as shown in Figure 20, are consistent
1700 with the so-called ‘H++’ scenario (Sweet et al., 2017), which represent a scenario of extreme ice
1701 melt in the West Antarctic ice sheet. As in Vitousek et al. (2017), sea level versus time is
1702 modeled as a quadratic function. The three unknown coefficients of the quadratic curve are
1703 obtained via three equations: (1) The mean sea level in 2000 is assumed to be at zero elevation,
1704 (2) the rate of SLR in 2000 is assumed to be 3 mm/yr, which is consistent with global mean
1705 values of sea-level rise observed via satellites, (3) future sea-level elevation at 2100 is assumed
1706 to be 0.5, 0.75, 1.0, 1.25, 1.5, 1.75, 2.0, 2.5, or 3.0 m based on the scenarios considered (see
1707 Figure 20). We note that, in the current application, sea level only forces equilibrium profile
1708 changes via the third term on the right-hand side of Eq. (1), which is in line with many recent
1709 studies (Anderson et al., 2015; Vitousek et al., 2017; Le Cozannet et al., 2019; Vousdoukas et al.,
1710 2020; D’Anna et al., 2021a, 2022)



1711

1712 Figure 20 – Scenarios of sea-level rise (i.e., 0.5, 0.75, 1.0, 1.25, 1.5, 1.75, 2.0, 2.5, or 3.0 m) used
 1713 in the current application, which follow from the California Guidance (Griggs et al., 2017).

1714

1715 *C.3 Coastal management scenarios*

1716 In this application, we explore the combination of nine sea-level projections (see Figure 20) and
 1717 four management scenarios. The four management scenarios result from two independent,
 1718 binary scenarios, namely, “hold the line” and “continued nourishment”. The “hold the line”
 1719 scenario represents the management decision to prevent or allow the shoreline from receding
 1720 past existing infrastructure (e.g., by permitting or prohibiting shoreline armoring, respectively) or
 1721 naturally hardened shorelines (e.g., cliffs, bluffs, and headlands). If the line is held, then the
 1722 modeled shoreline is constrained from eroding past a so-called ‘non-erodible shoreline’, which is

1723 manually digitized from recent aerial and satellite imagery and represents the division of beach
1724 and urban infrastructure, cliffs, or highly vegetated areas (following Vitousek et al., 2017). If the
1725 line is not held, then the shoreline is allowed to erode into existing infrastructure and coastal
1726 cliffs without impediment as if the eroded substrate is the same as a sandy beach. As in the
1727 original CoSMoS-COAST model application (Vitousek et al., 2017), we assume that any dunes
1728 or cliffs do not erode landward with the beach, and that the non-erodible shoreline stays fixed
1729 through time.

1730 The “continued accretion” scenario represents the management decision to continue or cease the
1731 long-term residual shoreline trend (which can be affected by processes such as beach
1732 nourishment, fluvial sediment input, and other sources of sediment that contribute to chronic
1733 accretion) determined from assimilation of recent historical data (1995-2020). The scenario was
1734 previously called “continued nourishment” in Vitousek et al. (2017) when the model domain was
1735 limited to southern California, where some nourishment projects have taken place. The current
1736 application spans all of California, where nourishments are rare in central and northern
1737 California. Hence, the scenario, now referred to as “continued accretion”, assumes that both
1738 natural (e.g., fluvial) and anthropogenic (e.g., nourishment) accretionary signals will persist or
1739 cease. In the model, the “continued accretion” scenario is implemented allowing the data-
1740 assimilated value of v_{it} to remain unchanged during the forecast period (2020-2100). On the
1741 other hand, the “no continued nourishment” scenario forces $v_{it} = 0$ starting in 2020 (at the end of
1742 the validation period) for each accreting transect where $v_{it} > 0$. We note that any chronically
1743 eroding transects (with $v_{it} < 0$) are held constant at the end of the data-assimilation period, and
1744 thus are unaffected by the choice of the “continued accretion” vs “no continued accretion”

1745 scenario. The 9 sea-level scenarios and 4 management scenarios combine to give a total of 36
1746 different models run as part of this effort. For each scenario, we provide time series of expected
1747 shoreline change including long-term erosion hazards zone (median projection + 95% confidence
1748 intervals for the parametric and structural uncertainty) plus additional storm-driven erosion
1749 hazard zones that correspond to annual, 20-year, and 100-year return period wave-driven erosion
1750 events. Above, the ‘Data availability statement’ contains information on where the model-
1751 projections, produced as part of this study, can be accessed.

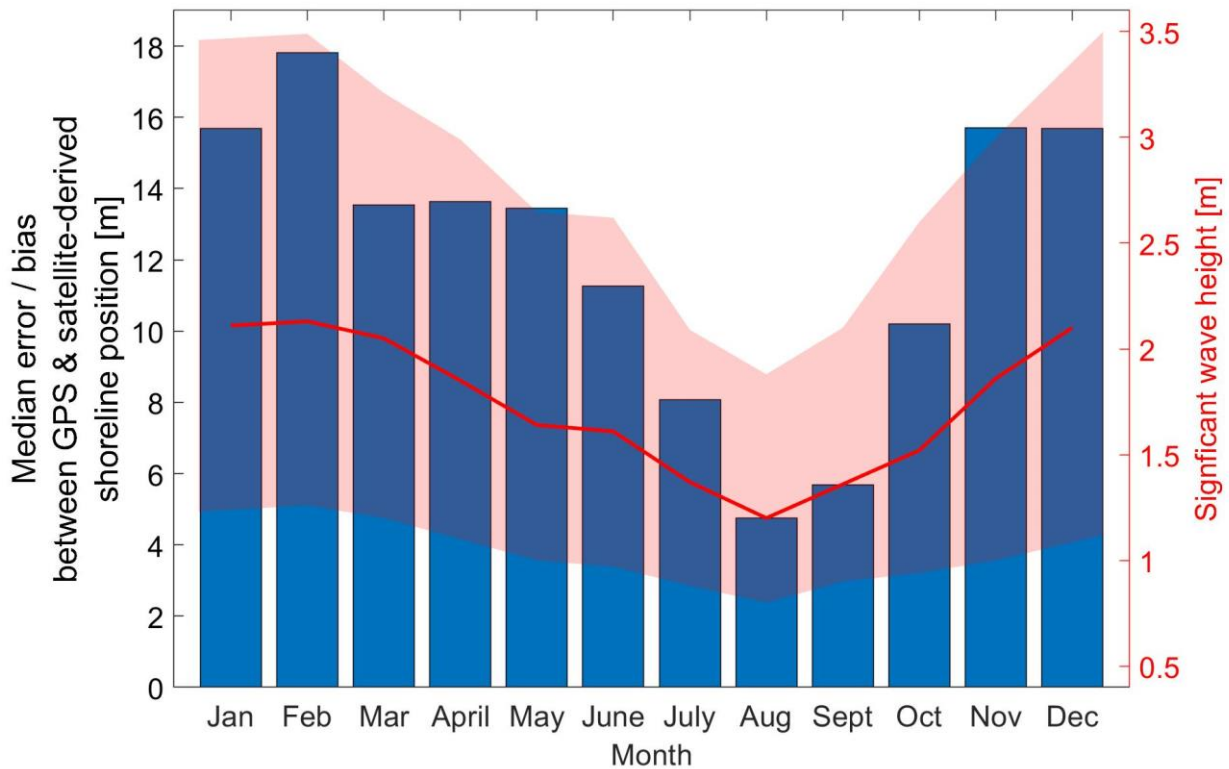
1752

1753 **Appendix D: Satellite-derived shoreline error and ‘proxy-datum bias’**

1754 The so-called ‘proxy-datum bias’ (Moore et al., 2006; Ruggiero & List, 2009) is a well-known
1755 source of error in historical shoreline analyses that combine data sets of both elevation/datum-
1756 based surveys (e.g., Lidar/GPS) and visual/proxy-based (e.g., digitized shorelines from aerial
1757 photos) shoreline observations. In short, there can often be a slight offset or ‘bias’ between the
1758 two different sources of data, which should ideally be accounted/corrected for. The proxy-datum
1759 bias remains poorly understood in the context of satellite derived shoreline observations. Below,
1760 we seek to explore the proxy-datum bias of satellite-derived shorelines with the aid of monthly
1761 GPS observations at Ocean Beach, California.

1762 Figure 21 shows a histogram of the median error in tide-corrected satellite derived shoreline
1763 position (i.e., GPS shoreline position minus the satellite-derived shoreline position) for all Ocean
1764 Beach transects as a function of month. Hence, positive values of the error indicate that the
1765 satellite-derived shorelines are consistently located farther landward than GPS-derived MSL
1766 shoreline contour. We hypothesize that the landward bias of the tide-corrected satellite

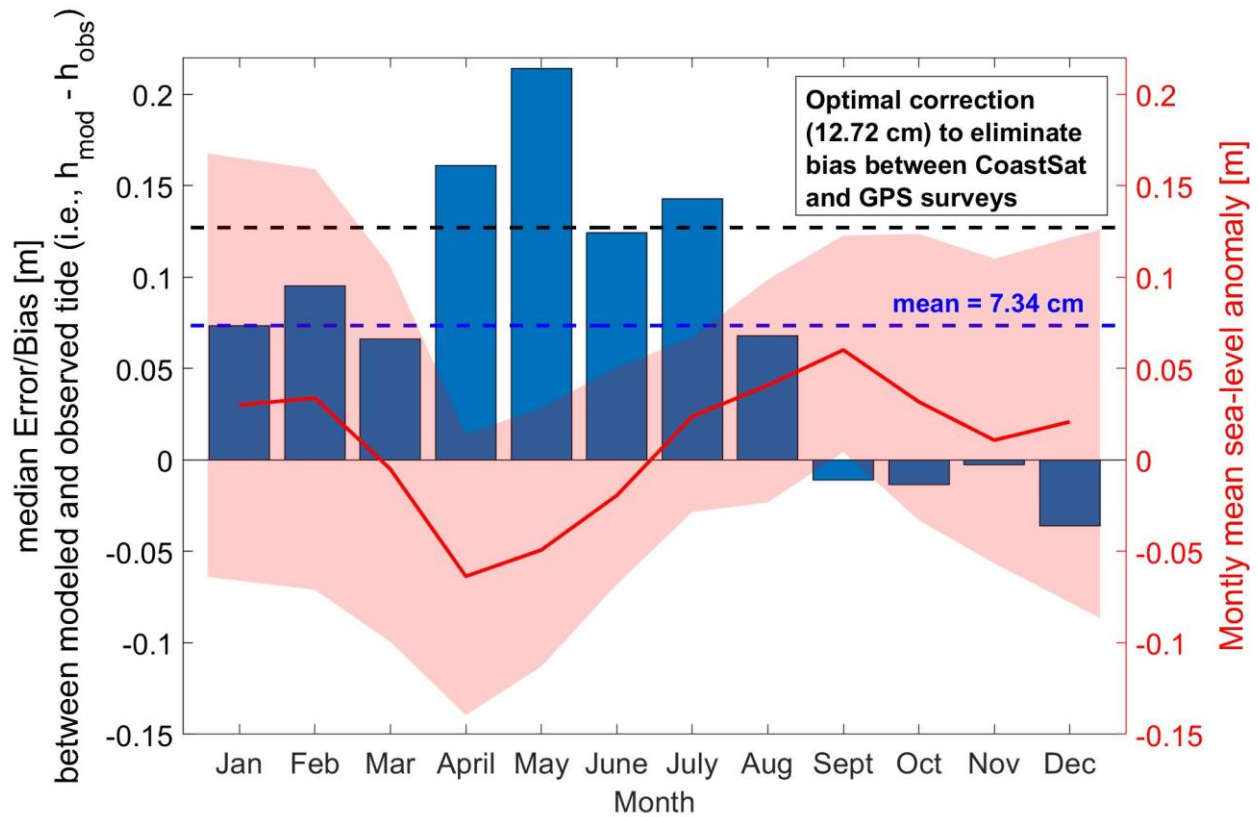
1767 observations shown in Figure 21 is due to wave setup (i.e., the persistent increase in nearshore
 1768 water levels due to wave breaking, which can be corrected for). This hypothesis is supported by
 1769 comparing the shoreline error (y-axis on the left side of Figure 21) to the median significant
 1770 wave height (y-axis on the right side of Figure 21, which recorded at the NOAA National Data
 1771 Buoy Center’s San Francisco wave buoy #46026, located 33 km offshore from Ocean Beach).
 1772 The pink bands on Figure 21 represent the 20th to 80th percentiles of the monthly wave height
 1773 about the median monthly significant wave height (solid red line). Figure 21 demonstrates that
 1774 the bias is correlated with wave height: the bias is largest in February when the waves are
 1775 generally the largest, and conversely, the bias is smallest in August when the waves are generally
 1776 the smallest.



1777

1778 Figure 21 – The error/bias in meters between the GPS surveys and the satellite-derived shoreline
 1779 position at Ocean Beach, San Francisco, California as a function of month. The median of the
 1780 monthly significant wave height is shown as a solid red line with the pink envelope representing
 1781 the 20% to 80% percentiles of the monthly wave height.

1782



1783

1784 Figure 22 – The median error / bias between the modeled and observed tide at Ocean Beach, San
 1785 Francisco, California as a function of month (blue bars). The bias is likely due to (negative)
 1786 monthly mean sea-level anomalies (typically associated with upwelling-favorable winds in
 1787 spring), shown in red with 80% confidence bands in pink, which are not resolved in the tidal
 1788 model.

1789

1790 As discussed in Section 2.3, much of the error/bias between (water-level-dependent, proxy-
 1791 based) satellite derived shorelines and (water-level invariant, datum-based) GPS shorelines can

1792 be attributed to the instantaneous water level. Figure 22 shows the median difference between
1793 modeled (using the Finite-Element Solution (FES) ocean model – Lyard et al., 2021) and
1794 observed water levels (using the San Francisco tide-gauge station #9414290) near Ocean Beach,
1795 San Francisco, California, as a function of month. We also compare the modeled-water-level
1796 error (y-axis on the left) to the monthly mean sea-level anomaly (y-axis on the right) on Figure
1797 22, where the pink bands represent the 20 to 80% percentiles of the monthly wave height about
1798 the median (solid red line). The mean difference between the modeled and observed water level
1799 across all months is 7.34 cm, which is compared to the optimal correction value of 12.72 cm,
1800 found in Section 2.3. This indicates that more than half of the proxy-datum bias (after correcting
1801 for tide, setup, and monthly-mean sea-level anomalies) of satellite-derived shorelines is likely
1802 due to the water-level offset between the modeled and observed water. The difference between
1803 modeled and observed water level may be due to dynamic, oceanographic processes (which may
1804 be difficult to rectify via modeling) and/or datum issues (which may be easy to rectify via an
1805 appropriate, additive constant determined from observations). It is well known (Gill & Clarke,
1806 1974; Schwing, 2000) that upwelling-favorable winds on the California coast during spring and
1807 early summer months decrease nearshore sea levels (see red line on Figure 22), which are not
1808 resolved in the FES-modeled astronomical tidal predictions and may contribute to the model’s
1809 over-prediction of spring/summer water levels in Figure 22. It is also possible that the image-
1810 processing algorithm that identifies the shoreline (i.e., the division between water and sand) may
1811 be slightly biased toward detecting wet sand (i.e., a landward bias) or subaqueous shoreline
1812 features (i.e., seaward bias), as is known to occur in certain settings like macrotidal environments
1813 (Castelle et al., 2021). However, the relative contributions to the overall bias are difficult, if not
1814 impossible, to diagnose in the absence of additional ‘ground-truth’ observations. Nevertheless,

1815 we find (in Figure 21 and Figure 22) that both waves and water levels play strong roles in the
1816 identification of shoreline position in satellite imagery at Ocean Beach. As shown here and in
1817 Section 2.3, with the aid of some corrections, we can obtain nearly unbiased estimate of the
1818 shoreline position at Ocean Beach from satellite imagery. Further, we can apply these water-
1819 level-correction methods more broadly to (presumably) obtain more accurate satellite-derived
1820 shoreline observations in otherwise data-deficient locations.

1821 **References:**

- 1822 1. Alessio, P., & Keller, E. A. (2020). Short-term patterns and processes of coastal cliff
1823 erosion in Santa Barbara, California. *Geomorphology*, 353, 106994.
1824
- 1825 2. Alvarez-Cuesta, M., Toimil, A., & Losada, I. J. (2021). Modelling long-term shoreline
1826 evolution in highly anthropized coastal areas. Part 1: Model description and validation.
1827 *Coastal Engineering*, 169, 103960.
1828
- 1829 3. Alvarez-Cuesta, M., Toimil, A., & Losada, Y. I. (2021). Reprint of: Modelling long-term
1830 shoreline evolution in highly anthropized coastal areas. Part 2: Assessing the response to
1831 climate change. *Coastal Engineering*, 169, 103985.
1832
- 1833 4. Anderson, D., Ruggiero, P., Antolínez, J. A., Méndez, F. J., & Allan, J. (2018). A climate
1834 index optimized for longshore sediment transport reveals interannual and multidecadal
1835 littoral cell rotations. *Journal of Geophysical Research: Earth Surface*, 123(8), 1958-
1836 1981.
- 1837 5. Anderson, T. R., Fletcher, C. H., Barbee, M. M., Frazer, L. N., & Romine, B. M. (2015).
1838 Doubling of coastal erosion under rising sea level by mid-century in Hawaii. *Natural*
1839 *Hazards*, 78(1), 75-103.
- 1840 6. Antolínez, José AA; Méndez, Fernando J; Anderson, Dylan; Ruggiero, Peter; Kaminsky,
1841 George M; Predicting climate driven coastlines with a simple and efficient multi-scale
1842 model. *Journal of Geophysical Research: Earth Surface* (2019)
- 1843 7. Armstrong, S. B., & Lazarus, E. D. (2019). Masked shoreline erosion at large spatial
1844 scales as a collective effect of beach nourishment. *Earth's Future*, 7(2), 74-84.
- 1845 8. Ashton, A., Murray, A. B., & Arnoult, O. (2001). Formation of coastline features by
1846 large-scale instabilities induced by high-angle waves. *Nature*, 414(6861), 296-300.
- 1847 9. Ashton, A. D., & Murray, A. B. (2006). "High-angle wave instability and emergent
1848 shoreline shapes: 1. Modeling of sand waves, flying spits, and capes." *Journal of*
1849 *Geophysical Research: Earth Surface* (2003–2012), 111(F4).

- 1850 10. Bannister, RN; A review of operational methods of variational and ensemble-variational
1851 data assimilation. Quarterly Journal of the Royal Meteorological Society. 143 703 607-
1852 633 (2017)
- 1853 11. Banno, M.; Kuriyama, Y.; Hashimoto, N; Equilibrium-based foreshore beach profile
1854 change model for long-term data. In The Proceedings of the Coastal Sediments 2015
1855 (2015).
- 1856 12. Banno, M., Nakamura, S., Kosako, T., Nakagawa, Y., Yanagishima, S. I., & Kuriyama,
1857 Y. (2020). Long-Term Observations of Beach Variability at Hasaki, Japan. Journal of
1858 Marine Science and Engineering, 8(11), 871.
- 1859 13. Barnard, P. L., Hansen, J. E., & Erikson, L. H. (2012). Synthesis study of an erosion hot
1860 spot, Ocean Beach, California. Journal of Coastal Research, 28(4), 903-922.
- 1861 14. Barnard, P. L., van Ormondt, M., Erikson, L. H., Eshleman, J., Hapke, C., Ruggiero, P.,
1862 Adams P. N., & Foxgrover, A. C. (2014). Development of the Coastal Storm Modeling
1863 System (CoSMoS) for predicting the impact of storms on high-energy, active-margin
1864 coasts. Natural hazards, 74(2), 1095-1125.
- 1865 15. Bruun, P. (1962). Sea-level rise as a cause of shore erosion. Journal of the Waterways
1866 and Harbors division, 88(1), 117-132.
- 1867 16. Cagigal, L.; Rueda, A.; Anderson, D.; Ruggiero, P.; Merrifield, M. A.; Montaña, J.,
1868 Coco, G.; Méndez, F. J.; A multivariate, stochastic, climate-based wave emulator for
1869 shoreline change modelling. Ocean Modelling, 101695. (2020).
- 1870 17. Calkoen, F., Luijendijk, A., Rivero, C. R., Kras, E., & Baart, F. (2021). Traditional vs.
1871 machine-learning methods for forecasting sandy shoreline evolution using historic
1872 satellite-derived shorelines. Remote Sensing, 13(5), 934.
- 1873 18. Castelle, B., Marieu, V., Bujan, S., Ferreira, S., Parisot, J. P., Capo, S., ... & Chouzenoux,
1874 T. (2014). Equilibrium shoreline modelling of a high-energy meso-macrotidal multiple-
1875 barred beach. Marine Geology, 347, 85-94.
- 1876 19. Castelle, B., Masselink, G., Scott, T., Stokes, C., Konstantinou, A., Marieu, V., & Bujan,
1877 S. (2021). Satellite-derived shoreline detection at a high-energy meso-macrotidal beach.
1878 Geomorphology, 383, 107707.
- 1879 20. Castelle, B., Ritz, A., Marieu, V., Lerma, A. N., & Vandenhove, M. (2022). Primary
1880 drivers of multidecadal spatial and temporal patterns of shoreline change derived from
1881 optical satellite imagery. Geomorphology, 108360.
- 1882 21. Callaghan, David P; Ranasinghe, Roshanka; Roelvink, Dano; Probabilistic estimation of
1883 storm erosion using analytical, semi-empirical, and process based storm erosion models.
1884 Coastal Engineering 82 64-75(2013)
- 1885 22. Chataigner, T., Yates, M. L., Le Dantec, N., Harley, M. D., Splinter, K. D., & Goutal, N.
1886 (2022). Sensitivity of a one-line longshore shoreline change model to the mean wave
1887 direction. Coastal Engineering, 172, 104025.

- 1888 23. Coastal Data Information Program (CDIP) (2016) Scripps Institution of Oceanography,
1889 Integrative Oceanography Division, San Diego, <http://cdip.ucsd.edu>
- 1890 24. Coles, S., Bawa, J., Trenner, L., & Dorazio, P. (2001). An introduction to statistical
1891 modeling of extreme values (Vol. 208, p. 208). London: Springer.
- 1892 25. Cooper, J. A. G., & Pilkey, O. H. (2004). Sea-level rise and shoreline retreat: time to
1893 abandon the Bruun Rule. *Global and planetary change*, 43(3), 157-171.
- 1894 26. Cooper, J. A. G., Masselink, G., Coco, G., Short, A. D., Castelle, B., Rogers, K., ... &
1895 Jackson, D. W. T. (2020). Sandy beaches can survive sea-level rise. *Nature Climate*
1896 *Change*, 10(11), 993-995.
- 1897 27. Dabees, M. A. (2000). Efficient modeling of beach evolution. PhD Thesis. Queen's
1898 University.
- 1899 28. Davidson-Arnott, R. G. (2005). Conceptual model of the effects of sea level rise on sandy
1900 coasts. *Journal of Coastal Research*, 1166-1172.
- 1901 29. Davidson-Arnott, R. G., & Bauer, B. O. (2021). Controls on the geomorphic response of
1902 beach-dune systems to water level rise. *Journal of Great Lakes Research*, 47(6), 1594-
1903 1612.
- 1904 30. Davidson, MA; Splinter, KD; Turner, IL; A simple equilibrium model for predicting
1905 shoreline change. *Coastal Engineering* 73 191-202 (2013)
- 1906 31. Davidson, Mark A; Turner, Ian L; Splinter, Kristen D; Harley, Mitchel D; Annual
1907 prediction of shoreline erosion and subsequent recovery. *Coastal Engineering* 130 14-25
1908 (2017)
- 1909 32. D'Anna, Maurizio; Idier, Déborah; Castelle, Bruno; Rohmer, Jeremy; Le Cozannet,
1910 Goneri; Robinet, Arthur. Impact of model free parameters and sea-level rise uncertainties
1911 on 20-years shoreline hindcast: the case of Truc Vert beach (SW France). *Earth Surface*
1912 *Processes and Landforms* (2020)
- 1913 33. D'Anna, M., Castelle, B., Idier, D., Rohmer, J., Le Cozannet, G., Thiéblemont, R., &
1914 Bricheno, L. (2021a). Uncertainties in Shoreline Projections to 2100 at Truc Vert Beach
1915 (France): Role of Sea-Level Rise and Equilibrium Model Assumptions. *Journal of*
1916 *Geophysical Research: Earth Surface*, 126(8), e2021JF006160.
- 1917 34. D'Anna, M., Idier, D., Castelle, B., Vitousek, S., & Le Cozannet, G. (2021b).
1918 Reinterpreting the Bruun rule in the context of equilibrium shoreline models. *Journal of*
1919 *Marine Science and Engineering*, 9(9), 974.
- 1920 35. D'Anna, M., Idier, D., Castelle, B., Rohmer, J., Cagigal, L., & Mendez, F. J. (2022).
1921 Effects of stochastic wave forcing on probabilistic equilibrium shoreline response across
1922 the 21st century including sea-level rise. *Coastal Engineering*, 175, 104149.
- 1923 36. Debreu, L., Marchesiello, P., Penven, P., & Cambon, G. (2012). Two-way nesting in
1924 split-explicit ocean models: Algorithms, implementation and validation. *Ocean*
1925 *Modelling*, 49, 1-21.

- 1926 37. East, A. E., Stevens, A. W., Ritchie, A. C., Barnard, P. L., Campbell-Swarzenski, P.,
1927 Collins, B. D., & Conaway, C. H. (2018). A regime shift in sediment export from a
1928 coastal watershed during a record wet winter, California: Implications for landscape
1929 response to hydroclimatic extremes. *Earth Surface Processes and Landforms*, 43(12),
1930 2562-2577.
- 1931 38. Evensen, Geir; Sequential data assimilation with a nonlinear quasi-geostrophic model
1932 using Monte Carlo methods to forecast error statistics. *Journal of Geophysical Research:*
1933 *Oceans* 99 C5 10143-10162. (1994)
- 1934 39. Flick, R. E. (1993). The myth and reality of southern California beaches. *Shore and*
1935 *Beach*, 61(3), 3-13.
- 1936 40. Gill, A. E., & Clarke, A. J. (1974, May). Wind-induced upwelling, coastal currents and
1937 sea-level changes. In *Deep Sea Research and Oceanographic Abstracts* (Vol. 21, No. 5,
1938 pp. 325-345). Elsevier.
- 1939 41. Griggs, G., Patsch, K., Lester, C., & Anderson, R. (2020). Groins, sand retention, and the
1940 future of Southern California's beaches. *Shore & Beach*, 88(2), 14-36.
- 1941 42. Griggs, G, Árvai, J, Cayan, D, DeConto, R, Fox, J, Fricker, HA, Kopp, RE, Tebaldi, C,
1942 Whiteman, EA (California Ocean Protection Council Science Advisory Team Working
1943 Group). *Rising Seas in California: An Update on Sea-Level Rise Science*. California
1944 Ocean Science Trust, April 2017
- 1945 43. Hagenars, G., Luijendijk, A., de Vries, S., & de Boer, W. (2017). Long term coastline
1946 monitoring derived from satellite imagery. In *Coastal Dynamics* (Vol. 122, pp. 1551-
1947 1562).
- 1948 44. Hamill, T. M., Whitaker, J. S., & Snyder, C. (2001). Distance-dependent filtering of
1949 background error covariance estimates in an ensemble Kalman filter. *Monthly Weather*
1950 *Review*, 129(11), 2776-2790.
- 1951 45. Hansen, J. E., & Barnard, P. L. (2010). Sub-weekly to interannual variability of a high-
1952 energy shoreline. *Coastal Engineering*, 57(11-12), 959-972.
- 1953 46. Hapke, C. J., Reid, D., Richmond, B. M., Ruggiero, P., & List, J. (2006). National
1954 assessment of shoreline change Part 3: Historical shoreline change and associated coastal
1955 land loss along sandy shorelines of the California Coast. *US Geological Survey Open File*
1956 *Report*, 1219, 27.
- 1957 47. Hegermiller, Christie A; Erikson, Li H; Barnard, Patrick L; Nearshore waves in Southern
1958 California: Hindcast, and modeled historical and 21st century projected time series. *US*
1959 *Geological Survey summary of methods to accompany data release*. (2016)
- 1960 48. Hegermiller, C.A., et al, 2017, Controls of multi-modal wave conditions in a complex
1961 coastal setting: *Geophysical Research Letters*, <https://doi.org/10.1002/2017GL075272>.
- 1962 49. Hersbach, H., Bell, B., Berrisford, P., Hirahara, S., Horányi, A., Muñoz-Sabater, J., ... &
1963 Thépaut, J. N. (2020). The ERA5 global reanalysis. *Quarterly Journal of the Royal*
1964 *Meteorological Society*, 146(730), 1999-2049.

- 1965 50. Hunt, E., Davidson, M., Steele, E. C., Amies, J. D., Scott, T., & Russell, P. (2023).
 1966 Shoreline modelling on timescales of days to decades. *Cambridge Prisms: Coastal*
 1967 *Futures*, 1-26.
- 1968 51. Hurst, M. D., Barkwith, A., Ellis, M. A., Thomas, C. W., & Murray, A. B. (2015).
 1969 Exploring the sensitivities of crenulate bay shorelines to wave climates using a new
 1970 vector-based one-line model. *Journal of Geophysical Research: Earth Surface*.
- 1971 52. Ibaceta, R., Splinter, K. D., Harley, M. D., & Turner, I. L. (2020). Enhanced coastal
 1972 shoreline modeling using an ensemble kalman filter to include nonstationarity in future
 1973 wave climates. *Geophysical Research Letters*, 47(22), e2020GL090724.
- 1974 53. Kaergaard, K., & Fredsoe, J. (2013). A numerical shoreline model for shorelines with
 1975 large curvature. *Coastal Engineering*, 74, 19-32.
- 1976 54. Kroon, Anna, Matthieu de Schipper, Pieter van Gelder, and Stefan Aarninkhof. Ranking
 1977 uncertainty: Wave climate variability versus model uncertainty in probabilistic
 1978 assessment of coastline change. *Coastal Engineering* 103673 (2020)
- 1979 55. Larson, M., & Kraus, N. C. (1994). Temporal and spatial scales of beach profile change,
 1980 Duck, North Carolina. *Marine Geology*, 117(1-4), 75-94.
- 1981 56. Larson, M., Hanson, H. and Kraus, N.C. (1997). Analytical solutions of one-line model
 1982 for shoreline change near coastal structures. *Journal of Waterway, Port, Coastal, and*
 1983 *Ocean Engineering* 123 (4), 180-191.
- 1984 57. Lazarus, E. D., & Goldstein, E. B. (2019). Is there a bulldozer in your model?. *Journal of*
 1985 *Geophysical Research: Earth Surface*, 124(3), 696-699.
- 1986 58. Le Cozannet, G., Bulteau, T., Castelle, B., Ranasinghe, R., Wöppelmann, G., Rohmer, J.,
 1987 ... & Salas-y-Mélie, D. (2019). Quantifying uncertainties of sandy shoreline change
 1988 projections as sea level rises. *Scientific reports*, 9(1), 1-11.
- 1989 59. Lentz, E. E., & Hapke, C. J. (2011). Geologic framework influences on the
 1990 geomorphology of an anthropogenically modified barrier island: Assessment of
 1991 dune/beach changes at Fire Island, New York. *Geomorphology*, 126(1-2), 82-96.
- 1992 60. Limber, P. W., & Murray, A. B. (2011). Beach and sea-cliff dynamics as a driver of long-
 1993 term rocky coastline evolution and stability. *Geology*, 39(12), 1147-1150.
- 1994 61. Limber, P. W., Barnard, P. L., Vitousek, S., & Erikson, L. H. (2018). A model ensemble
 1995 for projecting multidecadal coastal cliff retreat during the 21st century. *Journal of*
 1996 *Geophysical Research: Earth Surface*, 123(7), 1566-1589.
- 1997 62. Long, Joseph W; Plant, Nathaniel G; Extended Kalman Filter framework for forecasting
 1998 shoreline evolution. *Geophysical Research Letters* 39 13 (2012)
- 1999 63. Lorensen, W. E., & Cline, H. E. (1987). Marching cubes: A high resolution 3D surface
 2000 construction algorithm. *ACM siggraph computer graphics*, 21(4), 163-169.
 2001

- 2002 64. Ludka, B. C., Guza, R. T., O'Reilly, W. C., Merrifield, M. A., Flick, R. E., Bak, A. S., ...
2003 & Boyd, G. (2019). Sixteen years of bathymetry and waves at San Diego beaches.
2004 *Scientific data*, 6(1), 1-13.
- 2005 65. Lyard, F. H., Allain, D. J., Cancet, M., Carrère, L., & Picot, N. (2021). FES2014 global
2006 ocean tide atlas: design and performance. *Ocean Science*, 17(3), 615-649.
- 2007 66. Moin, P. (2010). *Fundamentals of engineering numerical analysis*. Cambridge University
2008 Press.
- 2009 67. Montaña, Jennifer; Coco, Giovanni; Antolinez, Jose A.A; Beuzen, Tomas; Bryan, Karin
2010 R.; Cagigal, Laura; Castelle, Bruno; Davidson, Mark; Goldstein, Evan B.; Ibaceta,
2011 Raimundo; Idier, Déborah; Ludka, Bonnie; MasoudAnsari, Sina; Mendez, Fernando;
2012 Murray, A. Brad; Plant, Nathaniel G.; Ratliff, Katherine; Robinet, Arthur; Rueda, Ana;
2013 Senechal, Nadia; Simmons, Joshua; Splinter, Kristen; Stephens, Scott; Townend, Ian;
2014 Vitousek, Sean; Vos, Kilian. Blind testing of shoreline evolution models. *Scientific*
2015 *Reports* 10(1), 1-10. (2020)
- 2016 68. Moore, L. J., Ruggiero, P., & List, J. H. (2006). Comparing mean high water and high
2017 water line shorelines: should proxy-datum offsets be incorporated into shoreline change
2018 analysis?. *Journal of Coastal Research*, 22(4 (224)), 894-905.
- 2019 69. Morim, J., Hemer, M., Wang, X. L., Cartwright, N., Trenham, C., Semedo, A., ... &
2020 Andutta, F. (2019). Robustness and uncertainties in global multivariate wind-wave
2021 climate projections. *Nature Climate Change*, 9(9), 711-718.
- 2022 70. Morim, J., Vitousek, S., Hemer, M., Reguero, B., Erikson, L., Casas-Prat, M., ... &
2023 Timmermans, B. (2021). Global-scale changes to extreme ocean wave events due to
2024 anthropogenic warming. *Environmental Research Letters*, 16(7), 074056.
- 2025 71. Murray, A. B., Gasparini, N. M., Goldstein, E. B., & Van der Wegen, M. (2016).
2026 Uncertainty quantification in modeling earth surface processes: more applicable for some
2027 types of models than for others. *Computers & Geosciences*, 90, 6-16.
- 2028 72. Nelson, T. R., & Miselis, J. L. (2019). Method For Observing Breach Geomorphic
2029 Evolution: Satellite Observation of the Fire Island Wilderness Breach. In *Coastal*
2030 *Sediments 2019-Proceedings Of The 9th International Conference* (p. 71). World
2031 Scientific.
- 2032 73. O'Reilly, W. C., Olfe, C. B., Thomas, J., Seymour, R. J., & Guza, R. T. (2016). The
2033 California coastal wave monitoring and prediction system. *Coastal Engineering*, 116,
2034 118-132.
- 2035 74. Otsu, N. (1979). A threshold selection method from gray-level histograms. *IEEE*
2036 *transactions on systems, man, and cybernetics*, 9(1), 62-66.
- 2037 75. Pape, L., Kuriyama, Y., & Ruessink, B. G. (2010). Models and scales for cross-shore
2038 sandbar migration. *Journal of Geophysical Research: Earth Surface*, 115(F3).

- 2039 76. Pardo-Pascual, J. E., Almonacid-Caballer, J., Ruiz, L. A., & Palomar-Vázquez, J. (2012).
 2040 Automatic extraction of shorelines from Landsat TM and ETM+ multi-temporal images
 2041 with subpixel precision. *Remote Sensing of Environment*, 123, 1-11.
- 2042 77. Pelnard-Considere, R. (1956). Essai de theorie de l'évolution des formes de rivage en
 2043 plages de sable et de galets. 4th Journées de l'Hydraulique, Les énergies de la Mer, Paris,
 2044 3(1), 289-298.
- 2045 78. Sweet, W., Horton, R., Kopp, R., & Romanou, A. (2017). Sea level rise.
- 2046 79. Turner, I. L., Harley, M. D., Almar, R., & Bergsma, E. W. (2021). Satellite optical
 2047 imagery in Coastal Engineering. *Coastal Engineering*, 167, 103919.
- 2048 80. Ranasinghe, Roshanka; Callaghan, David; Stive, Marcel JF; Estimating coastal recession
 2049 due to sea level rise: beyond the Bruun rule. *Climatic Change* 110 4-Mar 561-574 (2012)
- 2050 81. Ranasinghe, Roshanka. On the need for a new generation of coastal change models for
 2051 the 21st century. *Scientific Reports* 10, no. 1 (2020).
- 2052 82. Reeve, DE; Fleming, CA; A statistical-dynamical method for predicting long term coastal
 2053 evolution. *Coastal Engineering* 30 4-Mar 259-280 (1997)
- 2054 83. Reeve, Dominic E; Karunarathna, Harshinie; Pan, Shunqi; Horrillo-Caraballo, Jose M;
 2055 Różyński, Grzegorz; Ranasinghe, Roshanka; Data-driven and hybrid coastal
 2056 morphological prediction methods for mesoscale forecasting. *Geomorphology* 256
 2057 49-67 (2016)
- 2058 84. Regard, V., Prémaillon, M., Dewez, T. J. B., Carretier, S., Jeandel, C., Godderis, Y., ... &
 2059 Fabre, S. (2022). Rock coast erosion: an overlooked source of sediments to the ocean.
 2060 Europe as an example. *Earth and Planetary Science Letters*, 579, 117356.
- 2061 85. Robinet, A.; Idier, D.; Castelle, B.; & Marieu, V.; A reduced-complexity shoreline
 2062 change model combining longshore and cross-shore processes: the LX-Shore model.
 2063 *Environmental modelling & software*, 109, 1-16. (2018)
- 2064 86. Roelvink, Dano; A guide to modeling coastal morphology 12 (2011)
- 2065 87. Roelvink, D., Huisman, B., Elghandour, A., Ghonim, M., & Reyns, J. (2020). Efficient
 2066 modeling of complex sandy coastal evolution at monthly to century time scales. *Frontiers*
 2067 *in Marine Science*, 7, 535.
- 2068 88. Rosati, J. D., Dean, R. G., & Walton, T. L. (2013). The modified Bruun Rule extended
 2069 for landward transport. *Marine Geology*, 340, 71-81.
- 2070 89. Ruggiero, P., Kaminsky, G. M., Gelfenbaum, G., & Cohn, N. (2016). Morphodynamics
 2071 of prograding beaches: A synthesis of seasonal-to century-scale observations of the
 2072 Columbia River littoral cell. *Marine Geology*, 376, 51-68.
- 2073 90. Ruggiero, P., & List, J. H. (2009). Improving accuracy and statistical reliability of
 2074 shoreline position and change rate estimates. *Journal of Coastal Research*, 25(5 (255)),
 2075 1069-1081.

- 2076 91. Ruggiero, Peter; List, Jeff; Hanes, Dan; Eshleman, Jodi; Probabilistic shoreline change
2077 modeling. *Coastal Engineering* 2006: (In 5 Volumes) 3417-3429 (2007)
- 2078 92. Saha, S., Moorthi, S., Pan, H. L., Wu, X., Wang, J., Nadiga, S., ... & Goldberg, M.
2079 (2010). The NCEP climate forecast system reanalysis. *Bulletin of the American*
2080 *Meteorological Society*, 91(8), 1015-1058.
- 2081 93. Schwing, F. B. (2000). Record coastal upwelling in the California Current in 1999.
2082 *CalCOFI Rep.*, 41, 148-161.
- 2083 94. Smith, K. E., Terrano, J. F., Pitchford, J. L., & Archer, M. J. (2021). Coastal Wetland
2084 Shoreline Change Monitoring: A Comparison of Shorelines from High-Resolution
2085 WorldView Satellite Imagery, Aerial Imagery, and Field Surveys. *Remote Sensing*,
2086 13(15), 3030.
- 2087 95. Splinter, Kristen D; Turner, Ian L; Davidson, Mark A; Barnard, Patrick; Castelle, Bruno;
2088 Oltman-Shay, Joan; A generalized equilibrium model for predicting daily to interannual
2089 shoreline response. *Journal of Geophysical Research: Earth Surface* 119 9 1936-1958
2090 (2014)
- 2091 96. Sweet, W.V., Hamlington, B.D., Kopp, R.E., Weaver, C.P., Barnard, P.L., Bekaert, D.,
2092 Brooks, W., Craghan, M., Dusek, G., Frederikse, T., Garner, G., Genz, A.S., Krasting,
2093 J.P., Larour, E., Marcy, D., Marra, J.J., Obeysekera, J., Osler, M., Pendleton, M., Roman,
2094 D., Schmied, L., Veatch, W., White, K.D., and Zuzak, C., 2022. Global and regional sea
2095 level rise scenarios for the United States: updated mean projections and extreme water
2096 level probabilities along U.S. coastlines. NOAA Technical Report NOS 01. National
2097 Oceanic and Atmospheric Administration, National Ocean Service, Silver Spring, MD,
2098 111 pp., [https://oceanservice.noaa.gov/hazards/sealevelrise/noaa-nos-techrpt01-global-](https://oceanservice.noaa.gov/hazards/sealevelrise/noaa-nos-techrpt01-global-regional-SLR-scenarios-US.pdf)
2099 [regional-SLR-scenarios-US.pdf](https://oceanservice.noaa.gov/hazards/sealevelrise/noaa-nos-techrpt01-global-regional-SLR-scenarios-US.pdf)
- 2100 97. Taylor, B. N., & Kuyatt, C. E. (1994). Guidelines for evaluating and expressing the
2101 uncertainty of NIST measurement results (Vol. 1297). Gaithersburg, MD: US
2102 Department of Commerce, Technology Administration, National Institute of Standards
2103 and Technology.
- 2104 98. Toimil, A., Losada, I. J., Camus, P., & Díaz-Simal, P. (2017). Managing coastal erosion
2105 under climate change at the regional scale. *Coastal Engineering*, 128, 106-122.
- 2106 99. Toimil, A., Camus, P., Losada, I. J., Le Cozannet, G., Nicholls, R. J., Idier, D., &
2107 Maspataud, A. (2020a). Climate change-driven coastal erosion modelling in temperate
2108 sandy beaches: Methods and uncertainty treatment. *Earth-Science Reviews*, 202, 103110.
- 2109 100. Toimil, A., Losada, I. J., Nicholls, R. J., Dalrymple, R. A., & Stive, M. J. (2020b).
2110 Addressing the challenges of climate change risks and adaptation in coastal areas: A
2111 review. *Coastal Engineering*, 156, 103611.
- 2112 101. Toimil, A., Camus, P., Losada, I. J., & Alvarez-Cuesta, M. (2021). Visualising the
2113 uncertainty cascade in multi-ensemble probabilistic coastal erosion projections. *Frontiers*
2114 *in Marine Science*, 8, 683535.

- 2115 102. Troy, C. D., Cheng, Y. T., Lin, Y. C., & Habib, A. (2021). Rapid lake Michigan
2116 shoreline changes revealed by UAV LiDAR surveys. *Coastal Engineering*, 170, 104008.
- 2117 103. Turner, I. L., Harley, M. D., Short, A. D., Simmons, J. A., Bracs, M. A., Phillips,
2118 M. S., & Splinter, K. D. (2016). A multi-decade dataset of monthly beach profile surveys
2119 and inshore wave forcing at Narrabeen, Australia. *Scientific data*, 3(1), 1-13
- 2120 104. Turner, I. L., Harley, M. D., Almar, R., & Bergsma, E. W. (2021). Satellite
2121 optical imagery in *Coastal Engineering*. *Coastal Engineering*, 167, 103919.
- 2122 105. Vitousek, Sean and Patrick L. Barnard; A nonlinear, implicit one-line model to
2123 predict long-term shoreline change. *The Proceedings of the Coastal Sediments*. (2015).
- 2124 106. Vitousek, Sean; Barnard, Patrick L; Limber, Patrick; Can beaches survive climate
2125 change? *Journal of Geophysical Research: Earth Surface* 122 4 1060-1067 (2017a)
- 2126 107. Vitousek, Sean; Barnard, Patrick L; Limber, Patrick; Erikson, Li; Cole, Blake; A
2127 model integrating longshore and cross-shore processes for predicting long-term shoreline
2128 response to climate change. *Journal of Geophysical Research: Earth Surface* 122 4 782-
2129 806 (2017b)
- 2130 108. Vitousek, S., Buscombe, D., Vos, K., Barnard, P. L., Ritchie, A. C., & Warrick, J.
2131 A. (2023). The future of coastal monitoring through satellite remote sensing. *Cambridge*
2132 *Prisms: Coastal Futures*, 1, e10.
- 2133 109. Vitousek, S., Vos, K., Splinter, K., Erikson, L., Barnard, P., & O'Neill, A. Coastal
2134 Storm Modeling System coastal change projections (CoSMoS-COAST) for California,
2135 (ver. 1): U.S. Geological Survey data release, <https://doi.org/xx.xxxx> , (2023 - under
2136 review) [data set]
2137 (*The data set produced as part of the current under-review paper will be made publicly
2138 available on USGS ScienceBase with a valid DOI upon provisional acceptance of this
2139 manuscript and subject to USGS internal review protocols. For purposes of peer review
2140 only, the provisional data set is currently available here:
2141 [https://drive.google.com/drive/folders/1FH6IkC7OND55qiNTdf2XIWAyMMOkwvuM?](https://drive.google.com/drive/folders/1FH6IkC7OND55qiNTdf2XIWAyMMOkwvuM?usp=share_link)
2142 [usp=share_link](https://drive.google.com/drive/folders/1FH6IkC7OND55qiNTdf2XIWAyMMOkwvuM?usp=share_link))
2143
- 2144 110. Vitousek, S. CoSMoS-COAST: The Coastal, One-line, Assimilated, Simulation
2145 Tool of the Coastal Storm Modeling System, (ver. 1): U.S. Geological Survey software
2146 release, <https://doi.org/xx.xxxx> , (2023 - under review) [software]
2147 (*The modeling software produced as part of the current under-review paper will be
2148 made publicly available on the USGS code.usgs.gov repository with a valid DOI upon
2149 provisional acceptance of this manuscript and subject to USGS internal review protocols.
2150 For purposes of peer review only, the provisional software is currently available here:
2151 [https://drive.google.com/drive/folders/1hYCACddm2mVRNHLTssAx4WdytWm1cO3M](https://drive.google.com/drive/folders/1hYCACddm2mVRNHLTssAx4WdytWm1cO3M?usp=share_link)
2152 [?usp=share_link](https://drive.google.com/drive/folders/1hYCACddm2mVRNHLTssAx4WdytWm1cO3M?usp=share_link))
2153
2154
2155

- 2156
- 2157 111. Vos, K., Splinter, K. D., Harley, M. D., Simmons, J. A., & Turner, I. L. (2019a).
 2158 CoastSat: A Google Earth Engine-enabled Python toolkit to extract shorelines from
 2159 publicly available satellite imagery. *Environmental Modelling & Software*, *122*, 104528.
- 2160 112. Vos, K., Harley, M. D., Splinter, K. D., Simmons, J. A., & Turner, I. L. (2019b).
 2161 Sub-annual to multi-decadal shoreline variability from publicly available satellite
 2162 imagery. *Coastal Engineering*, *150*, 160-174.
- 2163 113. Vos, K., Harley, M. D., Splinter, K. D., Walker, A., & Turner, I. L. (2020). Beach
 2164 slopes from satellite-derived shorelines. *Geophysical Research Letters*, *47*(14),
 2165 e2020GL088365.
 2166
- 2167 114. Vos, K. (2022). Time-series of shoreline change along the Pacific Rim (v1.3).
 2168 Zenodo. <https://doi.org/10.5281/zenodo.4760144> [data set].
- 2169 115. Vos, K., Harley, M. D., Turner, I. L., & Splinter, K. D. (2023). Pacific shoreline
 2170 erosion and accretion patterns controlled by El Niño/Southern Oscillation. *Nature*
 2171 *Geoscience*, *16*(2), 140-146.
- 2172 116. Voudoukas, M. I., Ranasinghe, R., Mentaschi, L., Plomaritis, T. A., Athanasiou,
 2173 P., Lujendijk, A., & Feyen, L. (2020). Sandy coastlines under threat of erosion. *Nature*
 2174 *climate change*, *10*(3), 260-263.
- 2175 117. Warrick, J. A., Vos, K., East, A. E., & Vitousek, S. (2022). Fire (plus) flood
 2176 (equals) beach: coastal response to an exceptional river sediment discharge event.
 2177 *Scientific Reports*, *12*(1), 3848.
- 2178 118. Warrick, J. A., East, A. E., & Dow, H. (2023). Fires, floods and other extreme
 2179 events—How watershed processes under climate change will shape our coastlines.
 2180 *Cambridge Prisms: Coastal Futures*, *1*, e2.
- 2181 119. Willmott, C. J. (1981). On the validation of models. *Physical geography*, *2*(2),
 2182 184-194.
- 2183 120. Wright, L. D., & Short, A. D. (1984). Morphodynamic variability of surf zones
 2184 and beaches: a synthesis. *Marine geology*, *56*(1-4), 93-118.
- 2185 121. Yates, ML; Guza, RT; O'reilly, WC; Equilibrium shoreline response:
 2186 Observations and modeling. *Journal of Geophysical Research: Oceans* 114 C9 (2009)
- 2187 122. Young, A. P., Guza, R. T., Matsumoto, H., Merrifield, M. A., O'Reilly, W. C., &
 2188 Swirad, Z. M. (2021). Three years of weekly observations of coastal cliff erosion by
 2189 waves and rainfall. *Geomorphology*, *375*, 107545.
- 2190 123. Zarifsanayei, A. R., Antolínez, J. A., Etemad-Shahidi, A., Cartwright, N., &
 2191 Strauss, D. (2022). A multi-model ensemble to investigate uncertainty in the estimation
 2192 of wave-driven longshore sediment transport patterns along a non-straight coastline.
 2193 *Coastal Engineering*, *173*, 104080.